



# Fabrication of highly textured AuCu nanoparticles on α-Al<sub>2</sub>O<sub>3</sub> derived by solid-state dewetting

presented by

Evelyn Nachbauer

Institute of Micro- and Nanostructure Research
Prof. Dr. rer. nat. habil. Erdmann Spiecker
Supervisors: Johanna Schubert and Martin Dierner

Erlangen, 09. September 2021

### **Abstract**

In this study the fabrication of AuCu nanoparticles by solid-state dewetting (SSD) of thin films is examined. Using physical vapor deposition Cu and Au bilayer thin films with a total film thickness of 40nm with different concentrations were applied on top of a α-Al<sub>2</sub>O<sub>3</sub> substrate. AFM measurements were performed to verify the accuracy of the deposited layer thicknesses. It is also revealed rim formation at a dewetted sample by mass accumulation at the edges of the formed holes. Furthermore, three predominant directions of SSD were identified by applying FFT to a SEM image resulting from favoured SSD along the (110) directions. Subsequently, the dewetting behaviour of the AuCu thin films were evaluated to optimize parameters for creating nanoparticles. Therefore, thin films were annealed in a rapid thermal annealing furnace where subsequently fast cooling was applied. EDX measurements were taken of particles confirming the successful formation of a AuCu solid solution. Annealing parameters at 850 °C for 120 s were identified as the ideal ones for formation of particles. A trend of increasing SSD with higher annealing temperatures and longer annealing times was observed. Analysis under the SEM reveals the particles' faceting that indicates a (111) out of plane texture which is expected for fcc metals on a α-Al<sub>2</sub>O<sub>3</sub> substrate. XRD measurements were performed to identify the exact lattice parameter aiming for lattice match and the particles' orientation confirming the predominant (111) out of plane texture. A lattice match between film and substrate was accomplished at 52 at.% by varying the thin film's Au concentration. At this concentration texture loss was observed. The hypothesis is that it is apparently energetically more favourable for particles to tilt away than forming a coherent, but strained interface. Additionally, further heating at lower temperatures at 350 °C and 400 °C yielded ordered phases which were analysed in the XRD, identifying an out of plane (111) orientation. In the final steps these ordered phases were also created on SiN<sub>x</sub> membrane TEM grids and analysed by SAD. These imply a (2-32) zone axis with a lattice parameter deviating  $\Delta a = 0.12 \text{Å}$  from the ordered phases on the  $\alpha$ -Al<sub>2</sub>O<sub>3</sub> substrate.

# Content

Abstract	iii
List of abbreviations and symbols	vi
1. Introduction	1
2. Fundamentals	2
2.1 Solid-state dewetting	2
2.1.1 Void formation and void growth	3
2.1.2 The evolution of particle formation	4
2.2 Particle alignment and faceting	6
2.3 Correlation between thin film and substrate	7
3. Materials and methods	10
3.1 The AuCu system	10
3.2 Electron beam physical vapour deposition	12
3.3 Rapid thermal annealing	14
3.4 Atomic force microscopy	16
3.5 Scanning electron microscopy	18
3.6 Energy dispersive X-ray spectroscopy	21
3.7 X-ray diffraction	23
3.8 Transmission electron microscopy	26
3.8.1 Selected area diffraction	27
3.9 Specimen preparation and precalculations	29
3.9.1 Sample preparation for layer deposition	29
3.9.2 Determination of thin film composition	29
4. Results	33
4.1 Thickness measurements with the AFM	33
4.2 Variation of dewetting temperature and time	36

4.2.1 SEM characterization of SSD	36
4.2.2 EDX measurements	43
4.3 Characteristics of AuCu particles	44
4.3.1 SEM characterization of particles	44
4.3.2 EDX measurements	46
4.3.3 SEM characterization of faceting	47
4.3.3 XRD measurements	50
4.3.4 Lattice parameter calculation	52
4.4 Adjustment of the lattice parameter	53
4.4.1 XRD measurements	56
4.5 Ordered phases in particles	59
4.5.1 XRD characterization	59
4.5.2 TEM investigations	62
5. Discussion	65
5.1 The solid-state dewetting process	65
5.1.1 Deviations from the SSD trend	66
5.2 Particle formation	67
5.3 XRD discussion	68
5.3.1 Deviations of peak appearances	69
5.3.2 Peak observation	72
6. Conclusion and Outlook	74
References	76
List of Figures	79
List of Tables	84
Appendix	85
Acknowledgement	90
Prüfungsrechtliche Erklärung	91

## List of abbreviations and symbols

α-Al<sub>2</sub>O<sub>3</sub> Sapphire

Ar Argon

Au Gold

BSD Backscattered Diffraction

BSE Backscattered Electrons

CBS Concentric Backscatter

Cu Copper

EBSD Electron Backscattered Diffraction

EDX Energy Dispersive X-Ray Spectroscopy

fcc face centred cubic

FIB Focused Ion Beam

FWHM Full Width at Half Maximum

H<sub>2</sub> Hydrogen

NP Nanoparticle

OOP out-of-plane

PVD Physical Vapour Deposition

RTA Rapid Thermal Annealing

SAD Selected Area Diffraction

SE Secondary Electrons

SEM Scanning Electron Microscope

SiO<sub>x</sub> Silicon oxide (amorphous)

SSD Solid-State Dewetting

TEM Transmission Electron Microscope

TLD Through-Lens Detector

XRD X-Ray Diffraction

### 1. Introduction

Over the years the industries constantly aimed for more efficient and simultaneously smaller devices. Therefore, thinner films were applied where the first problems of devices failing occurred caused by Solid-State Dewetting (SSD). This is the main reason for microelectronics to collapse, especially emerging with higher temperatures during operation which also limits the applications [1].

Nevertheless, this phenomenon motivates the research in SSD to efficiently produce nanoparticles (NPs) with specific parameters for a great number of catalytic and sensor applications. The advantage of SSD compared to chemical processes is the control of the particles' size, shape and orientation and that no stabilizers nor other chemical supplements are necessary [1]. Notably bimetallic NPs stand out due to their elemental composition and morphology [2]. They find significant applications in numerous devices where especially AuCu particles show interesting properties for catalytic systems for which reason the production of these NPs are examined in this work. An additional complexity comes within bilayers due to the difficulty of controlling the process of SSD being already challenging for monolayers. Since there is a range of parameters that influence the SSD of thin films, these are identified for the AuCu system in this work [1,3].

The ambition for this thesis is the fabrication of NPs with controlled composition, shape and size. Therefore, the SSD behaviour of AuCu thin films needs to be understood and the ideal parameters for forming NPs need to be determined. For this purpose the samples were analysed under the Scanning Electron Microscope (SEM) visualising the dewetting state. The particles' faceting is an important feature for catalytic applications also being analysed under the SEM. Moreover, lattice match between substrate and particle is aimed for forming a coherent. This is achieved through varying the Au concentration aiming for the ideal concentration for lattice matching. The particles' lattice parameter can be determined through XRD measurements additionally identifying their orientation. The particles' orientation is associated with faceting and therefore also interesting to analyse for catalytic

applications. For further prospects ordered phases were obtained and further analysed.

### 2. Fundamentals

### 2.1 Solid-state dewetting

Thin films find themselves in a thermodynamically metastable state due to their high surface-to-volume ratio [1]. Accordingly SSD describes thin films reaching an energetically favourable state by forming particles below the melting temperature [4]. The driving force for SSD is the minimization of the Gibbs free energy [5]. The total energy minimization is composed of grain boundary energies  $E_{gb}$ , energies of all defects  $E_{def}$ , interface energy  $E_{interf}$  between film and substrate and the surface energies  $E_{surf}$  [4].

$$E_{total} = E_{ab} + E_{def} + E_{inerf} + E_{surf} \tag{1}$$

The main driving force emerges from the reduction of the surface and interface energy. However, a specific activation barrier prevents the thin film from SSD under normal environmental conditions. To activate the SSD the barrier needs to be overcome which is achieved by heating at higher temperatures [1].

After initiating, SSD proceeds in several stages. Firstly, voids nucleate and holes begin forming and consequently start growing after reaching a critical size [5]. Next up, elongated strands are formed which continue to dewet into arrays of particles [6].

Parameters like film thickness, element concentration, defects and grain size effect the development of the SSD [1]. With increasing film thickness the probability of dewetting decreases as well as the dewetting rate. Therefore, higher temperatures are required to initiate SSD of thicker films. Temperature has a great influence on the dewetting rate because the process generally depends on mass transport

through atomic diffusion which is enhanced at higher temperatures [6]. In the following more details on the several processes and impacts on the SSD are provided.

### 2.1.1 Void formation and void growth

The first step of the SSD of thin films is the void formation. Rather high energy must be provided for which reason void nucleation is favoured at defects. Therefore, polycrystalline films have many initiation areas particularly grain boundaries [1]. In general high energy grain boundaries as well as triple junctions provide the most favourable location for this [6]. The initiation takes place by the grain boundaries either starting to groove, at the surface as pointed out in Figure 1a) or a void nucleates at the interface between the substrate and the film, occurring when the interfacial energy is sufficiently high as in 1b) [4].

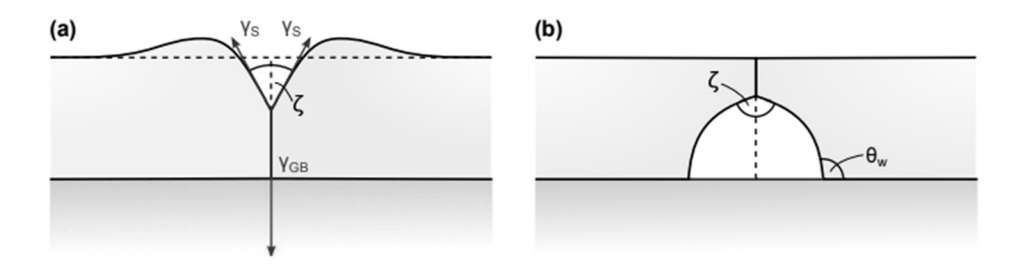


**Figure 1:** Void formation at grain boundaries starting at *a*) the surface by grain boundary grooving or *b*) the interface between the substrate and film [4].

By passing a critical size  $r_{void} > r_{crit}$  the activation barrier is reached so the voids start growing. Otherwise, when  $r_{void} < r_{crit}$ , thin films rebuild again. Additionally diffusion of vacancies as well as of atoms is kinetically preferred at grain boundaries which leads to an increased void growth along those [1]. After a specific incubation time  $\tau$  the total of holes are formed. The thinner the film, the more holes will be formed simultaneously. The dewetting rate is driven by the number of existing holes and their growth rate or the hole formation rate of new ones. [6] The mechanisms

believed to be behind all processes described, are surface self-diffusion, grain boundary and interface diffusion as well as grain boundary sliding. Primarily interface and grain boundary diffusion cause the mass transport off the void [1].

### 2.1.2 The evolution of particle formation

After the voids are build another process, the retraction of the film, driven by capillary forces takes place. To prevent sharp corners and therefore minimize its curvature, material is transported by surface self-diffusion towards the flat film as demonstrated in Figure 2. A rim is built through mass accumulation at the edge whereupon a valley is followed shortly ahead caused by flux divergences. The further the edge retracts and the hole is growing the higher the rim develops. On account of this, the curvature at the edge decreases what leads to a descent of mass transportation and the retraction of the edge [1].

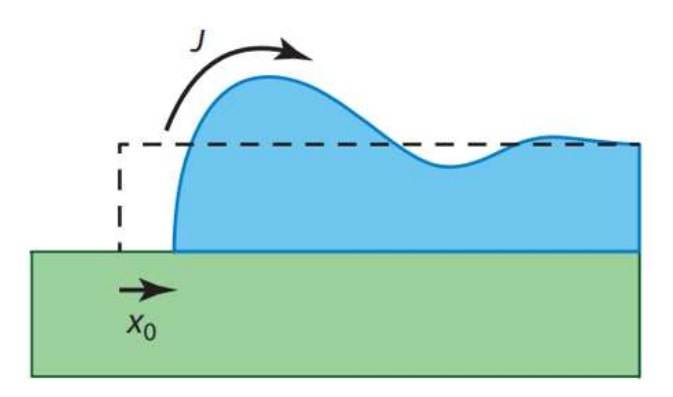


**Figure 2:** Mass accumulation forming a rim due to edge retraction closely followed by valley formation ahead of the rim [6].

Another consequence with the retraction of the edge is the closely followed valley after the rim. Figure 3a) demonstrates the retraction of the valley to deepen, sometimes even until it might reach the substrate and form an isolated rim, being the case in b). This process is called pinch-off, further retracting the new edges to form a new rim and the process being able to restart until particles are formed [6].

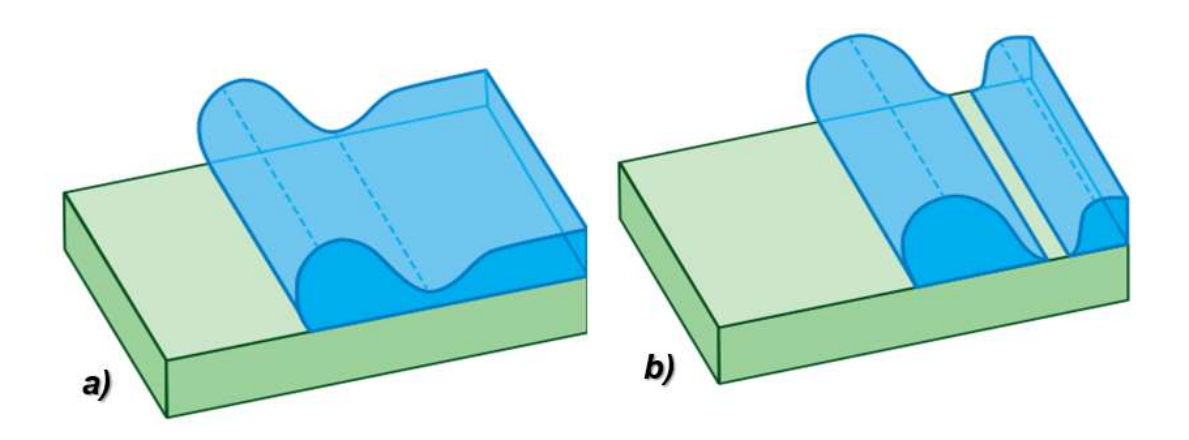


**Figure 3:** *a)* Increasing edge retraction leading to increasing depth of the valley, *b)* sometimes insofar that the valley reaches the substrate and an isolated rim evolves [6].

Another way of formation of isolated rims besides pinch-off is through fingering [6]. By thermal activation some morphologies are built through surface diffusion. The fingering process is illustrated in Figure 4 whereby these further evolve in isolated islands due to the Rayleigh instabilities [1]. The grain structure influences the fingering, favouring high-angled boundaries due to the locally increased self-diffusivity [6].



**Figure 4:** Top view of the fingering process evolving into islands due to Rayleigh instabilities [1].

In later stages of the SSD process the surface diffusivity is not the main kinetic force anymore rather grain boundary migration [4]. With further dewetting elongated strands evolve into separated islands and further into particles due to Rayleigh instability. The specific characteristics of those is discussed in the next point.

### 2.2 Particle alignment and faceting

The formation of facets results on account of surface energy anisotropy of thin films that also causes changes in the mechanism of the SSD [7]. A Wulff shaped particle is the most thermodynamically preferable state which represents the equilibrium. Since every direction in space has a specific surface energy the minimum energy space is favoured [1]. The surface energy can be visualised through the Wulff plot as shown two-dimensionally in Figure 5. In this plot the length of the vector  $\gamma_f$  illustrates the surface energy and the angle  $\omega$  the crystal's orientation. In the case of Figure 5 the surface energy is minimized at the four cusps which relate to the facets at the equilibrium shape of the crystal [6].

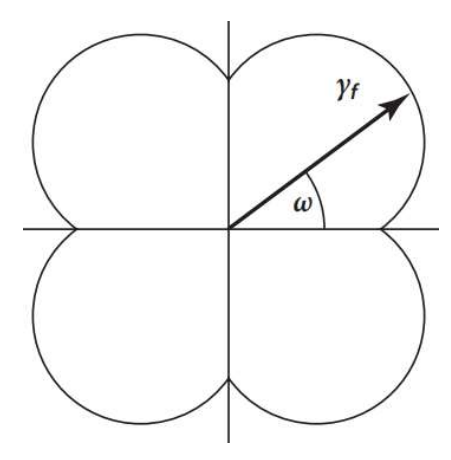


**Figure 5:** A Wulff plot representing the surface energy determined by the length of the vector  $\mathbf{y}_f$  and the crystal's orientation by the angle  $\boldsymbol{\omega}$  resulting in a minimized surface energy at the four cusps [6].

In some instances, metastable shapes are noticed. This may occur when the equilibrium may not be accomplished instantly due to problems forming surface steps on atomically flat, singular faces [1].

The aspect that the substrate influences the SSD and hence also the equilibrium shape of the crystal is considered in the Winterbottom construction shown in Figure 6 [6].

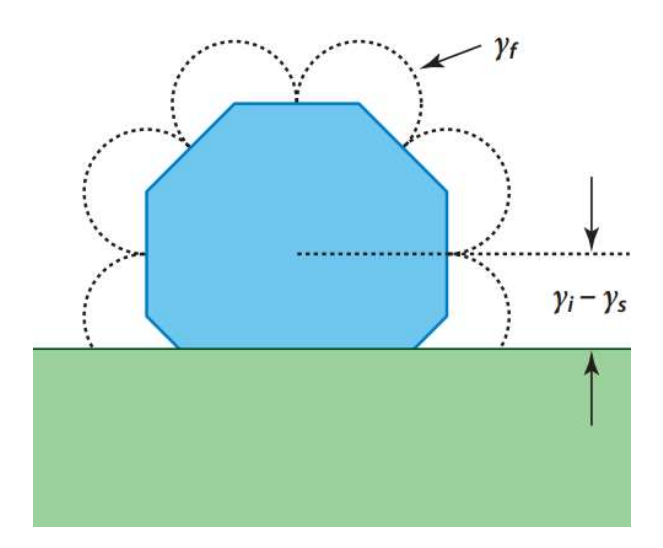


**Figure 6:** The Winterbottom construction considers contrary to the Wulff plot the interface energy between the film and the substrate finding the crystal's equilibrium shape [6].

The Winterbottom construction contemplates the Wulff plot as well as the interface energy between particle and substrate. An advantage of the Winterbottom plot is that the equilibrium state can be approximated for three-dimensional crystals with anisotropic surface energies [6]. Broader insights about the substrate's influence on the SSD process and alignment of particles is given furthermore.

### 2.3 Correlation between thin film and substrate

The substrate's material type, crystallinity and topography have a great impact on the SSD [1]. The structure and chemistry between the metal thin film and the oxide substrate control the behaviour and properties of the particles [8]. The arrangement of the thin film on the substrate's surface depends on the low energy interfaces, symmetry matching and low misfit [9]. A match between the metal's and substrate's lattice is fundamental for the interfacial physical characteristics and therefore in this work the lattice match between particles and substrate is aimed for. When mismatching occurs, homogenous strains are found in the lattice system. At perfect match, a coherent interface forms due to the absence of lattice stress, as visualised in Figure 7a). With increasing mismatch the elastic strain energy enlarges so that

misfit dislocations are formed due to their energetically preference to compensate for high elastic stress fields in semi-coherent interfaces shown in *b*). The incoherent interface demonstrated in c) arises from overlapping strain fields of dislocations with decreasing dislocation spacing [10].

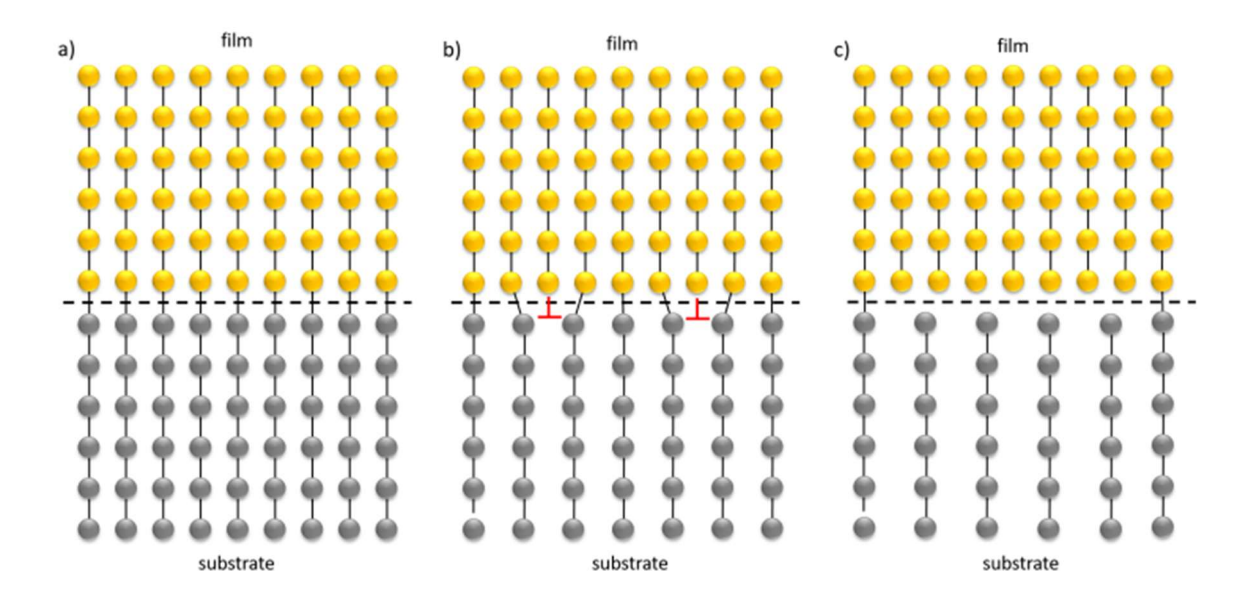


**Figure 7:** Different interface pattern between film and substrate forming a *a*) coherent interface, *b*) semi-coherent interface with misfit dislocations and an *c*) incoherent interface [11].

In a bilayer thin film system, it is possible for the film to adopt to the lattice of the substrate by concentration variation of the film. If the lattice of the film does not deviate much from the substrate's lattice a coherent interface is accomplished with improved mechanical stability which also helps to obtain grain growth of a single orientation [5,6]. When changing the lattice parameter minimally the material's properties are influenced considerably. This is fundamental for the applications because the functional properties change in semiconductors, multiferroics, ferroelectrics, ferromagnets and materials for data storage [12].

Depending on the crystal systems different texturing of the NPs on a  $\alpha$ -Al<sub>2</sub>O<sub>3</sub> substrate is energetically preferred. Considering the fcc structure in the whole solid solution range the energetically favourable out-of-plane (OOP) texture is towards

the *(111)* planes. The reason for this preference is the surface energy minimization in this orientation as well as the rather similarity of the lattice between *(0001)* substrate and *(111)* particle. The equilibrium texture of a *(111)* particle on a *(0001)* oriented  $\alpha$ -Al<sub>2</sub>O<sub>3</sub> substrate is shown in Figure 8a) and b). To describe the complete texture between two crystalline materials, the in-plane relation must also be considered. Regarding the metal<sub>fcc</sub> -  $\alpha$ -Al<sub>2</sub>O<sub>3</sub> system, the most predominant in-plane orientation relation is the one where the *(220)* planes of the metal are parallel to the *(30-30)* planes of the substrate (see Figure 8b)). This relation also determines the mismatch of this system, which can be calculated as follow [5].

$$\delta = \frac{d_{30\overline{3}0} - d_{220}}{d_{30\overline{3}0}} \tag{2}$$

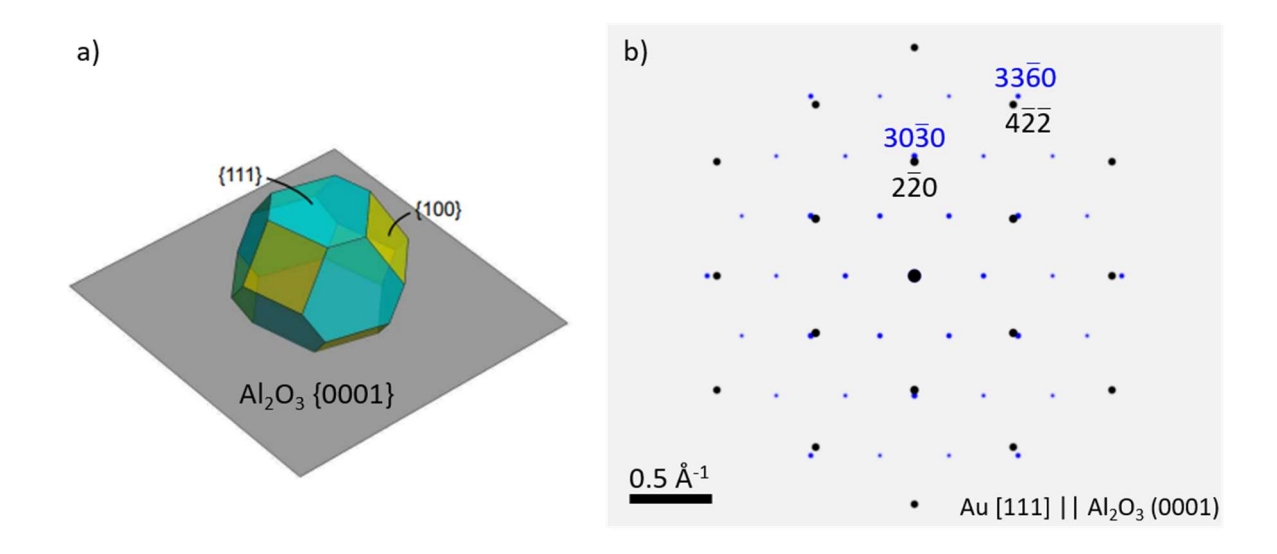


**Figure 8:** a) The equilibrium texturing of a fcc structure forming a (111) oriented particle on a (0001) oriented  $\alpha$ -Al<sub>2</sub>O<sub>3</sub> substrate demonstrating the position and shape of each plane [4]. b) Simulated SAED-Pattern showing the orientation relation Au(111)<1-10> || Al<sub>2</sub>O<sub>3</sub> (0001)<10-10> well known for metal<sub>fcc</sub> – Al<sub>2</sub>O<sub>3</sub> systems [5].

### 3. Materials and methods

The solid-state dewetting of AuCu thin films forming particles is examined in this work. In the following all materials and methods are presented that were used for achieving the results displayed in Chapter 4.

### 3.1 The AuCu system

AuCu alloyed nanoparticles have gained attention due to their ability of catalytic oxidation [13]. The binary AuCu system is characterized by its fcc structure at the whole solid solution range [12]. A 50/50 alloy will be in solid solution at temperatures above 410 °C as shown in the phase diagram in Figure 9. At lower temperatures, for example at an 50/50 alloy below 410 °C, ordered structures will form, but the atomic diffusion may be limited at these low temperatures so that the transformation might proceed very slowly [14]. Depending on the AuCu alloy concentration the ordered phases obtain either a L10-type (CuAu) or a L12-type of structure (AuCu<sub>3</sub> or CuAu<sub>3</sub>). Additionally, a tetragonal crystal system is existent at the L10-type of structure occurring due to the ordering of Au and Cu into layers in the unit cell [15].

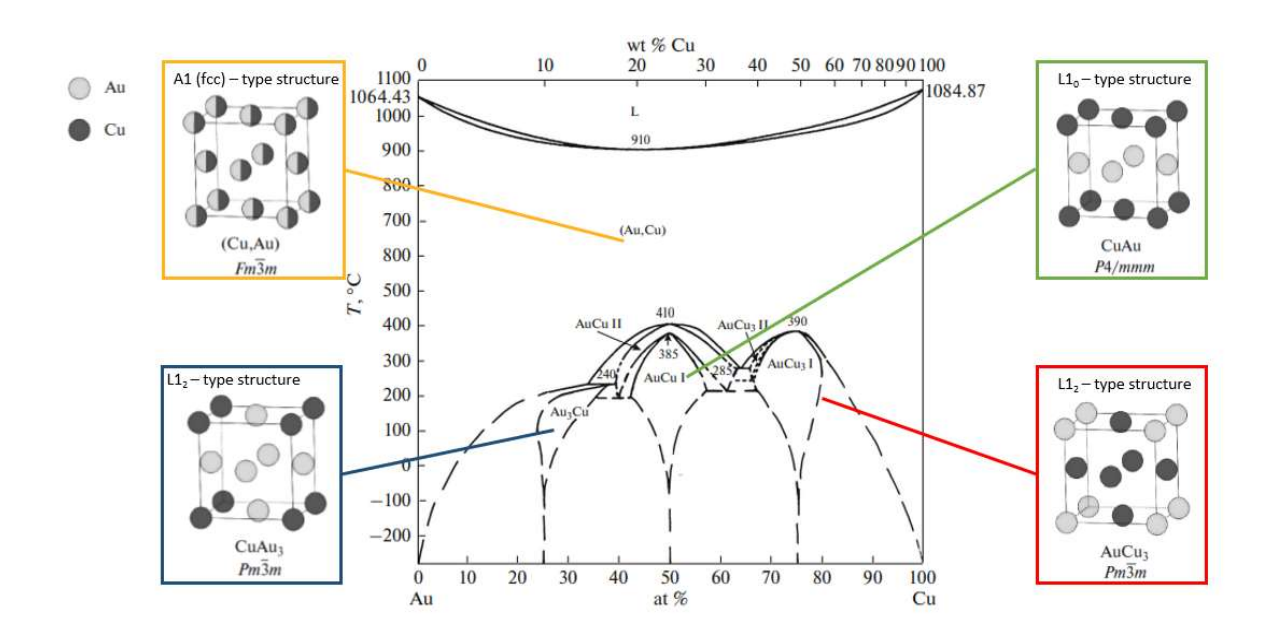


**Figure 9:** Phase diagram of an AuCu alloy with displayed crystallographic structures in each region, showing a fcc structure in the whole solid solution range at higher temperatures. At lower temperatures three types of ordered phases CuAu (green), AuCu<sub>3</sub> (red) and CuAu<sub>3</sub> (blue) exist [15].

### 3.2 Electron beam physical vapour deposition

A typical method for producing thin films is the Physical Vapor Deposition (PVD) due to accomplishing high purity films. There atoms of a solid target material are ejected for example by electron beam heating [16]. This electron beam consists out of electrons emitted out of a cathode at approximately 5-10 kV. The advantage of using an electron beam is the high evaporation rate and that almost all materials can be evaporated. The procedure of PVD is shown in Figure 10 where the particles from the target material are converted into a gaseous state by thermal evaporation. This occurs when the kinetic energy of the atoms or molecules is increased by an electron beam and converted into thermal energy that causes evaporation of the material in the vacuum below about 10-1 mbar. Thereby, these particles conquer the separation energy, evaporate and consequently condense on the substrate placed above. The higher the energy the more atoms are able to be released whereby the required energy is depending on the material's evaporation temperature [17].

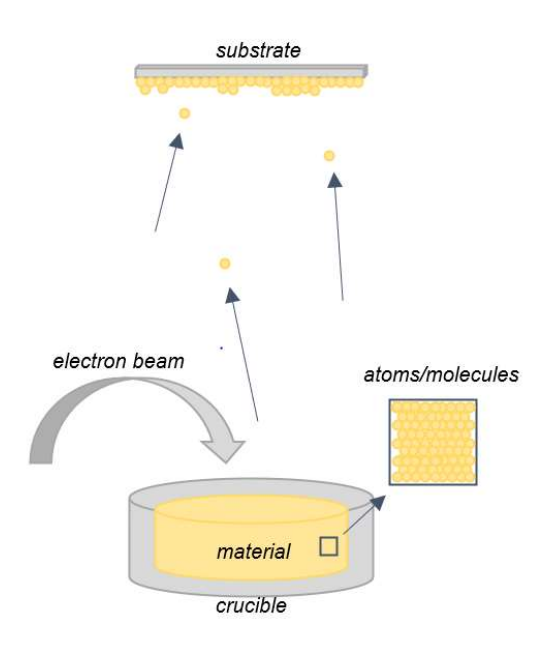


**Figure 10:** Procedure of PVD by E-Beam heating causing material evaporation by inducing high energy. These atoms/molecules are deposited on the substrate placed above.

For the experiments in this work an AuCu layer is deposited by the Winter Vakuumstechnik HVB 130 illustrated in Figure 11.

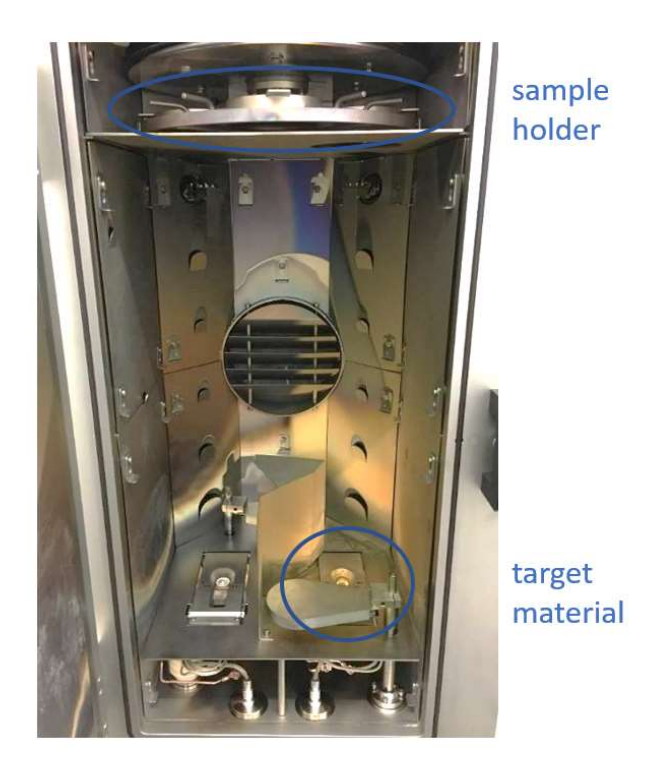


**Figure 11:** Vacuum chamber of a Winter Vakuumstechnik HVB 130 showing the target material and the sample holder positioned above.

By means of this system a multilayer may be accomplished with up to four elements without venting the chamber. Furthermore, specific recipes can be inserted for automatization. The system has two electron guns but only one of them was used due to the corresponding set of material (AuCu) that was required. Au and Cu were evaporated under an acceleration voltage of 8~kV where above four plates are placed with the samples taped onto as demonstrated in Figure 11. These rotating plates enable to operate more than one recipe in one run whereby the deposited layer is measured in situ by oscillating quartz crystals. All samples used in this work were fabricated with the Winter HVB 130 with a coating rate of 0.4~Å/s for Cu and 0.5~Å/s for Au.

### 3.3 Rapid thermal annealing

For achieving SSD of thin films heating is performed to overcome the activation barrier, whereby the RTA furnace has the ideal conditions with its ability of defined heating and cooling rates. For the following experiments the AS-One 100 from ANNEALSYS is used with the advantage of specifically defined annealing times. Especially the feature of high cooling rates enables the fabrication of alloyed or supersaturated AuCu particles in a metastable state. The general construction of an RTA is illustrated in Figure 12.

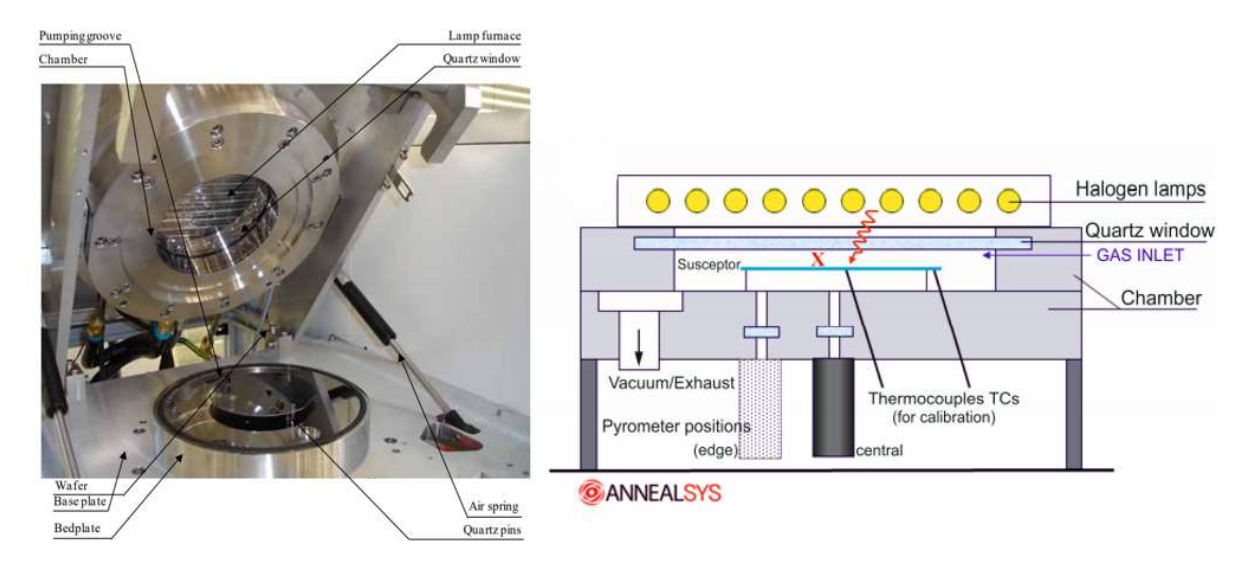


**Figure 12:** The process chamber of an AS-One 100 [18] specified in a cross section of the inside [1] showing the lamp furnace, the cooled bedplate and the quartz pins holding the wafer.

Before starting the heating process three rounds of Ar-flushes were performed while alternately evacuating to vacuum pressure. Afterwards the chamber operates under atmospheric pressure. Heating is accomplished rapidly with a defined heating rate, in this work with 100 °C/s through thermal radiation by halogen lamps. It is performed through the quartz window by accommodating a high temperature range from 400 °C to 1300 °C. [18].

Furthermore, it is possible to control the atmosphere while heating by inducing process gases for example to target specific reactions. Inert gases like Argon (Ar) and Nitrogen or reactive gases such as Oxygen and Hydrogen (H<sub>2</sub>) are available. During heating a gas-flow of 2000 sccm Ar and 100 sccm H<sub>2</sub> (a ratio of 20:1) is set [1]. The sample is positioned in the middle of the wafer using in this experiment a Si<sub>3</sub>N<sub>4</sub> wafer which is placed on top of three quartz pins. Pyrometers measure and control the temperature of the wafer contactless from below preventing measuring the halogen lamps' temperature. Another useful feature is the fast cooling where the pins that hold the wafer are drawn in so that the wafer is in direct contact with the water-cooled bedplate achieving a cooling rate of 200 °C/s [18].

In this experiment different time and temperature test series are run through to find the best annealing temperature and time for creating AuCu particles. Temperatures from 350 °C to 850 °C were applied to obtain the AuCu system in the solid solution as well as in the miscibility gap in the phase diagram. Under these temperatures annealing times from two to twenty minutes in the solid solution and two hours in the miscibility gap were performed.

### 3.4 Atomic force microscopy

The Atomic Force Microscope (AFM) differs from light and electron microscopes especially in the image formation where instead of two-, three-dimensional pictures are obtained. Despite there are various imaging methods, in this work the AFM is only used to map the quantitative topography of surfaces [19]. To create an image the general mechanism is shown in Figure 13 where a sharp tip scans over the sample's surface to observe surface forces [20]. This tip is a construction called cantilever supporting a small beam on one end and the free end holding a tiny tip which is in contact with the sample. [21]. In this work the repulsive forces are measured due to their higher stability in this mode [20]. This means that the tip is in constant physical contact with the sample scanning over it for which a piezoelectric transducer is used to provide this mechanical scanning [20,21]. Forces are measured by the deflection of the cantilever behaving proportional to the detected forces [22].

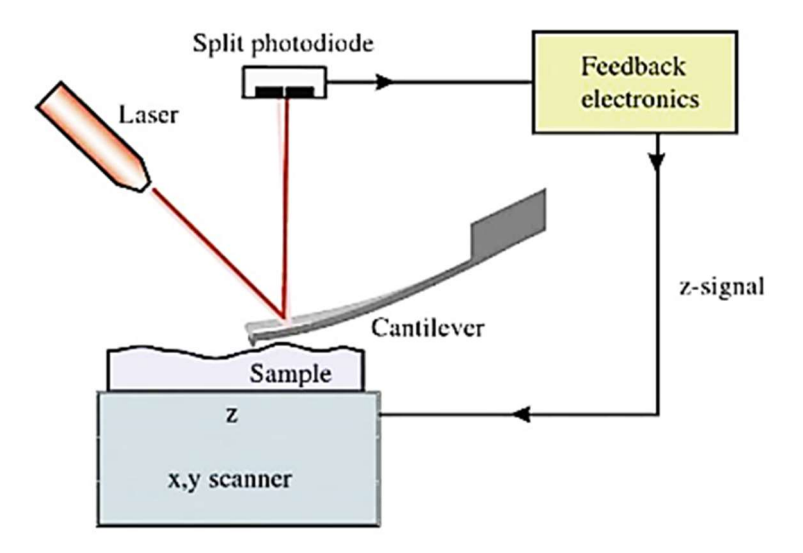


**Figure 13:** A schematic setup of an AFM illustrating the measurement by means of the cantilever in the contact mode. Measurements of the cantilever's deflection are detected which behave proportional to the forces achieving a three-dimensional plot of the height data against the distance [22].

In the next step the computer plots the height data against the distance and consequentially produces a three-dimensional picture [20]. The height, length, width or volume of any feature can be measured easily by means of the generated map [19].

Hence, this tool is used in this work for measuring the film thicknesses applied by the E-Beam, explained in Chapter 3.2. A scratch was carved into the sample's surface as shown in Figure 14 to create a clear edge between sample and substrate. At this edge the AFM is now able to measure the film-substrate height difference.

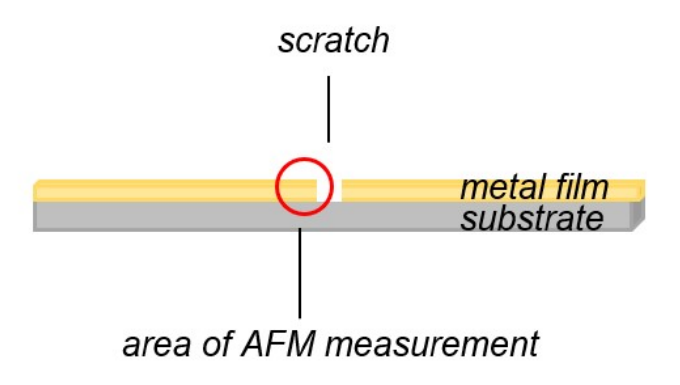


**Figure 14**: Sample preparation for height-difference and film thickness measurement in the AFM.

### 3.5 Scanning electron microscopy

SEM is a common method for the characterization and analysis of the microstructure and morphology of the samples. The image formation results from the interaction between the electron beam and the sample. Two different interactions can be detected which occur through inelastic and elastic interaction. Elastically scattered electrons that are deflected at an angle more than 90° are called Back Scattered Electrons (BSE) whereas the Secondary Electrons (SE) are inelastic scattered electrons. Both kinds of electrons are used for imaging the specimen visualizing different details with either of them. Figure 15 shows the interaction volume and depth of the electron beam with the specimen. It increases with increasing beam energy which means that the depth of emerging BSE is higher as well. The different signals are illustrated depending on the depth of the sample where these are obtained [23].

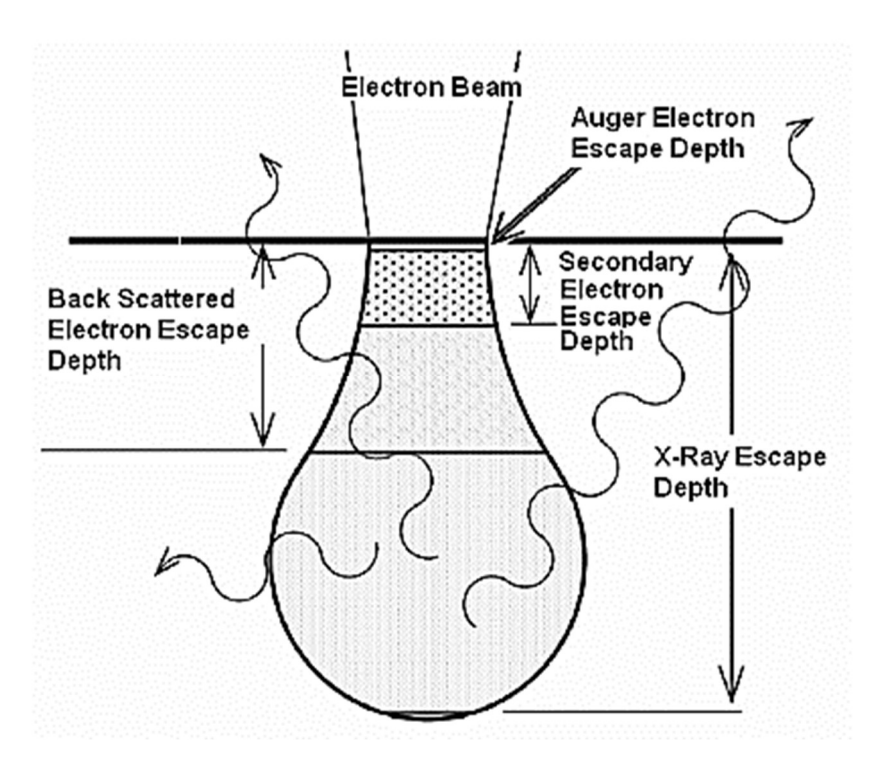


**Figure 15:** Signals generated through beam-specimen interaction illustrated in an interaction volume showing the two electron types for imaging in the SEM, SE and BSE [24].

SE have a low energy of smaller than 50 eV so that those are only able to emit from the sample's surface of about a few nanometres. That is the reason for the good topographic illustration via SE for visualizing surface topography. By using the Everhart-Thornley-Detector with a positive grid current SE are attracted and imaging with those is accomplished. Depending on the amount of SE reaching the detector a rather high amount leads to a good topographical image and the more electrons can emit out of a location, the brighter it appears in the image. To gain both compositional and topographic information BSE are used. These can emerge from much deeper under the specimen's surface with an energy equivalent to the acceleration voltage. Materials with higher atomic numbers cause more BSE signal due to the higher positive charge on their nucleus what induces a higher scattering probability of the primary electrons. This is also useful to identify phase separation in the particles due to their different atomic numbers [23]. Besides the emerging electrons for imaging purposes like BSE and SE, other kinds of signals are produced when an electron beam interacts with the specimen. As seen in Figure 15 X-rays and Auger electrons are observed that can be applied for imaging using specific detectors.

For imaging the samples in this work a Tabletop SEM Phenom ProX by Thermo Fisher Scientific is used. It combines an easy handling with good resolution pictures. The microscope works with a CeB<sub>6</sub> source which provide high brightness and long endurance. Pictures were taken with 10 kV whereby the resolution of this microscope is  $\leq 6nm$  with a SE detector and  $\leq 8nm$  with a BSE detector [25].

The Helios Nanolab 660 from FEI, illustrated in Figure 16, was used for imaging with the SEM as well. The advantage of using this compared to the Tabletop SEM is its higher resolution and the greater variety of detectors and further options. It is helpful for the imaging of particle faceting in this work's experiments. The Concentric Backscatter (CBS) detector and the Through-Lens Detector (TLD) was used for imaging with the two different kinds of electrons.

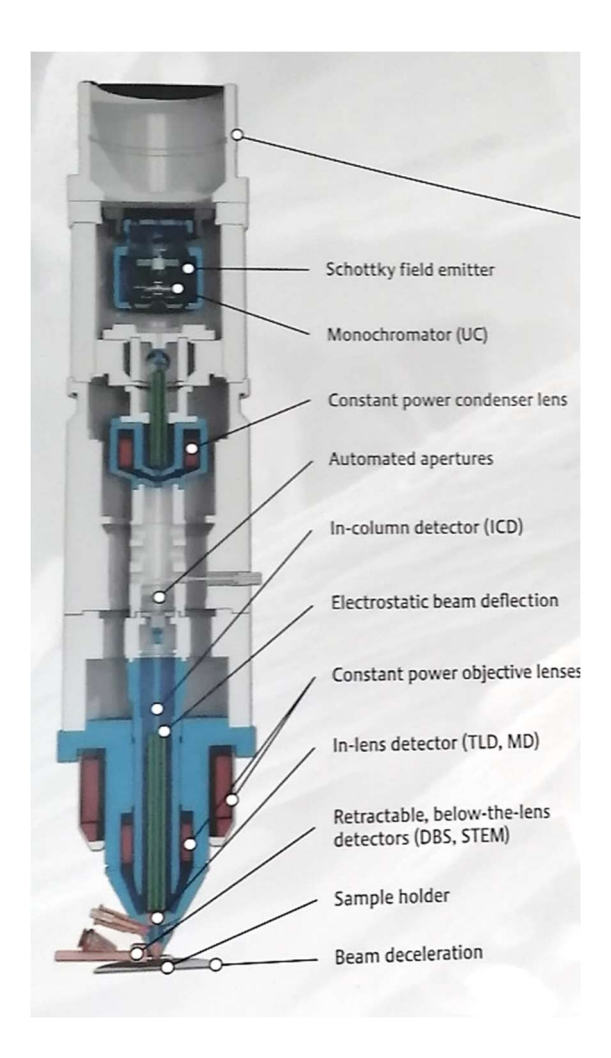


**Figure 16:** Structure of a SEM column of the Helios Nanolab 660 visualising the electron source, the Schottky field emitter, lenses and different detectors [26].

The samples that were analysed by means of the SEM are coated with an approximately 3nm thick layer of carbon before analysing. The step is performed because the sapphire substrate is not conductive and therefore charging effects might occur which are avoided by that. Additionally, both microscopes have the ability of Energy Dispersive X-ray spectroscopy (EDX) which is discussed in Chapter 3.6.

### 3.6 Energy dispersive X-ray spectroscopy

When the electron beam interacts with the specimen, asides SE and BSE also X-rays are generated as seen in Figure 15. These X-rays provide chemical information about the specimen being used as a common microanalytical technique [23]. Energy Dispersive X-ray spectroscopy (EDX) in combination with SEM supply a method of analytical electron microscopy allowing quantitative and qualitative chemical analysis of specimen. Due to the resolution of a few nanometres the thin films and nano- and microparticles can be analysed [27]. These X-rays are created when an initial beam electron collides with an inner shell electron from the specimen illustrated in Figure 17. When the beam electron provides sufficient energy the atom's inner shell electron is knocked out [23]. Due to the lack of this displaced electron the atom becomes ionized aspiring the normal state again. The initial state is achieved by replacing the blank space with an outer atom's electron while the energy difference between these two shells will either produce a characteristic X-ray or an characteristic Auger electron [28].

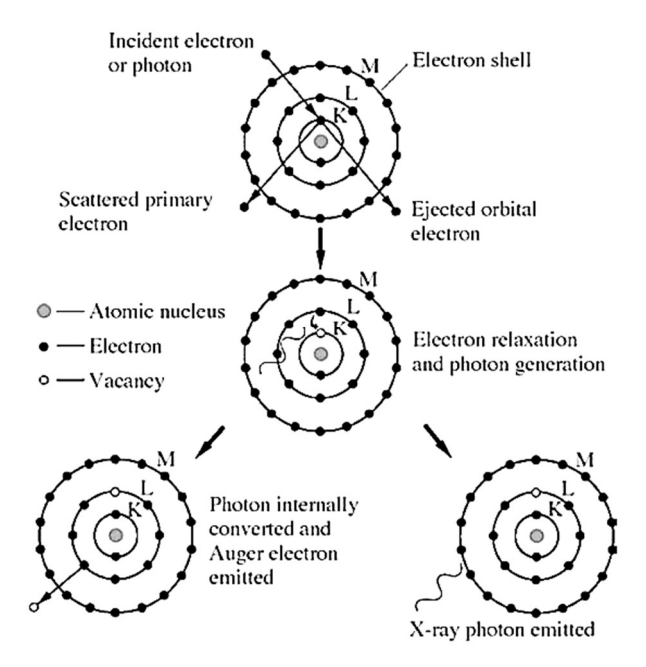


**Figure 17:** Generating characteristic X-rays or Auger electrons through the interaction of the specimen's atoms with the electron beam [28].

For EDX a semiconductor detector is installed like a lithium-drifted Si crystal or a Ge crystal of high purity. The EDX spectra is illustrating the X-ray intensity plotted against the energy. These plots show characteristic peaks of the present elements that are approximately Gaussian shaped [27]. A continuous background is also formed through the deceleration of high-energy electrons [23]. The depth of X-ray production  $R_x$  [nm] is displayed in Equation 3 calculated with the density of the sample  $\rho$ , the energy of the primary electron beam  $E_0$  and ionization energy of the material  $E_c$  [29]:

$$R_x = \frac{64}{\rho} \cdot (E_0^{1.68} - E_c^{1.68}) \tag{3}$$

With the help of the SEM, an EDX map was recorded of the present AuCu film and particles. This proceeds at 15 kV at the Tabletop SEM to capture the gold peak in the diagram. To confirm the successful alloy-formation, qualitative EDX-mappings are performed. Additionally, EDX-point measurements are carried out to quantify the Au and Cu concentration.

### 3.7 X-ray diffraction

The XRD is an important device and a powerful non-destructive technique to characterize crystalline materials regarding their crystalline phases and structural properties [27]. For all measurements done within this thesis a Rigaku Smartlab with a Cu- $K_{\alpha}$  cathode is used. For better resolution a parabolic multilayer mirror is used to monochromize the Cu X-rays.

The analytical method of XRD works with X-rays which in practice are generated as discussed in Chapter 3.6 and visualised in Figure 17. The difference to EDX is that high-speed electrons are targeted at an outstanding metal and not the specimen. As mentioned before, in our case the target material is Cu that creates a wavelength of  $\lambda_{K\alpha} = 1.54$ nm These monochromized X-rays are now targeted at the specimen being analysed. When interacting with the specimen the X-rays are diffracted at the crystallographic planes as visualised in Figure 18 [28].

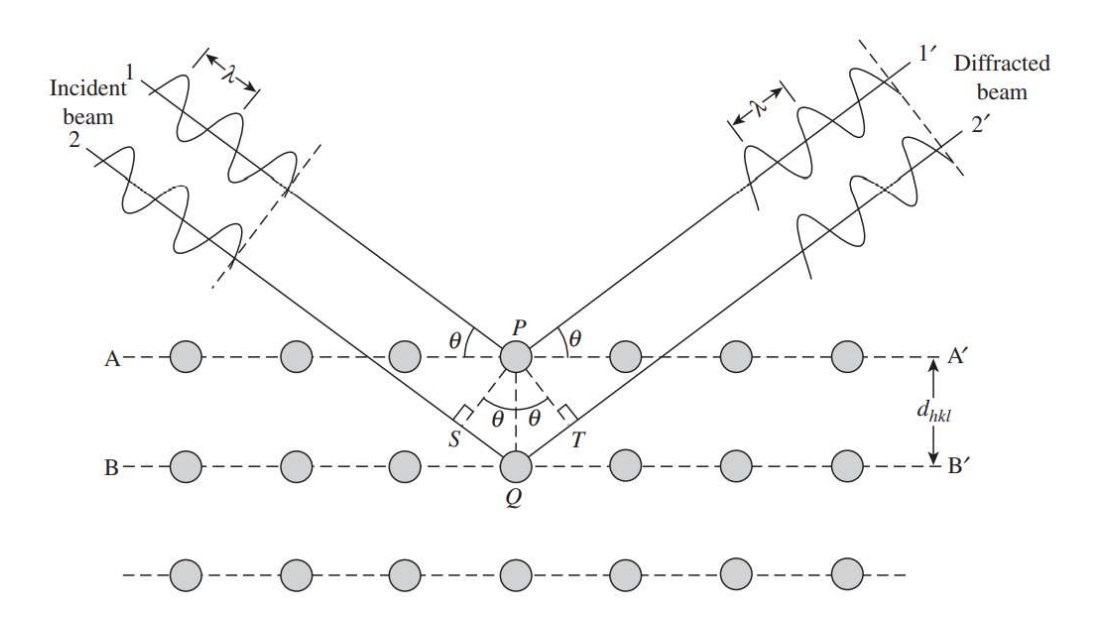


**Figure 18:** Bragg deflection of X-rays at lattice planes at a certain angle  $\theta$  leading to either constructive or to destructive interference depending on the path difference between two waves. [28].

Two waves interact with each other when having the same wavelength and passing the same direction. Thereby, destructive interference occurs when the path difference is  $\frac{n\lambda}{2}$  where both waves cancel each other out. Constructive interference occurs when both waves find themselves in phase so they are amplified. The deflection with constructive interference which is finally detected is described through the Bragg's law [28]:

$$n \cdot \lambda = 2 \cdot d \cdot \sin(\theta) \tag{4}$$

Containing the diffraction order n, the wavelength of the incident beam  $\lambda$ , the lattice spacing d and the angle between wavevector and plane  $\theta$ . The spacing between atomic planes are received through the XRD from the crystalline structure. When a cubic crystal is existent, as in this work the AuCu system, the lattice parameter can be calculated using the XRD data as follows [28]:

$$d_{hkl} = \frac{\lambda}{2 \cdot \sin(\theta_{hkl})} = \frac{a}{\sqrt{h^2 + k^2 + l^2}} \Leftrightarrow a = \frac{\lambda \cdot \sqrt{h^2 + k^2 + l^2}}{2 \cdot \sin(\theta_{hkl})}$$
 (5)

The XRD proceeds through generating a single wavelength X-ray beam and continuously varying the incident angle of this beam. The diffracted X-rays are detected and thereupon the diffraction intensities are plotted against the diffraction angle  $2\theta$ . These different peaks are further analysed comparing with the database holding over 60,000 diffraction spectra of familiar crystalline substances by the ICDD (=International Centre for Diffraction Data) [28].

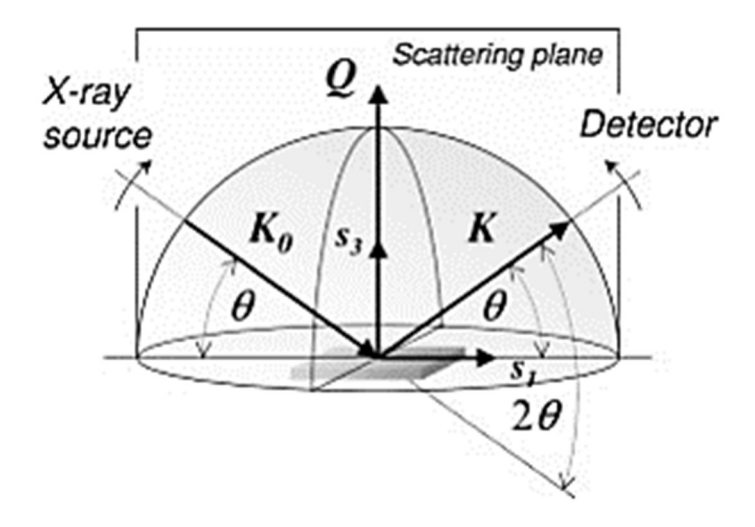


**Figure 19:** Working mechanism of a X-ray OOP measurement illustrating the movement of the X-ray source and detector in equal measure maintaining the same incoming and outcoming angle  $\theta$ . The measured  $2\theta$  angle is visualised as well as the plane being measured [30].

The working mechanism of a XRD OOP measurement, used for the experiments in this work, is visualised in Figure 19. The X-ray beam is directed at the sample at a specific angle  $\theta$  monitoring the scattered radiation under the same angle  $\theta$  at the detector. The angle of incoming and outcoming beam remains the same during the measurement even though those are continuously varied over a defined angular range. This is accomplished by moving the X-ray source and detector similarly as visualised through the arrows in Figure 19. The measured lattice planes are located perpendicular to the scattering vector  $\mathbf{Q}$ . The detected diffraction angle  $2\theta$  is shown through combining the angles between incident beam and scattered beam [30].

The XRD presents a major help in this work for analysing the NPs, their crystallographic OOP-orientation as well as characterizing their lattice parameter.

### 3.8 Transmission electron microscopy

The Transmission Electron Microscope (TEM) is a common tool for microstructural characterization [31]. It irradiates a thin specimen with an electron beam of an energy up to 300 keV. To transmit the electrons through the specimen a particular sample thickness needs to be maintained typically of the order of 100nm [32]. For the TEM experiments in this work a double-corrected Titan Themis 300 is used. In the TEM different types of techniques can be performed like Selected Area Diffraction (SAD) explained in the following. In Figure 20 both a) diffraction and b) imaging mode is illustrated in a simplified TEM column model.

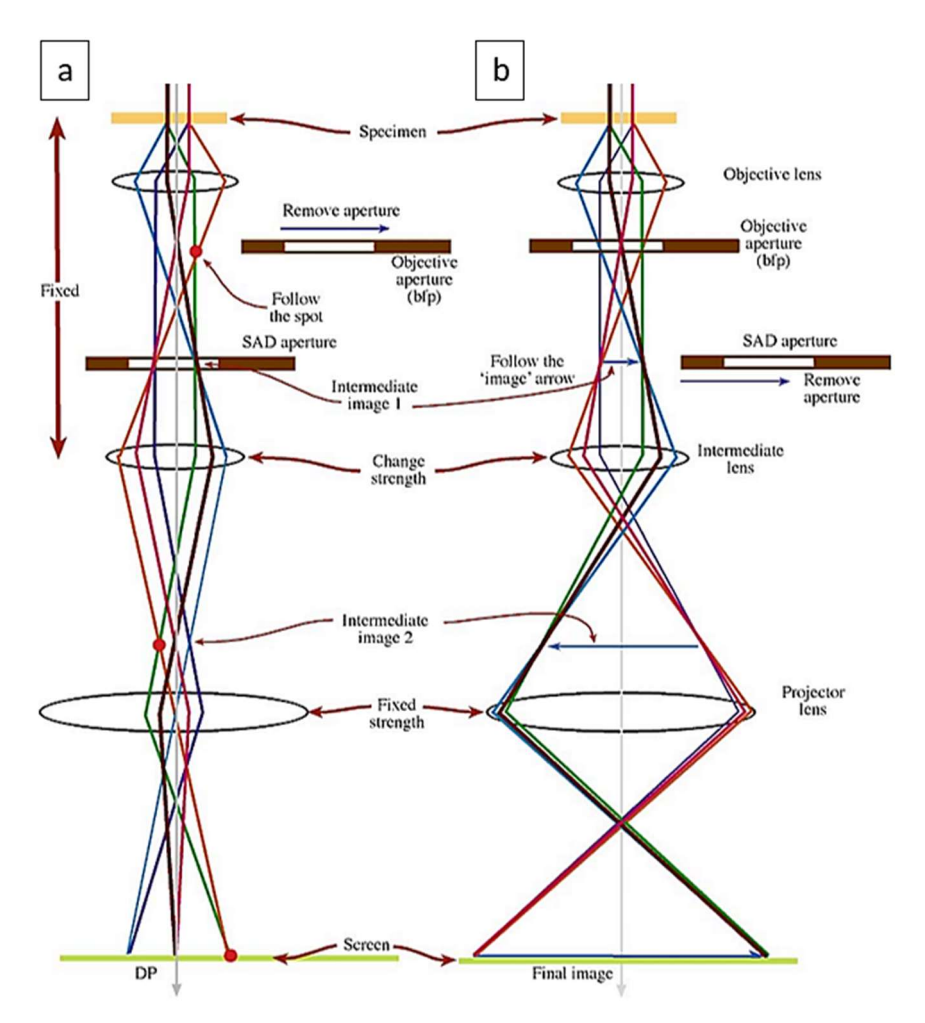


**Figure 20:** The most common operations in the TEM are *a*) the diffraction mode and *b*) the imaging mode [33].

For imaging the object the plane of the intermediate lens must be the image plane of the objective lens as illustrated in Figure 20*b*). By accomplishing that an image is projected onto the screen/detector. Applying an objective aperture located in the back focal plane (BFP) of the objective lens, additionally two modes being bright field (BF) and dark field (DF) can be adopted while imaging. BF imaging detects the direct beam electrons whereat DF images originate from scattered electrons. For diffraction mode the BFP of the objective lens needs to act as the object plane for the intermediate lens projecting the diffraction pattern onto the screen/detector visualised in Figure 20*a*) [33]. The specific diffraction used in this work is explained in the following.

### 3.8.1 Selected area diffraction

It is possible to record diffraction patterns by using a TEM as visualised in Figure 20a), called Selective Area Diffraction (SAD), where an advantage in comparison to the XRD is that an area of interest can be chosen to be analysed selectively by inserting an aperture illuminating just the desired area [34]. The aperture is usually located in the first image plane below the sample. The typical size of the area studied by SAD is a few hundred nanometres [31]. In this study this process was used to analyse the diffraction pattern and therefore the orientation of a single NP on a SiN<sub>x</sub> membrane TEM grid.

The diffraction pattern represents the angular distribution of intensities of the diffracted transmitted electrons through the sample. This diffraction process can be described by Braggs law already mentioned in Equation 4. The Ewald sphere is a helpful construction visualising the relation between the real and the reciprocal space illustrated in Figure 21 [33].

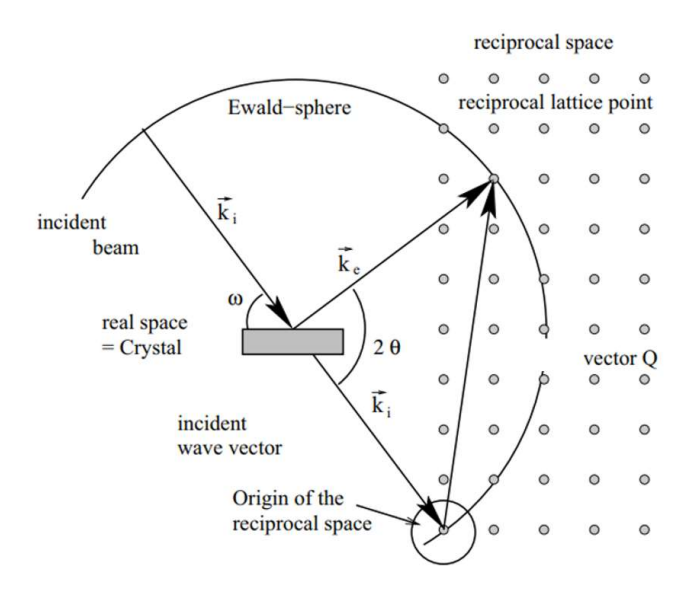


**Figure 21:** Ewald sphere construction with a radius related to the wavelength showing the incident wave vector  $k_i$  and diffracted wave vector  $k_e$  [35].

In Figure 21 the incident wave is represented by its wave vector  $k_i$  which length includes the reciprocal wavelength  $\lambda$  creating the radius of the Ewald sphere. If the Ewald sphere cuts a reciprocal lattice point the Laue condition is fulfilled. This means that  $k_i$  and  $k_e$  interfere constructively with  $g_{hkl}$  being the reciprocal lattice vector of the corresponding (hkl) lattice planes. By measuring this vector between the incident wave  $k_i$  and diffracted wave  $k_e$  the lattice spacing  $d_{hkl}$  can be calculated [36]:

$$k_i - k_e = g_{hk}$$
  $d_{hkl} = \frac{1}{|g_{hkl}|}$  (6)

Comparing the diffraction pattern to a simulated pattern, the crystal structure and orientation of the sample can be evaluated [33].

### 3.9 Specimen preparation and precalculations

The AuCu system is an interesting system for SSD, since a solid solution can be produced over the whole concentration range, as well as ordered phases can be produced by selective heating at moderate temperatures. In the following the sample preparation and precalculations are presented.

### 3.9.1 Sample preparation for layer deposition

The thin film is deposited on a crystalline sapphire ( $\alpha$ - $AI_2O_3$ ) substrate of size 5mm × 0.5mm (CrysTec Kristalltechnologie). Therefore, the sapphire substrate needs to be cleaned elaborately before depositing the AuCu bilayer thin film on top of it. The cleaning process is performed for avoiding inconsistencies and provide traceability. The cleaning process starts with an Isopropanol bath, next preserving the substrate in an ultrasound bath of Acetone for five minutes and finishing it with an Ethanol bath. Following the specimen are plasma cleaned with an Ar/O<sub>2</sub> (3:1) plasma for 10 min to remove organic residues.

### 3.9.2 Determination of thin film composition

AuCu bilayer thin films with a total thickness of *40nm* are deposited on sapphire substrates as displayed in Figure 22.



**Figure 22:** The total *40nm* AuCu layer on top of the sapphire substrate showing the order of each layer deposited.

First, a layer of copper was deposited and on top of it a layer of gold, illustrated in Figure 22, preventing the copper from oxidizing. By using a bilayer system in this work, a lattice match between the  $\alpha$ -Al<sub>2</sub>O<sub>3</sub> substrate and the thin film can be accomplished through variation of thickness ratio of each elemental layer. In order to achieve lattice matching which is equal to the minimization of the lattice mismatch, the d-spacing of the 220 planes of the NPs has to be equal to the substrate's 30-30 d-spacing (see Equation 2) [37]. Combining the lattice parameter of gold  $a_{Au} = 4.08 \,\text{Å}$  with the lattice parameter of copper  $a_{Cu} = 3.61 \,\text{Å}$  while alloying the emerging alloy's lattice parameter adjusts between those two. The necessary  $d_{220}$  spacing for matching is  $1.3746 \,\text{Å}$ . Using Equation 5 the corresponding lattice parameter is calculated to  $a = 3.89 \,\text{Å}$ .

An approximation of the lattice parameter of a bilayer film is calculated through the Vegard's law by using the parameters of the raw elements. Vegard's law describes the linear dependency of the lattice parameter a from the atomic concentration x of an alloy's component being Au and Cu [38].

$$a_{AuCu} = x_{Au} \cdot a_{Au} + x_{Cu} \cdot a_{Cu} \tag{7}$$

Although the Vegard's law enables a good approximation of the alloy's parameter it is not exact for metallic alloys. The accurate lattice parameter is rather a curve than a linear relation. The actual lattice parameter is expected in between the Bulk plot containing actual experimental data and Vegard's plot displayed in Figure 23 [38].

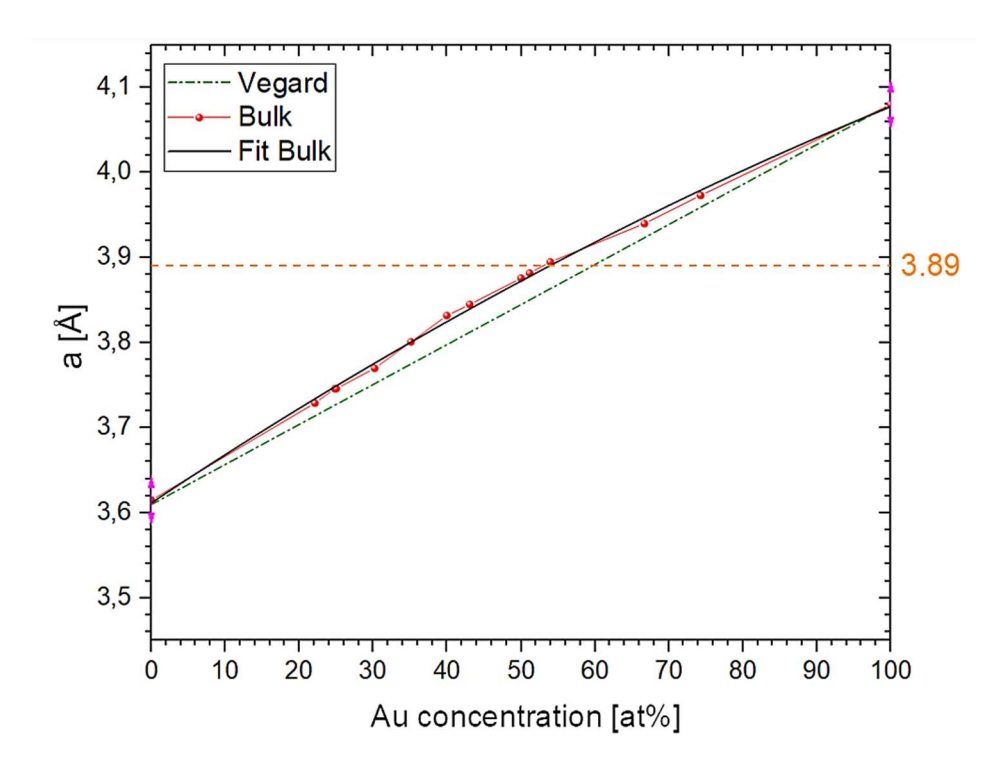


**Figure 23:**Evolution of the lattice parameter for AuCu alloys as a function of the Au concentration showing a deviation between the Vegard's prediction and the data for bulk alloys [12]. The line at a=3.89Å indicates the lattice parameter needed for lattice matching.

In this work several test series with varying concentrations but constant 40nm total film thickness were fabricated finding the ideal lattice match. At first the concentration of Au and Cu needed for lattice matching is calculated considering Vegard's law  $59.9~at.\%_{Au}$  listed in Equation 7 as well as considering the Bulk plot  $53.8~at.\%_{Au}$  in Figure 23 where the concentration was calculated by means of the Bulk fit equation.

The perfect lattice match is expected in the range of those two concentration calculations. Whereafter a whole concentration series was performed to create an own plot for determination of the ideal concentration for the lattice match. Therefore, the atomic percent of Au  $(at.\%_{Au})$  was varied in an interval of each  $20 at.\%_{Au}$  whereupon near the expected lattice match an interval of  $2 at.\%_{Au}$  is chosen as listed in Table 1.

In correspondence to the  $at.\%_{Au}$  the to deposited film thicknesses were detected by first calculating the volume percentage  $(vol.\%_x)$ .

$$vol.\%_{x1} = \left(1 + \frac{at.\%_{x2} \cdot m_{x2} \cdot \rho_{x1}}{at.\%_{x1} \cdot m_{x1} \cdot \rho_{x2}}\right)^{-1}$$
(8)

The atomic percent  $at.\%_x$ , the atomic mass  $m_x$  and the element's density  $\rho_x$  are inserted in Equation 8. The required film thickness is finally calculated by multiplying the  $vol.\%_x$  with the total film thickness  $d_{total}$ .

$$d_x = vol. \%_x \cdot d_{total} \tag{9}$$

In the following Table 1 all calculated  $at.\%_x$  and  $d_x$  are listed.

**Table 1:** Atomic percent and film thickness of Au and Cu is calculated for different concentrations adjusting the lattice parameter.

-40/ -	d . []	-40/ 0	d . []
at.% Au	<b>d</b> Au [nm]	at.% Cu	<i>d</i> Au [nm]
59.5	27.1	40.5	12.9
53.8	25	46.2	15
0	0	100	40
20	10.6	80	29.4
40	19.6	60	20.4
48	22.8	58	17.2
50	23.6	56	16.4
52	24.4	54	15.6
54	25.1	52	14.9
56	25.9	50	14.1
58	26.6	48	13.4
60	27.3	40	12.7
80	34.1	20	5.9
100	40	0	0

### 4. Results

The results of producing and analysing the specimen with the materials and methods mentioned in Chapter 3 are displayed in the following.

### 4.1 Thickness measurements with the AFM

The thicknesses of the films prepared via E-Beam evaporation are quantified by using the AFM as visualised in Figure 14. The reason for measuring the film thicknesses is to confirm the accuracy of the PVD film application. With the maintained data the height difference between the applied film and substrate is measured by the software Gwyddion. In this experiment the thickness of a pure Au layer, a pure Cu layer and a bilayer of both of those elements is measured. Additionally, a 40nm AuCu layer was dewetted for 300 s at a temperature of 600 °C and measured in the AFM as well. All samples mentioned before were measured by placing a scratch except for the dewetted sample due to the already existent holes. The intended layer thickness deposited by the E-Beam and the AFM-measured thickness is demonstrated in Figure 24. The dotted lines illustrate the intended layer thickness for deposition in the E-beam showing a good correlation with the data from the AFM measurements. That means that the layers deposited in the following experiments with the E-Beam were quite accurate and therefore traceable. Considering the sum of each measured Au and Cu single layer a measured thickness of about 42nm of the 40nm AuCu film should be received. Consequently, the measured minimal decline of the total 40nm film can be explained through the interdiffusion between Au and Cu. The dewetted sample with an initial layer thickness of 40nm shows an increase caused by the process of SSD, resulting from adding the material where currently the holes exist on top of the 40nm film.

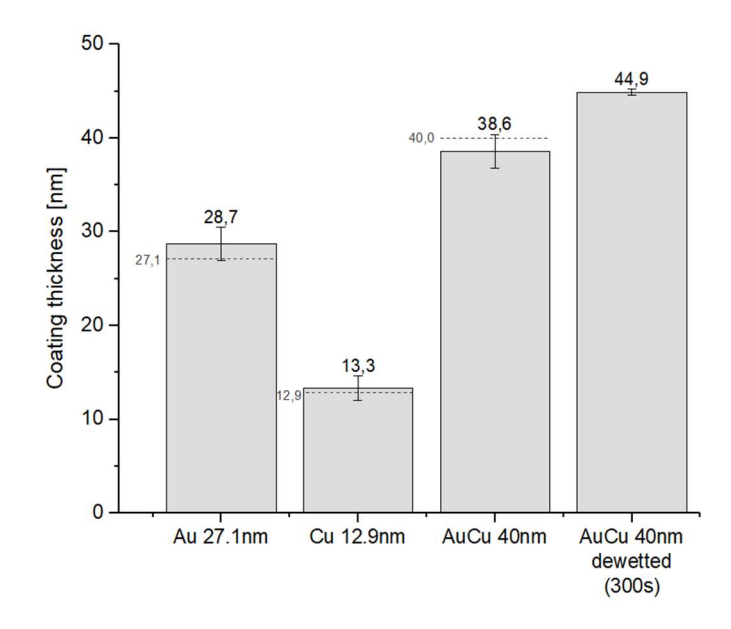


**Figure 24:** Film thickness measured by the AFM compared to the intended layer thickness marked with a horizontal line (---) showing a good correlation to the AFM measured thicknesses.

The height difference can be visualised very well by the three-dimensional illustration of the AFM data as shown in Figure 25. A 40nm AuCu sample is measured where the abrupt edge of the scratch is demonstrated. Also noticeable are some height peaks seen on the specimen's surface which leads to the assumption of the thin film's surface not being continuously even.

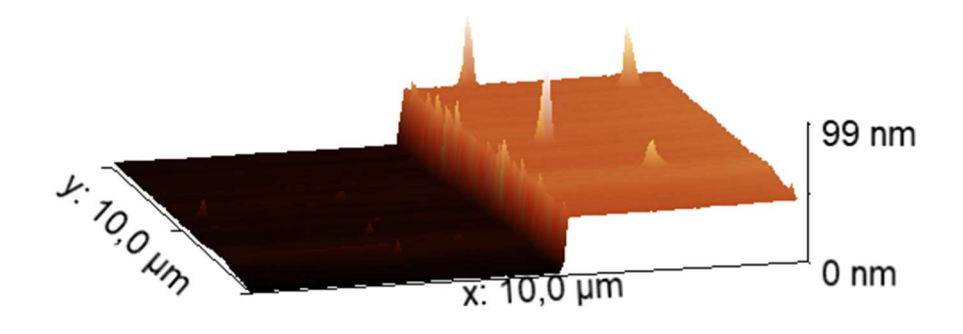


**Figure 25:** Three-dimensional AFM recording of a *40nm* AuCu layer illustrated with the software Gwyddion.

The dewetted sample is illustrated in Figure 26 in a *a)* two-dimensional (2D) and *b)* three-dimensional (3D) image where the dewetting is just in its initial state. On the side a coloured height scale is given which indicates that the black areas represent regions with lower height and therefore the substrate. At the edges of these holes the thin film is thicker pointed out through brighter spots which can be seen clearly in the 2D map in Figure 26*a*).

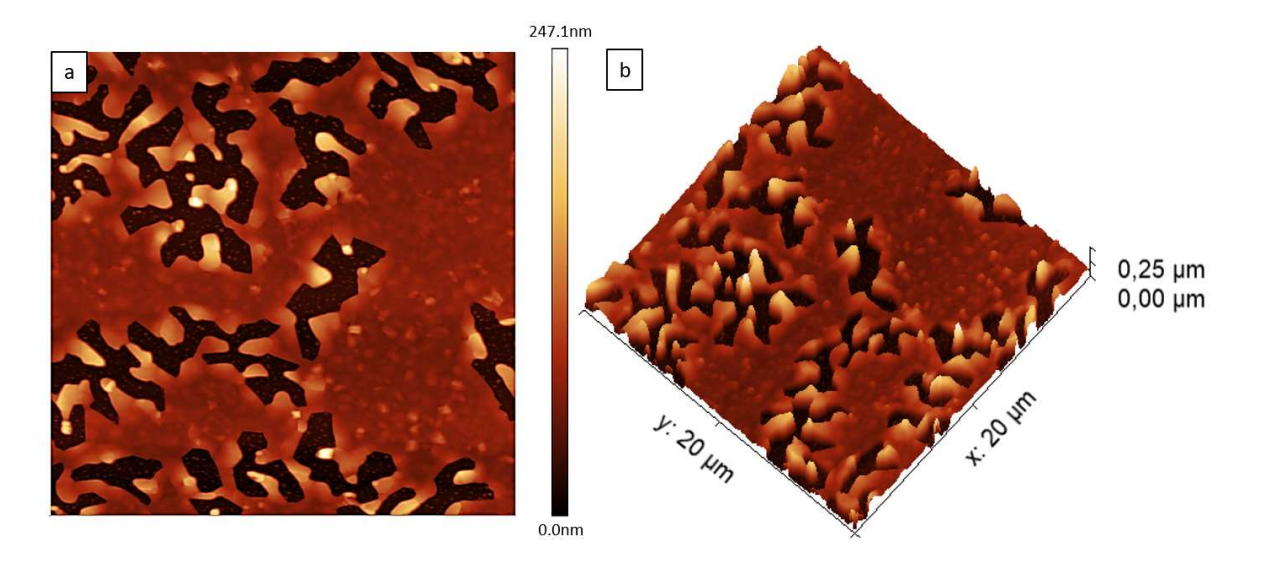


**Figure 26:** Height map of a SSD ( $T=600 \, ^{\circ}C \, t=300 \, s$ ) sample demonstrated *a*) in a 2D and *b*) in a 3D illustration visualising rim formation at the edges of the holes.

The thicker regions at the edges of the holes represent mass accumulation. This mechanism is already noticed by several sources and summarised in this work in the fundamentals in Chapter 2.1.2. Therefore, a rim formation is observed which is the underlying mechanism for mass retraction and thus SSD [1,2,5].

# 4.2 Variation of dewetting temperature and time

All experiments in the following are carried out with a constant concentration of  $59.5 \ at. \%_{Au}$  calculated by Vegard's law thus the parameters annealing time and temperature can be adjusted comparable.

#### 4.2.1 SEM characterization of SSD

Heating at temperatures of 600 °C, 700 °C, 800 °C and 850 °C were was performed where at the AuCu system finds itself in the solid solution in the phase diagram. The temperature of 850 °C is chosen close to the melting temperature of the AuCu alloy and is therefore the highest annealing temperature possible. Under these temperatures the samples are annealed at a time range from five to twenty minutes with an interval of five minutes choosing 300s, 600s, 900s and 1200s.

The annealing temperatures and times modified are illustrated in the dewetting map in Figure 27. This map shows a trend of the *40nm* AuCu film increasingly dewetting with higher time and temperature as expected. However, this trend is not followed perfectly, nevertheless the majority displays it. The samples at *600* °C and *700* °C after *900* s compared to the ones annealed for *1200* s underwent more dewetting which deviates from the trend. At *600* °C the dewetting is in its initial state and almost a continuous film is still present. Then continuously more dewetted area is seen where at *700* °C already particle like structures are formed. The instable fingering process is emerging at *800* °C after *300* s as well as at *700* °C after *300* s and *1200* s. These fingering structures are developing to particles due to the Rayleigh instability. At *800* °C already after *600* s the formation of elongated particles can be observed. Whereat *850* °C even after *300* s particles are formed that have a round shape.

Overall, the ideal temperature for the formation of particles proves to be 850 °C whereby the annealing time does not have a significant influence by analysing it with the Tabletop SEM. Further analysis of these specific samples is undertaken in the following.

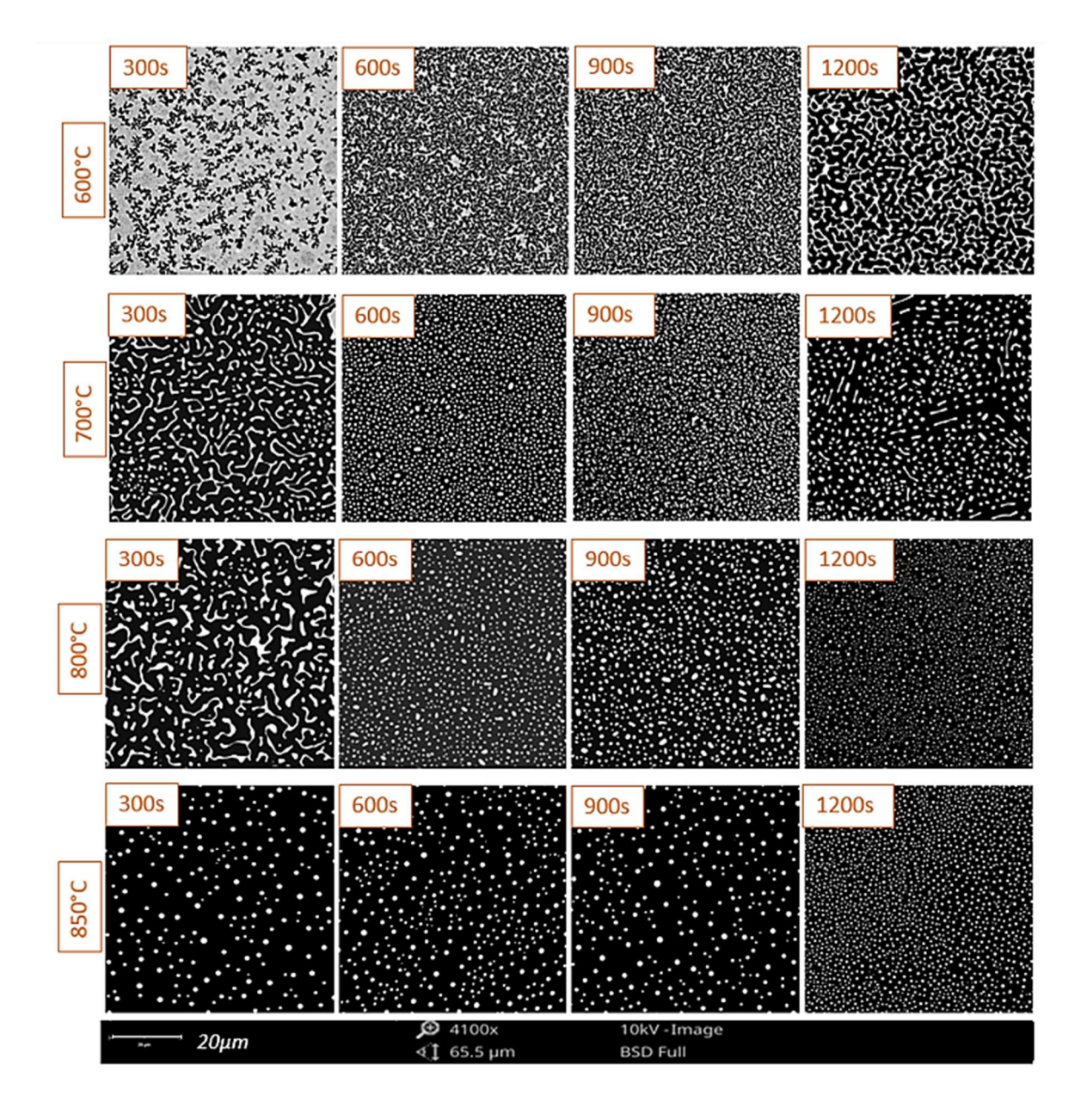


**Figure 27:** SSD map of AuCu *40nm* thin films at variating annealing times and temperatures showing a trend of increasing SSD with higher temperatures and longer annealing times.

A sample's SSD state can be visualised through the dewetted area (%area) calculated by means of the software ImageJ. It describes the thin film's area in relation to the total area. In the diagrams shown in Figure 28 the %area development of SSD throughout increasing annealing temperature and annealing times is visualised more clearly. The trend of increasing SSD with higher temperatures and longer annealing times results in decreasing %area. The 600 °C and 800 °C test series are a perfect example for a %area consistently decreasing with increasing time. The 700 °C test series just roughly follows the trend. At 850 °C the %area was expected to be consistent at the varying annealing times which is approximately confirmed for all times except the 1200 s. This assumption is made due to the already completely formed particles at low annealing times. After the particles are formed the SSD reached its energetically favourable state and no further fragmentation is expected. Also noticeable are the similar %areas with different annealing times at constant temperatures in Figure 28b). This shows the higher significance of annealing temperature for SDD, delivering the main initiation energy, than annealing time. Annealing time only has a greater influence at lower temperatures such as 600 °C where longer times are needed because the dewetting rate is lower. At higher temperatures the dewetting rate is high wherefore already at smaller annealing times the whole SSD process is completed.

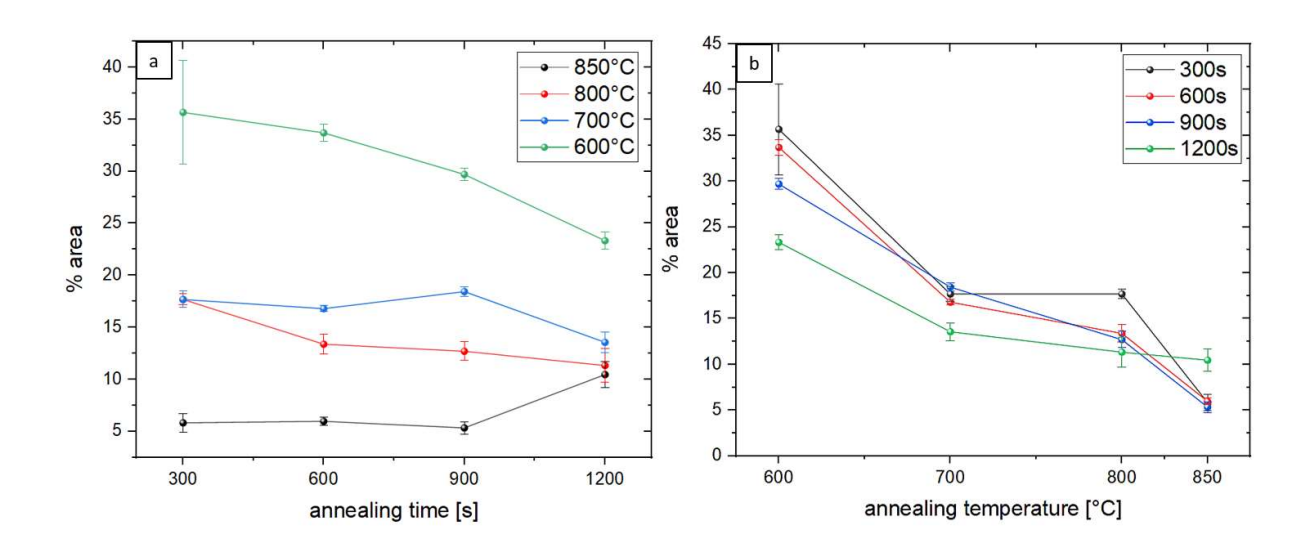


**Figure 28:** Changing *%area* through varying annealing temperatures and annealing times showing a trend of decreasing *%area* with *a)* increasing annealing time and *b)* higher temperatures.

The particles at 800 °C were visualised by means of the Tabletop SEM with 10 kV and imaging was performed with BSE in Figure 29. The images show several facets appearing on the particles.

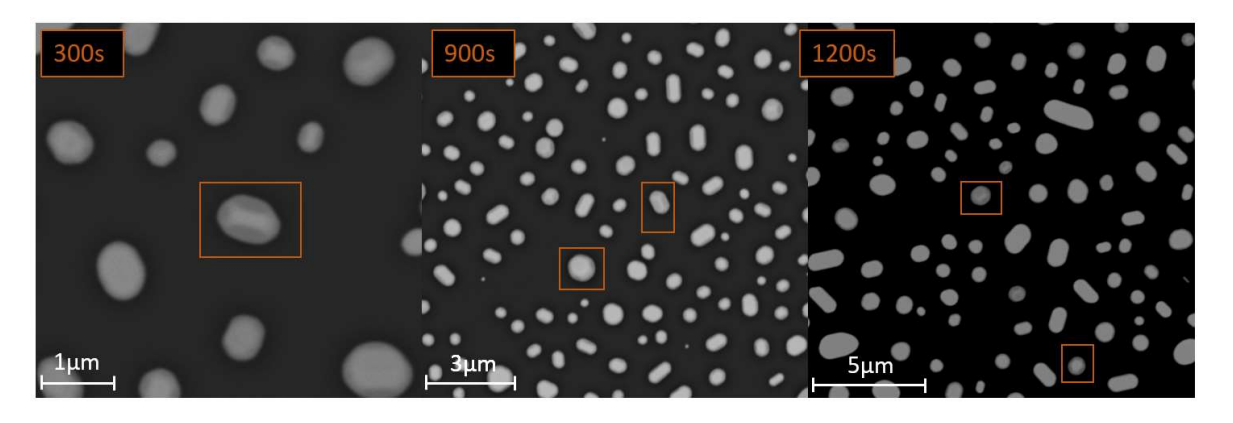
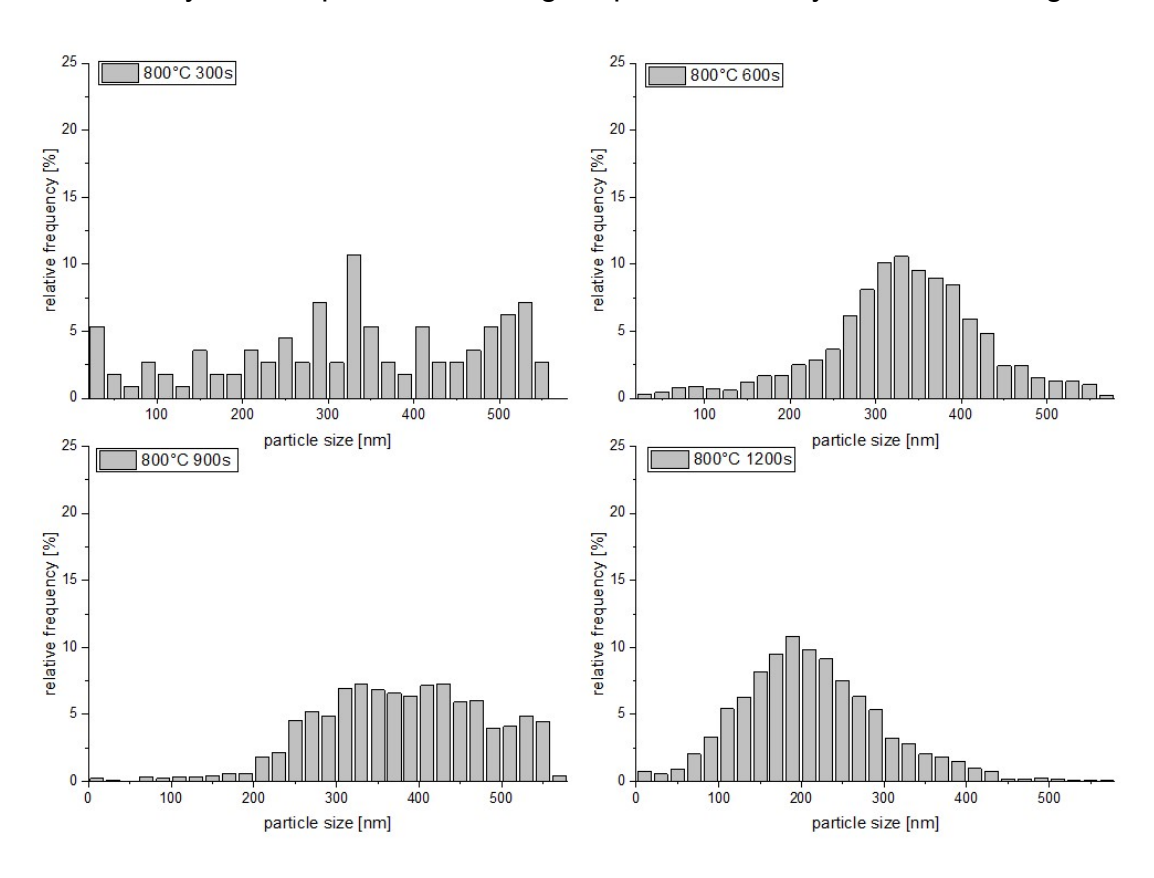


Figure 29: Facetted particles dewetted at 800 °C imaged with BSE in the Tabletop SEM.

Two types of facetted particles appear where the elongated ones have one rectangular plane oriented upwards and further four planes docking on the sides. On the other hand the rather round particles appear to have a hexagonal structure pointing upwards where six other planes are arranged at the sites. At different annealing times both kinds of particles are recognized.

The particle size distribution was detected by means of the software ImageJ and illustrated in Figure 30 for the  $800~^{\circ}C$  test series and in Figure 31 for the  $850~^{\circ}C$ . The relative frequency in % was plotted against the particle size in nm equal to the radius by assuming the circularity of particles in the calculations. Considering the  $800~^{\circ}C$  series in Figure 30 at  $300~^{\circ}s$  the average particle size is  $r_{300s} = 326,5nm \pm 149,2nm$ . A rather broad particle size distribution is noticeable which is additionally visualised through the high standard deviations when calculating the average size without showing any trend. At  $900~^{\circ}s$  annealing time an average particle size of  $r_{900s} = 379,6nm \pm 100,9nm$  showing a minimal Gaussian distribution without a distinct peak. Only  $600~^{\circ}s$  and  $1200~^{\circ}s$  show a clear Gaussian distribution with mean particle sizes of  $r_{600s} = 332,9nm \pm 93,1nm$  and at  $r_{1200s} = 219,2nm \pm 375,6nm$  indicating smaller particles at  $1200~^{\circ}s$ . The observation of the lower average particle size of the  $1200~^{\circ}s$  sample agrees with the previous notice of higher % area in Figure 28 caused by smaller particles with higher particle density visualised in Figure 27.



**Figure 30:** Relative frequency [%] plotted against the particle size [nm] showing the particle size distribution of the 800 °C series calculated by assuming the particles' circularity by means of the software ImageJ.

In Figure 31 the particle size distribution of the  $850\,^{\circ}C$  series is demonstrated neither showing a trend of the  $300\,s$  sample but revealing  $r_{300s}=436,2nm\pm135,0nm$  to be the average particle size. At this temperature the annealing times from  $600\,s$  to  $1200\,s$  all show a Gaussian distribution revealing its average particle size at  $r_{600s}=248,4nm\pm85,5nm, \quad r_{900s}=247,3nm\pm141,7nm \quad \text{and} \quad r_{1200s}=306,2nm\pm65,4nm.$  Whereupon the sample annealed for  $900\,s$  shows a bimodal particle distribution. Overall, these data shows no clear trend as well.

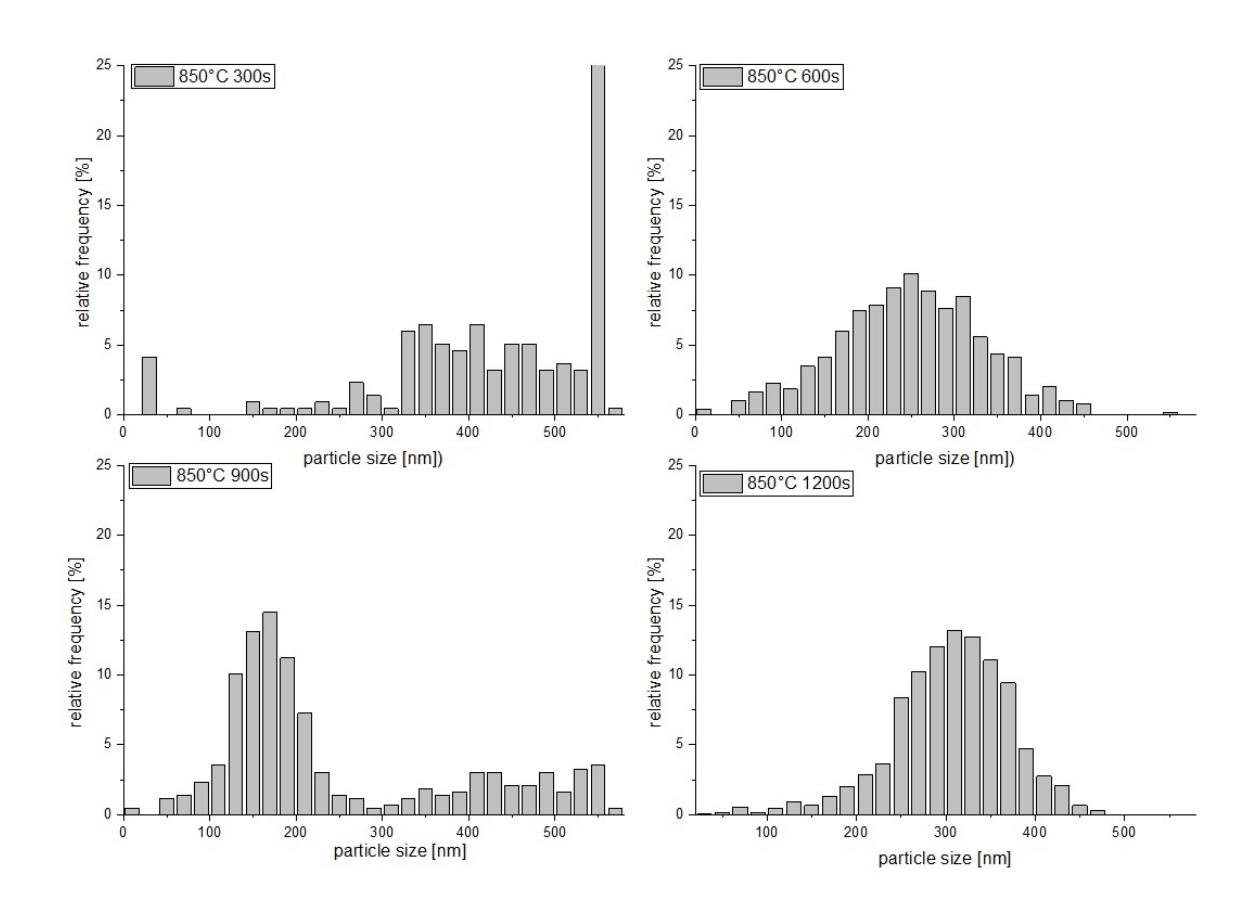


**Figure 31:**Relative frequency [%] plotted against the particle size [nm] showing the particle size distribution of the 850 °C series calculated by assuming the particles' circularity by means of the software ImageJ.

To determine the predominant directions of dewetting a Fast Fourier Transformation (FFT) was performed of a sample's SEM image finding itself in the initial state of SSD. When operating with a FFT on the SEM image of a 1200 s at 600 °C annealed sample clear lines appear showing the favoured directions in Figure 31a). According to the FFT the SSD is preferred in three directions discussed in Chapter 5.1.

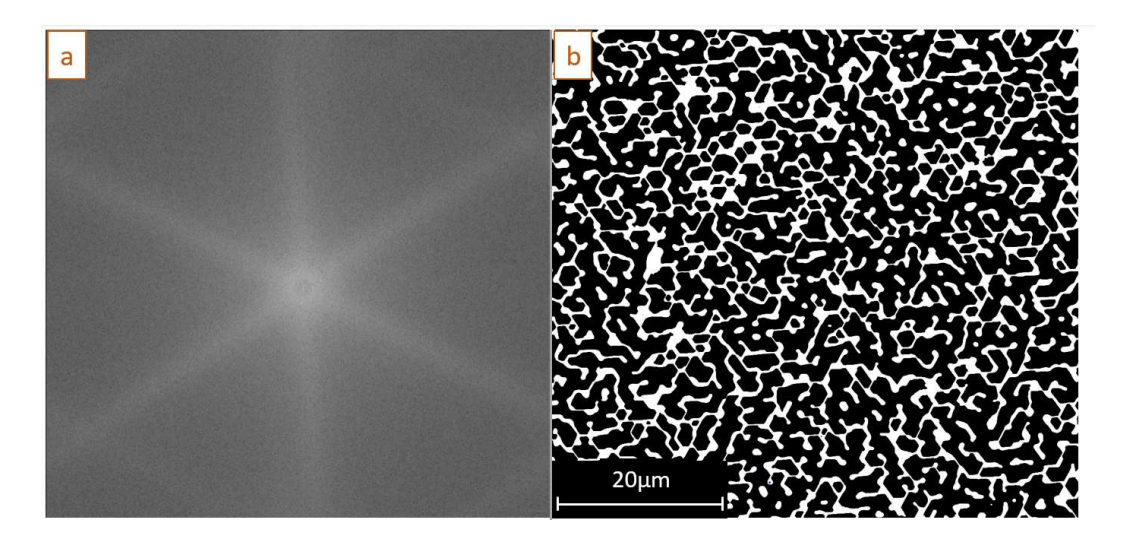


**Figure 32:** *a)* A FFT image of *b)* a dewetted AuCu specimen at 600 °C after 1200 s showing three predominant directions for SSD.

#### 4.2.2 EDX measurements

EDX measurements were performed using a voltage of 15~kV in the Tabletop SEM with all test series mentioned above. Qualitative maps were received showing the elemental distribution of the samples. The elements displayed in this sample are Aluminium and Oxygen sourcing from the  $Al_2O_3$  substrate as well as Copper and Gold sourcing from the thin film. The interaction volume intrudes deeper than the 40nm thin film or the formed particles wherefore the substrate can not be barred from the measurement. By Equation 3 the X-ray production is calculated for Au  $R_{Au} = 314nm$  and Cu  $R_{Cu} = 679nm$  for 15~kV showing much deeper thickness than the thin film. The main intention is to confirm that no segregation occurs and an alloy is present as suggested by the phase diagram. This expectation is confirmed by the EDX measurements where at varying times and temperatures consistently an alloy is visible. Examples for measured alloyed samples are illustrated in Figure 33 showing the substrate and the uniform distribution of Au and Cu at the film area at  $600~^{\circ}C$  and  $800~^{\circ}C$  after an annealing time of each  $600~^{\circ}S$ .

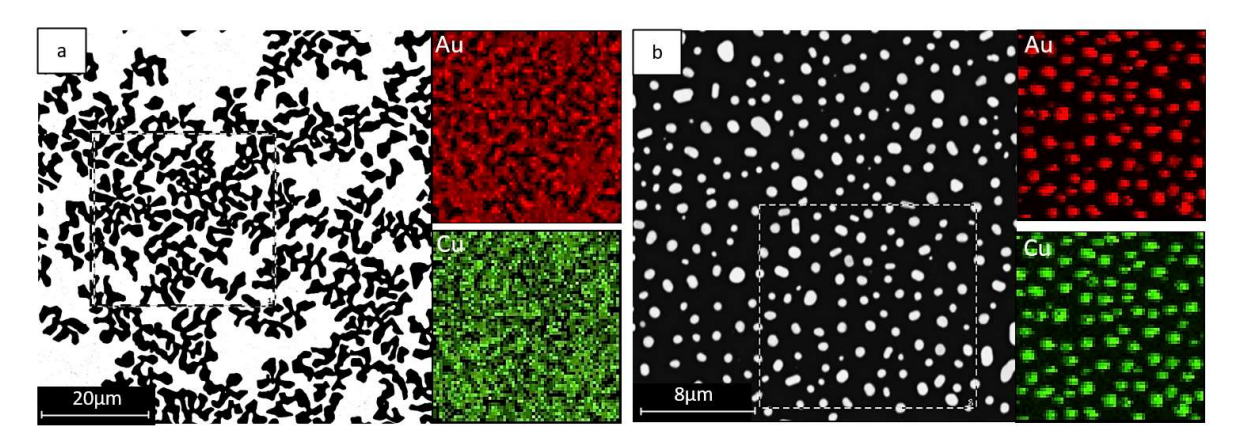


**Figure 33:** EDX maps of Au (red) and Cu (green) in the Tabletop SEM on a *40nm* SSD AuCu thin film at *a) 600 °C* and *b) 800 °C* for 600 s showing in both samples a uniform distribution of Au and Cu and therefore a consistent AuCu alloy.

# 4.3 Characteristics of AuCu particles

The particles characterized in the following were annealed under the determined ideal temperature of  $850~^{\circ}C$  and analysed by SEM, EDX and XRD. On the one hand the concentration calculated using Vegard's law described in Equation 7, which was already utilized in 4.2, is analysed. On the other hand another concentration was investigated calculated by Bulk ( $53.8~at.\%_{Au}$ ) due to the assumption that the perfect lattice match lays in the range to either of these calculated concentrations.

# 4.3.1 SEM characterization of particles

Round particles are observed when annealing the AuCu thin film at  $850\,^{\circ}C$  at any of the performed annealing times. The concentration variation between Bulk and Vegard does generally not lead to a change in the *%area* displayed in Figure 34 or in the particles' shape. As mentioned before in Chapter 4.2.1 a deviation emerges at  $59.5\,at.\%_{Au}$  after an annealing time of  $1200\,s$  resulting in a significant increase of *%area*. Therefore, another annealing time of  $120\,s$  was tested to determine if even short times lead to perfectly round particles. Confirming this assumption Figure 34 shows no significant change of *%area* is tabulated.

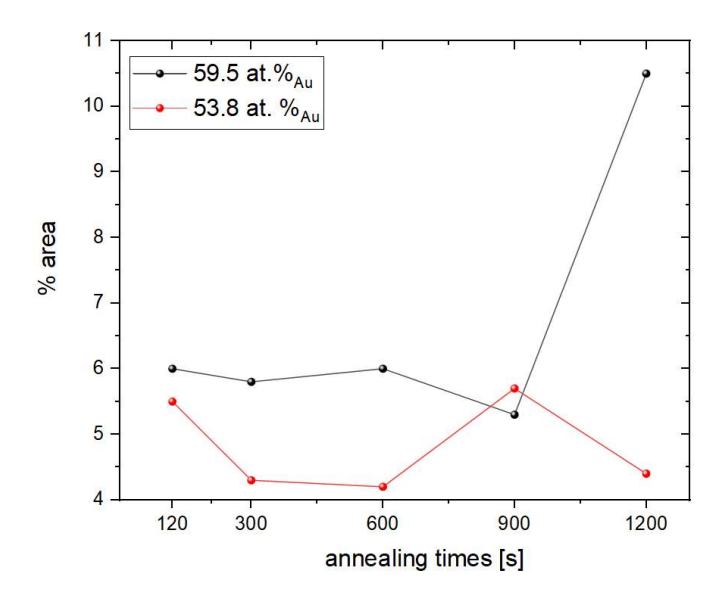


**Figure 34:** Comparison of dewetted *%area* between two concentrations calculated considering Vegard's law ( $59.5 \text{ at.}\%_{Au}$ ) and Bulk ( $53.8 \text{ at.}\%_{Au}$ ) showing an approximate constant *%area* with changing annealing times except the deviation at  $59.5 \text{ at.}\%_{Au}$  1200s.

Observing the SEM images recorded with a TLD detector surface topography can be evaluated where in Figure 35a) the particles seem to be spherically shaped and not flat. Additionally, a SEM image was recorded at the same position with a CBS detector illustrated in Figure 35b) in which the particles' faceting is visual.

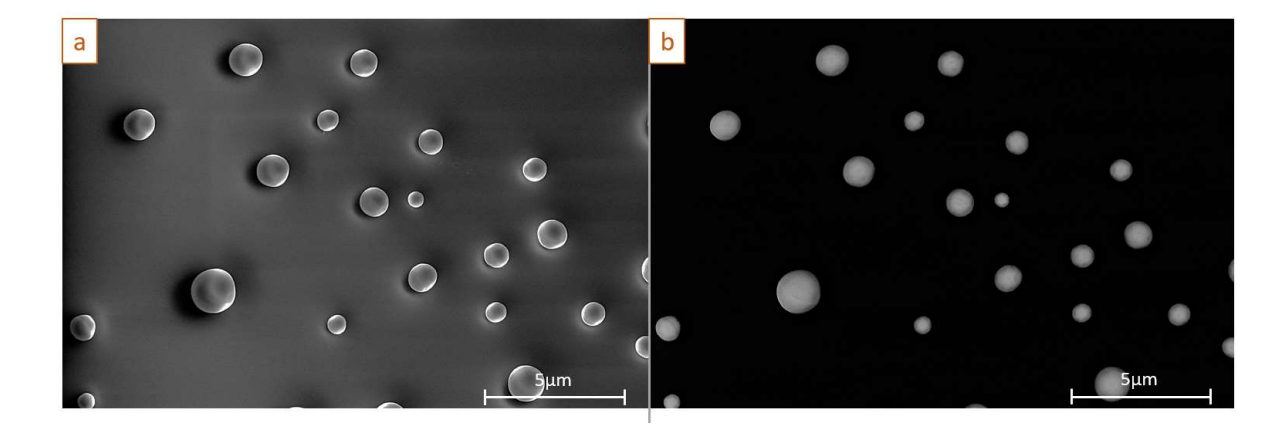


**Figure 35:** SEM image with *a*) a TLD illustrating the spherical shape of particles and with *b*) a CBS detector showing the faceting of particles of a 850 °C 300 s 59.5 at. %<sub>Au</sub> sample.

### 4.3.2 EDX measurements

To verify the composition of the particles EDX measurements were performed in the SEM. The measurements show in Figure 36 the successful formation of an AuCu solid solution since Au and Cu are homogeneously distributed in the elemental maps. With varying annealing times and concentrations the AuCu alloy remains the same. Point measurements were performed and discussed in Chapter 5.3.1.

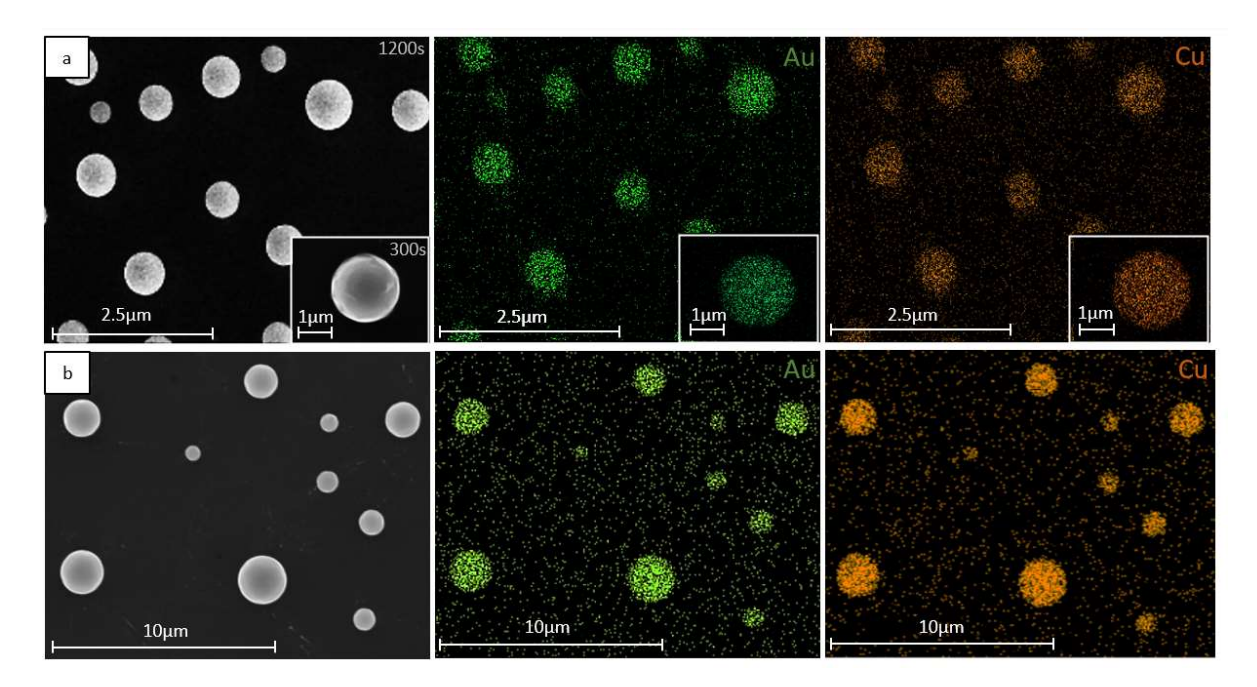


**Figure 36:** Qualitative EDX maps of a *a*) 59.5 at.%<sub>Au</sub> sample at annealing times of 300 s and 1200 s and a *b*) 53.8 at.%<sub>Au</sub> sample annealed at 120 s, illustrating the Au and Cu concentrations of several and one single particle revealing a homogeneous distribution and therefore the existence of an alloy.

### 4.3.3 SEM characterization of faceting

Regarding the fields of applications where these NPs can be implemented the faceting is an important attribute. The influence of the annealing time on the faceting as well as the general faceting of the particles is investigated in the following. The facets can be analysed in the Helios Nanolab SEM due to its higher resolution than the Tabletop SEM. The images lead to an assumption that an increasing annealing time at 850 °C does not significantly change the faceting of the particles. The expected OOP texture is the (111) orientation pointing upwards as mentioned before in the fundamentals under 2.3. There are three types of particles on the substrates that are observed in the SEM for both concentrations Bulk and Vegard. These three types are emphasized by coloured circles around them in Figure 37 revealing the (111) oriented particles in red, tilted particles in blue and particles with grain boundaries in green.

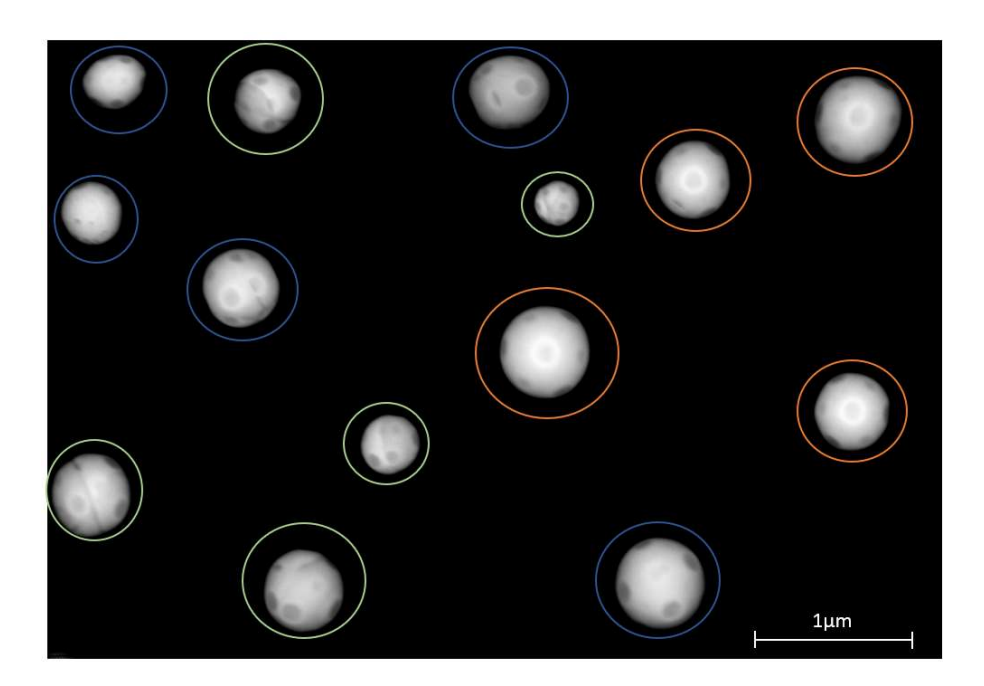


**Figure 37:** SEM picture in the FIB with a CBS detector of faceted particles on a 850 °C 1200 s 59.5 at.  $\%_{Au}$  sample showing the existence of three types of particles the most important (111) oriented particles (red), the tilted particles (blue) and the particles with grain boundaries (green).

The (111) oriented particles are the energetically preferred ones explained in the fundamentals under 2.3 and therefore closer illustrated in Figure 38. In this regard the assumed (111) plane is visible through the hexagonal structure appearing on the surface becoming obvious by the six impressions on the sides as displayed in Figure 38a) or it is visible when showing a triangular shape appearing on top of the particle seen in Figure 38b) and c).

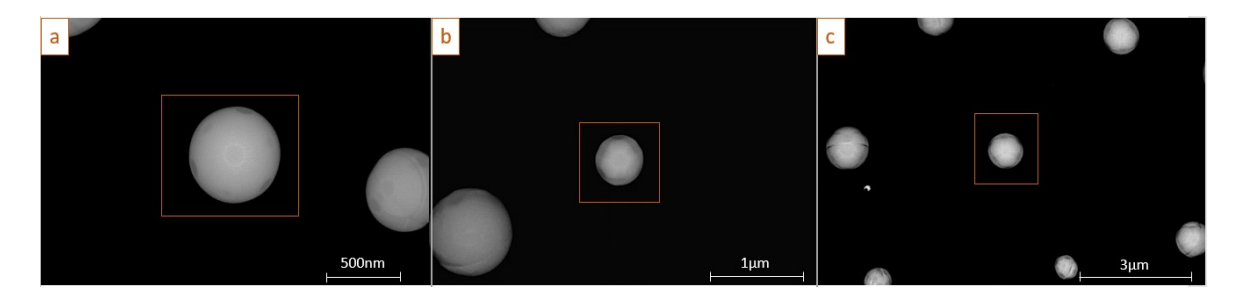


**Figure 38**: (111) oriented particles of a) 59.5 at.  $\%_{Au}$  1200 s, b) 59.5 at.  $\%_{Au}$  120 s and c) 53.8 at.  $\%_{Au}$  900 s samples revealed by a) six impressions on their sides or b) and c) a triangular shape on top of them.

Conspicuous are the SEM images of the  $53.8~at.\%_{Au}$  Bulk concentration after 600 s and 1200~s of annealing. There the particles seen in Figure 39 have slight divergences in comparison to the pictures of other annealing times as well as other concentrations. It appears like more facets evolve on the particles surface throughout maintaining the (111) orientation. Assuming that the facets are highly indexed this can be an advantage for the catalytic processes because these are more reactive due to less binding partners.

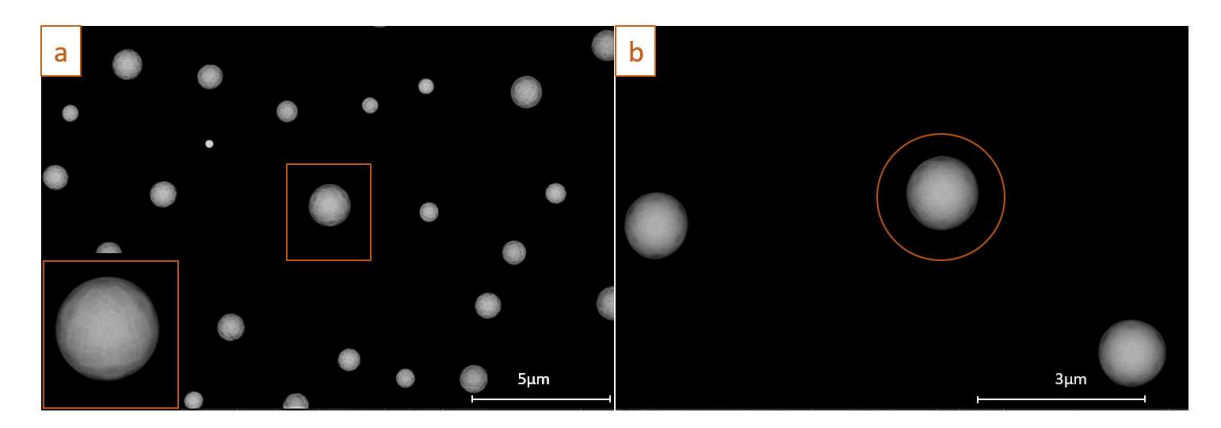


**Figure 39:** SEM images of deviating particles detected with a CBS of a *a) 1200* s annealed and *b) 600* s annealed  $53.8~at.\%_{Au}$  sample showing more facets than particles at  $59.5~at.\%_{Au}$  throughout maintaining the (111) orientation.

### 4.3.3 XRD measurements

For determination of the exact particles' orientation on top of the substrate the XRD visualised in Figure 40 was taken of *a*) Vegard and *b*) Bulk concentrations. The peaks were fitted by a Pseudo Voigt approximation with the software Lipras [39] which can be found in the appendix (Figure A1 and Figure A2).

As assumed before in the SEM images the (111) orientation at a degree of  $2\theta=40.75^\circ$  is the preferred one in both concentration series. This peak stands out the most next to the Al<sub>2</sub>O<sub>3</sub> (0006) peak at an angle of  $2\theta=41.68^\circ$ . However, a small (200) AuCu peak appears at  $2\theta=46.60^\circ$  indicating with its peak height that a small amount of the particles do not reach the most ideal (111) orientation. The peak vanishes at the Bulk concentration after 1200 s of annealing. Noticeable is also the Au (111) peak appearing at  $2\theta=38.18^\circ$  with a small intensity suggesting that a small amount of Au segregation at the surface and/or interface takes place. Contrariwise the XRD data is plotted logarithmically which means that the low intensity peaks occurring result from a considerably small number of particles or highly thin films. At the Bulk concentration an integrated peak is seen from 300 s to 900 s merging into the Au (111) peak suggesting formation of high Au concentrated AuCu (111) particles in low numbers.

Another occurring attribute is the total of AuCu (111) and AuCu (200) peaks shifting to the sides as seen clearly for both concentrations at an annealing time of 120 s and 1200 s.

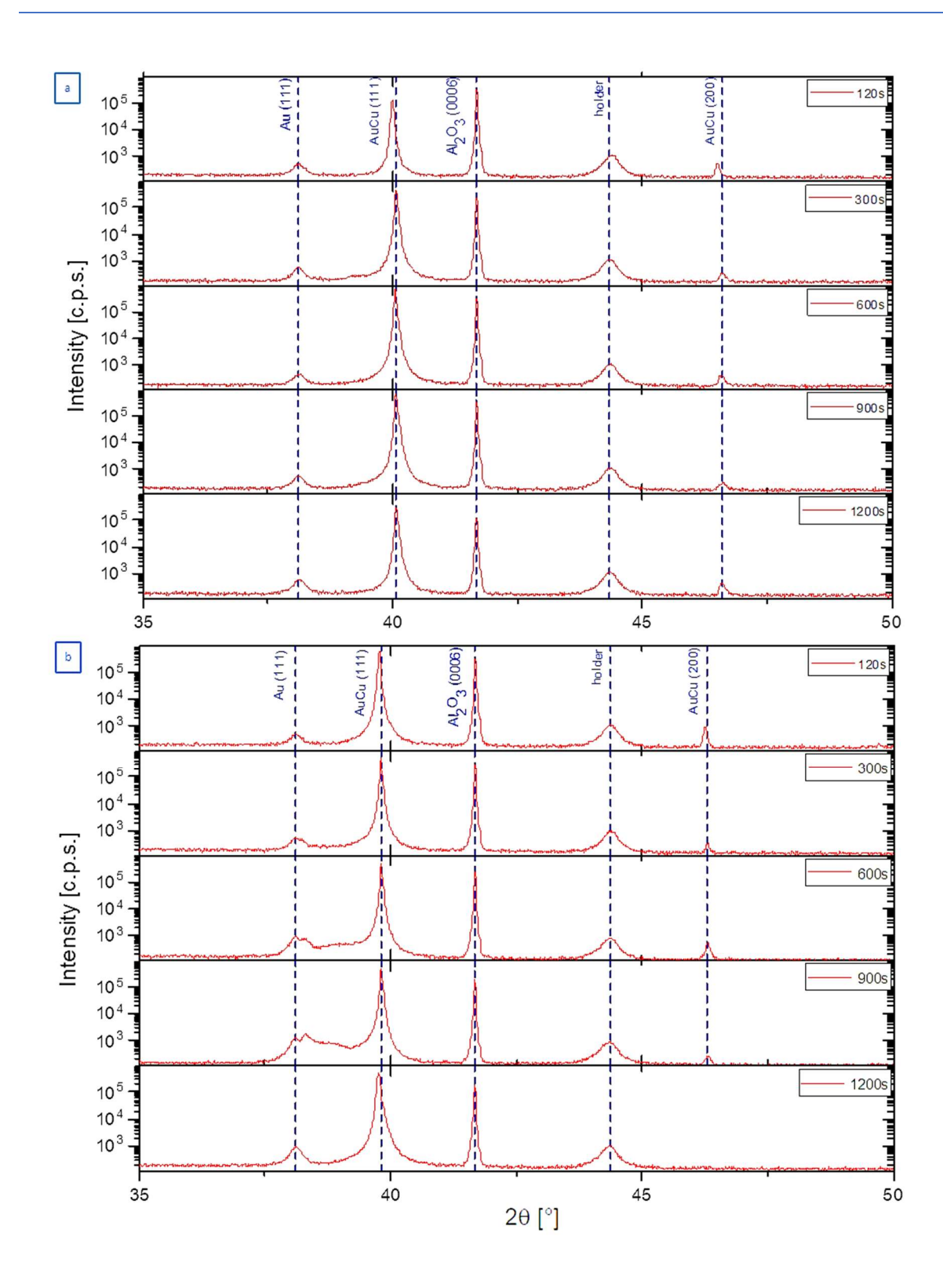


**Figure 40:** XRD measurements of the *a)* Vegard and *b)* Bulk concentrations with labelled peaks showing a predominant *(111)* orientation.

### 4.3.4 Lattice parameter calculation

The lattice of the NPs is aimed to be matched to the substrate's one. This is performed by changing the Au concentration meaning that the film thickness of each Cu and Au layer is varied in the range of the total *40nm* film thickness. The lattice parameter of the thin film's elements as well as the substrate's one is introduced in Chapter 3.9.2.

Additionally, to the determination of the particles' orientation the lattice parameter can be calculated by means of the XRD data. This is calculated via the Bragg's law listed in Equation 4 and the converted Equation 10 mentioned subsequently.

$$a = d_{hkl} \cdot \sqrt{h^2 + k^2 + l^2} \tag{10}$$

The lattice parameter of both Vegard  $a_{Vegard}=3.92\,\text{Å}$  and Bulk  $a_{Bulk}=3.90\,\text{Å}$  concentrations were calculated. Comparing those with the intended lattice parameter of  $a=3.89\,\text{Å}$  the one calculated with Vegard is  $\Delta a_{Vegard}=0.03\,\text{Å}$  higher whereby the Bulk one is  $\Delta a_{Bulk}=0.01\,\text{Å}$  higher. This shows that the Bulk concentration is close to the matching lattice parameter.

# 4.4 Adjustment of the lattice parameter

In previous experiments the concentration was calculated by the equation of the Bulk plot ( $53.8~at.\%_{Au}$ ) where the lattice parameter only deviated  $\Delta a = 0.01~\text{Å}$  from the intended parameter of a = 3.89~Å. This Bulk plot originates from experimental data wherefore an own concentration series was performed. The details of the to be analysed concentrations are listed in the Table 1 as well as the exact concentrations measured from  $0~at.\%_{Au}$  to  $100~at.\%_{Au}$ . The whole concentration series was annealed with the ideal parameters of  $850~^{\circ}\text{C}$  under 120~s identified in the experiments beforehand.

EDX point measurements were performed with the Tabletop SEM calculating the average of four measurements on the sample. The data received is compared to the intended *at.*%<sub>Au</sub> concentration showing rather lower *at.*%<sub>Au</sub> than the intended concentrations in Table 2.

**Table 2:** The intended  $at.\%_{Au}$  concentration compared to the EDX point measurements showing slight deviations whereby the EDX measurements shows rather a lower  $at.\%_{Au}$  than intended.

at.% Au		EDX data [at.% Au]	
-	20	18.6 ± 0.7	
	40	$36.5 \pm 0.4$	
	48	46.0 ± 0.7	
	50	48.0 ± 0.7	
	52	48.2 ± 1.1	
	54	52.1 ± 1.0	
	56	54.4 ± 1.3	
	58	54.7 ± 0.1	
	60	57.5 ± 0.4	
	80	79.4 ± 1.5	

The SEM images are illustrated in Figure 41 showing a similar state of SSD from Au concentration up to  $60~at.\%_{Au}$ . Going to higher concentrations of  $80~at.\%_{Au}$  a decrease is noticeable while for pure Au still a relatively continuous film can be found.

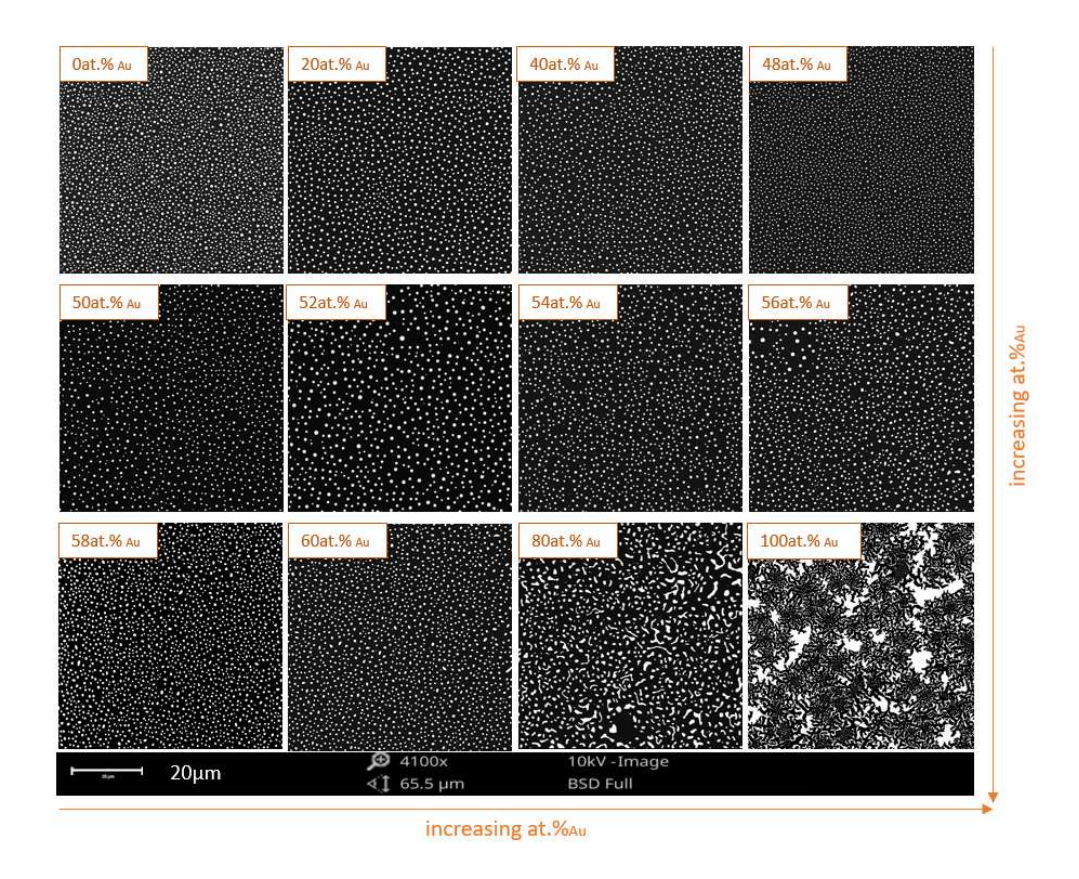


**Figure 41:**SEM pictures of the SSD state of AuCu *40nm* thin films at variating *at.*%<sub>Au</sub> concentration annealed at constant *850* °C for *120 s* showing decreasing SSD with high at.%<sub>Au</sub> where concentrations of *0-60 at.*%<sub>Au</sub> show a similar SSD state.

To confirm the visual SSD state in the SEM images of the samples the *%area* is detected by the software ImageJ for the concentration series and illustrated in Figure 42. The trend already assumed before considering the SEM images corresponds with the plotted *%area*. The dewetted area remains approximately the same from 0 at. $\%_{Au}$  to 60 at. $\%_{Au}$  whereafter the %area increases rapidly at 80 at. $\%_{Au}$  and 100 at. $\%_{Au}$ .

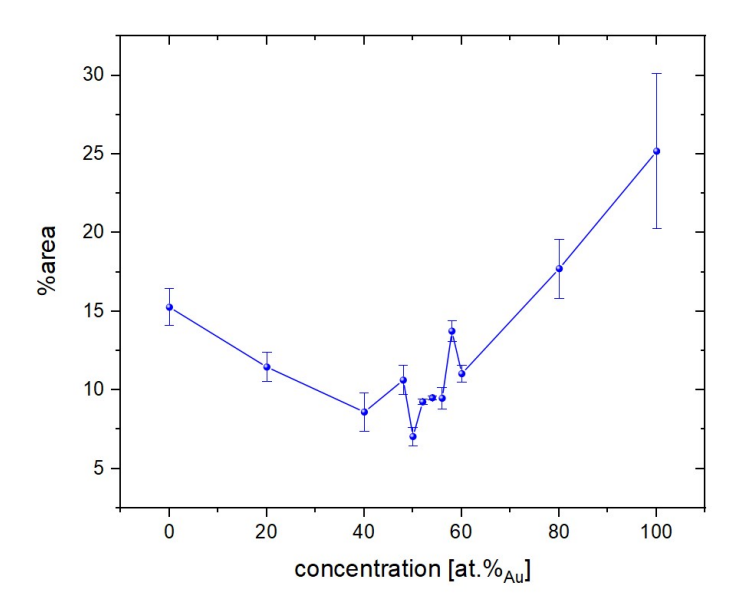


**Figure 42:** Behaviour of the SSD with increasing Au concentration demonstrated by the %area. At a range between 0 at.%Au and 60 at.%Au the dewetted area stays approximately the same whereupon with high Au concentration from 80 at.%Au the %area increases rapidly.

#### 4.4.1 XRD measurements

Thereafter the dewetted samples were analysed by the XRD where the data obtained is shown in Figure 43.

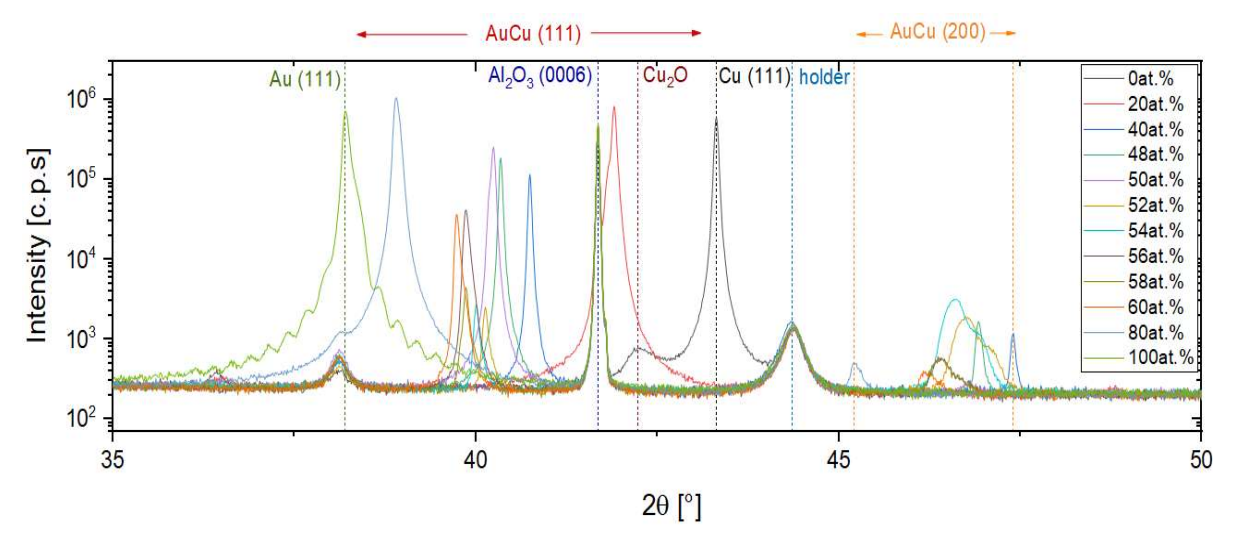


**Figure 43:** XRD data of the concentration series from 0 -100 at.  $%_{Au}$  showing a shift of the (111) and (200) peak to higher angles with decreasing at.  $%_{Au}$  and texture loss at 52 at.  $%_{Au}$  and 54 at.  $%_{Au}$  sample.

Comparing to the XRD data obtained before with the Vegard and Bulk concentration in Figure 40 the same peaks of Au (111), AuCu (111), Al<sub>2</sub>O<sub>3</sub> (0006) and AuCu (200) are appearing. Additionally, a Cu (111) peak emerges at a degree of  $2\theta=43.32^{\circ}$  assigning it to the sample with the pure 40nm Cu layer in front of which a Cu<sub>2</sub>O appears. The pure gold layer of 100 at.  $\%_{Au}$  illustrates an intense Au (111) peak showing oscillating runout called Laue fringes. This occurs when the thin film is still situated in the initial SSD and no particles are build yet. Due to lower surface energy of pure Au either longer annealing times, higher annealing temperatures or thinner films are required. Nevertheless, at concentrations from 40 at.  $\%_{Au}$  to 60 at.  $\%_{Au}$  an almost equal low intensity Au (111) peak is displayed at  $2\theta=38.14^{\circ}$ . Comparing the 100 at.  $\%_{Au}$  to the Au (111) peak at 80 at.  $\%_{Au}$  shifting is observed of approximately  $\Delta 2\theta=0.74^{\circ}$ . The peaks are shifted towards higher angles with a

decreasing amount of gold concentration. Therefore, the AuCu (111) peak varies depending on the concentrations in the range between the pure Au and pure Cu (111) peaks. Noticeable are especially the concentrations of 52 at.  $\%_{Au}$  and 54 at.  $\%_{Au}$  where at the AuCu (111) peak a high intensity loss is observed whereby at AuCu (200) a higher as well as broader peak is demonstrated in comparison to the other concentrations. Therefore, texture loss of (111) oriented particles is observed especially at these two concentrations. Regarding the AuCu (200) peak, also shifting with the same trend is observed with changing concentration at a range of  $2\theta = 45.28^{\circ} - 47.41^{\circ}$ .

In the following the corresponding lattice parameters to each concentration was calculated according to Equation 10.

**Table 3:** The lattice parameters corresponding to each atomic concentration measured in the XRD test series.

<b>at</b> .% Au	lattice parameter a [Å]
0	3.62
20	3.76
40	3.84
48	3.87
50	3.88
52	3.89
54	3.91
56	3.92
58	3.92
60	3.93
80	4.01
100	4.09

In Table 3 the calculated lattice parameters are listed where the measured lattice parameter of the pure elements suit the official ones mentioned in 3.9.2 really well assuring that the whole measurement is traceable. Considering that the Au lattice parameter is greater than the Cu one, the emerging lattice parameter of the AuCu alloy is increasing with increasing Au concentration. The closest approach to the

intended lattice parameter is the parameter a = 3.89 Å at a concentration of  $52 \text{ at.} \%_{Au}$ . With this concentration nearly a lattice match is obtained.

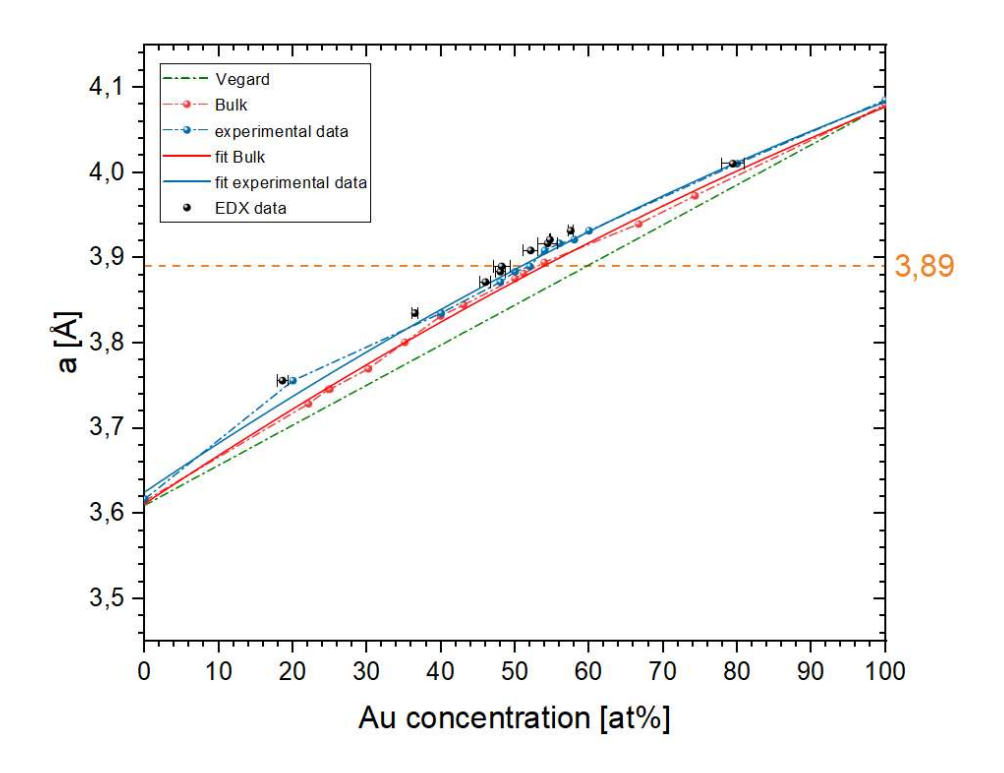


**Figure 44**: Experimental data illustrating the behaviour of the lattice parameter with increasing  $at.\%_{Au}$  compared to Bulk and Vegard. The experimental data matches the Bulk plot closely especially in the region of the lattice match highlighted with a horizontal line at a=3.89 Å approximating the data with EDX point measurements.

Figure 44 displays the nominal experimentally gained data of the concentration series with the data obtained through Bulk and Vegard visualising that the Bulk plot already offers a good estimation of the lattice parameter behaviour depending on the *at.*%<sub>Au</sub> especially at the area of the lattice match concentration. Additionally, the quantified data was determined by EDX point measurements listed in Table 3 often approaching the measured data to the Bulk plot.

# 4.5 Ordered phases in particles

The AuCu system forms ordered phases when following the solid solution region to lower temperatures. Especially interesting are the AuCuI and AuCuII ordered phases at a concentration of  $50~at.\,\%_{Au}$  displayed in the phase diagram in Figure 9. As visualised in the phase diagram both phases hold an  $L1_0$  structure starting at  $410~^{\circ}C$  with AuCuII to  $385~^{\circ}C$  reaching AuCuI at even lower temperatures. Under  $385~^{\circ}C$  a tetragonal structure exists whereupon at a range between  $385~^{\circ}C$  -  $410~^{\circ}C$  a similar tetragonal system with a superstructure exists forming domains [15]. These two ordered phases were generated in the AuCu particles by firstly producing them as usual under  $850~^{\circ}C$  for 120~s. For formation of the ordered phases the particles were cooled down directly from  $850~^{\circ}C$  to either  $400~^{\circ}C$  (sample1) or  $350~^{\circ}C$  (sample2) for both to achieve tetragonal crystal systems. The samples were postannealed for two hours to ensure sufficient time for the ordered phases to build.

#### 4.5.1 XRD characterization

The particles were analysed with XRD to provide data of the crystallographic orientation and the lattice parameter. Figure 45 displays all peaks registered compared with a XRD of 50~at.  $\%_{Au}$  particles without an ordered phase (sample3). The peaks were determined considering a tetragonal unit cell with the same dimensions of a fcc unit cell enabling comparison with the XRD data discussed before. Otherwise, a smaller unit cell could be chosen exhibiting a smaller lattice parameter of  $a' = \frac{a}{\sqrt{2}}$ . The AuCu (110)  $(2\theta = 31.65^\circ)$  and AuCu (201)  $(2\theta = 52.32^\circ)$  peaks only appear at sample2 yet showing low intensity. As in the previous XRD measurements a pure Au (111) peak is observed at the same degree for all samples. The AuCu (200) peak at  $2\theta = 45.66^\circ$  is only observed at the samples with ordered phases as well as the AuCu (002) peak at approximately  $2\theta = 49.41^\circ$ . Right next to the AuCu (200) peak of the ordered phases the AuCu<sub>fcc</sub> (200) of the cubic system occurs at  $2\theta = 46.60^\circ$ . However, the most important peak with the highest intensity

is the AuCu (111) peak of the ordered phases where in that range the AuCu<sub>fcc</sub> (111) peak of the fcc system occurs. Therefore, this range is observed in more detail in a close-up in Figure 45. Noticeable is especially the double peak of sample1 separating in about  $2\theta = 40.20^{\circ}$  and  $2\theta = 40.29^{\circ}$  peaks. The first peak is located nearby the AuCu<sub>fcc</sub> (111) peak of the fcc system of sample3 whereby second peak almost overlaps with the  $2\theta = 40.37^{\circ}$  with the AuCu (111) peak of the ordered phases at sample2.

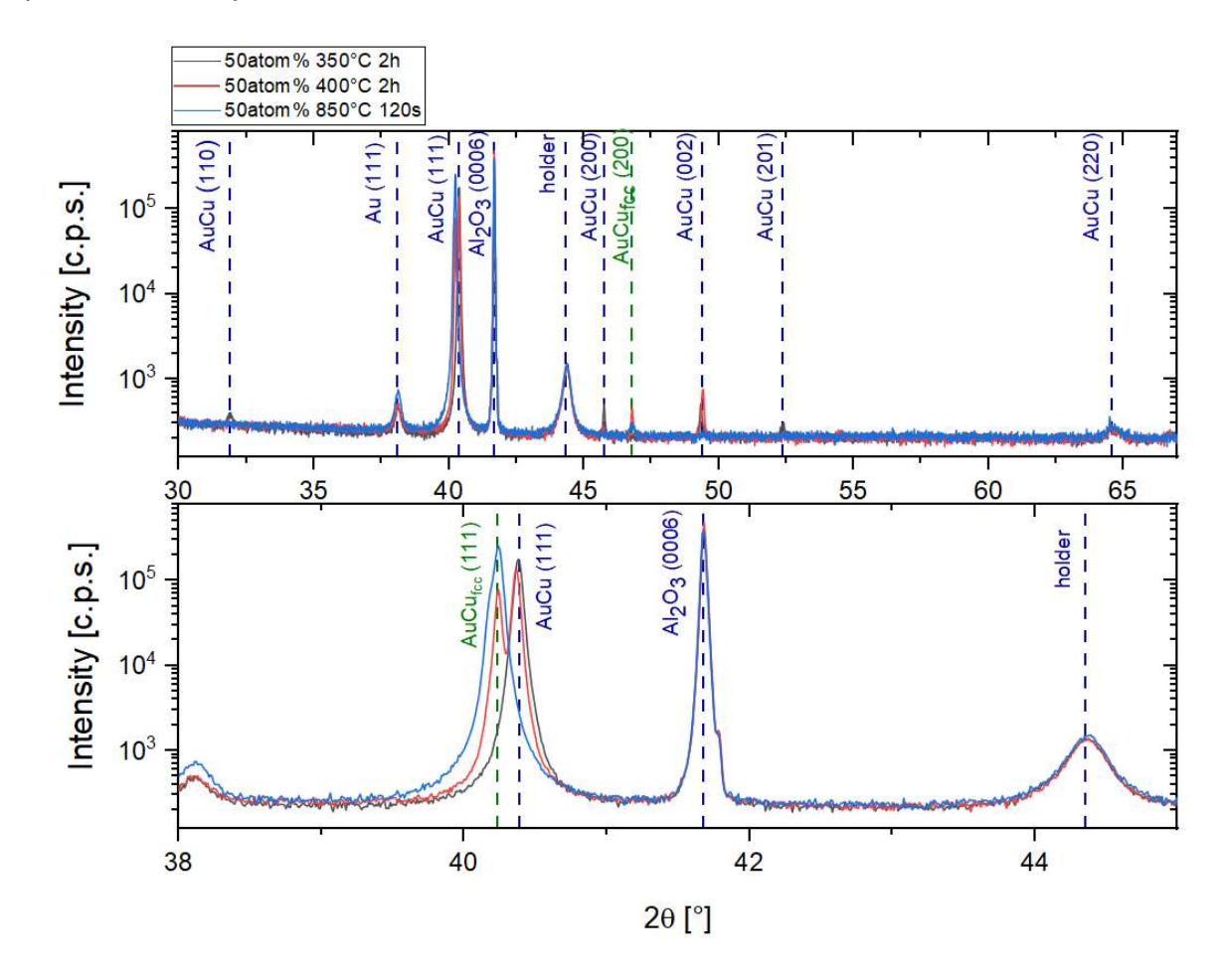


**Figure 45:** XRD measurement of  $50~at.\%_{Au}$  particles with ordered phases compared to a sample with a fcc structure and a close-up of the AuCu (111) peak showing a double peak of the 400 °C annealed sample. The separation between (200) and (002) peaks reveal the existence of a tetragonal crystal system.

Overall, no peak shifting is observed due to the fact that the samples have the same concentration.

For the lattice parameter calculation a different equation is used because no cubic system is present anymore. Therefore, the parameter was calculated for a tetragonal crystal system with c being a lattice constant.

$$a = \sqrt{(h^2 + k^2) \cdot \left(\frac{1}{d_{hk}^2} - \frac{l^2}{c^2}\right)^{-1}}$$
 (11)

Thereby higher lattice parameter in comparison to the fcc system was calculated by Equation 11 of a=3.96 Å with the parameter c=3.68 Å. This was expected due to the AuCu alloy existence in the solid solution. This structure allows a more dense packing of the atoms than in the arrangement of a L1<sub>0</sub>-type of structure.

# 4.5.2 TEM investigations

Ordered phased particles were fabricated at post annealing times of 400 °C analogous to the ones described above in Chapter 4.5 on a SiN<sub>x</sub> membrane TEM grid. These particles were analysed via SAD in the TEM obtaining diffraction pattern of the selected area chosen. When observing the sample under the TEM it is noticeable that most of the particles fabricated were too thick for analysis in the TEM as seen in Figure 46.

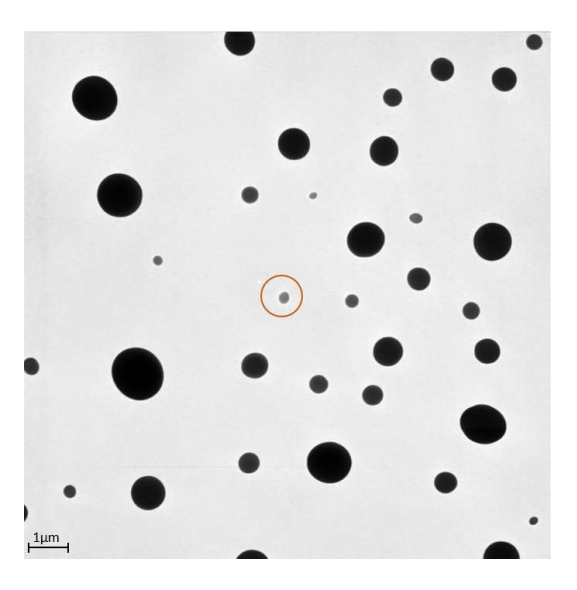


**Figure 46:** TEM image of ordered particles on a  $SiN_x$  TEM grid. Most particles being too thick for SAD measurements therefore the thinner marked particle is measured.

Nevertheless, a SAD measurement was performed at a single particle with reduced thickness (marked in Figure 46) resulting in a diffraction pattern shown in Figure 47. Additionally, line scans of the reflections were made visualised next to the diffraction pattern where the peak intensities and positions are demonstrated.

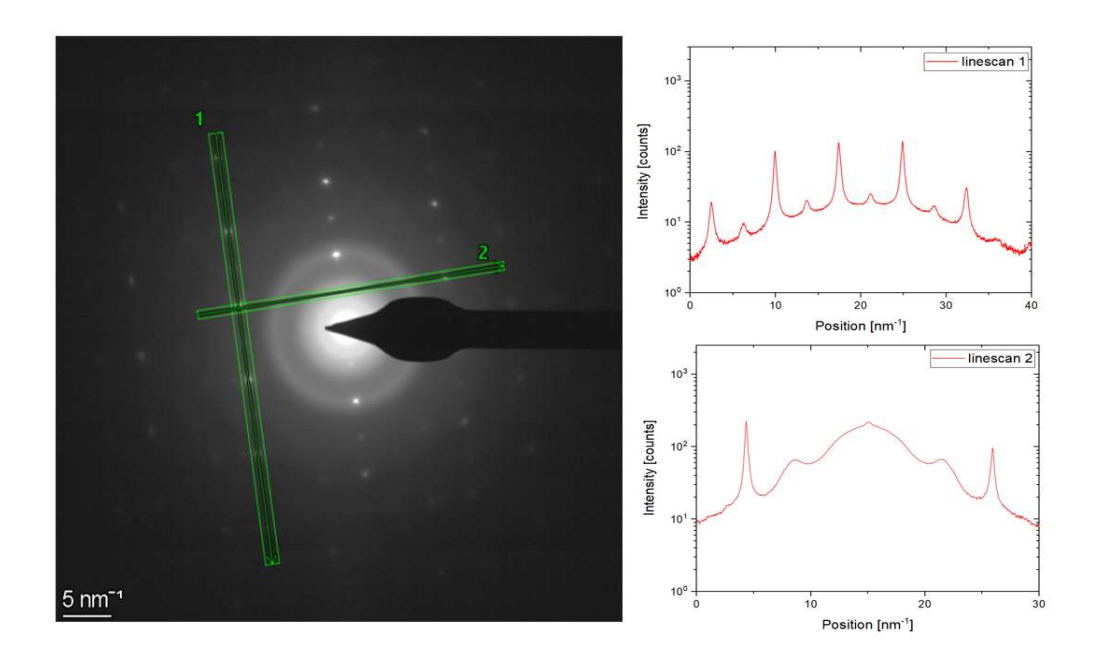


**Figure 47:** SAD measurement of ordered phase AuCu particles showing two line profiles of the reflections observed indicating superlattice reflections of the weaker ones.

The particles' orientation on an amorphous  $SiN_x$  membrane TEM grid experience texture loss in comparison to particles on a  $\alpha$ -Al<sub>2</sub>O<sub>3</sub> substrate. A (2-32) zone axis was observed of the particle on the  $SiN_x$  membrane marked in Figure 46 considering the diffraction pattern shown in Figure 47. Each upcoming diffraction dot was identified and indexed in Figure 48. The reflexions are clearly observable (in green) with weaker superlattice reflections (in red) among them. The brighter appearing reflections result from the cubic crystal system whereas the weaker spots, the superlattice reflections, arise from the tetragonal crystal system. The lattice parameter a and parameter b0 were calculated by measuring the distance to the intended peaks in the linescan and thereby calculating the lattice spacing  $d_{nkl}$  as mentioned in Equation 6. The lattice parameter b1 can be now easily calculated by Equation 11 likewise to the ordered phases on the sapphire substrate.

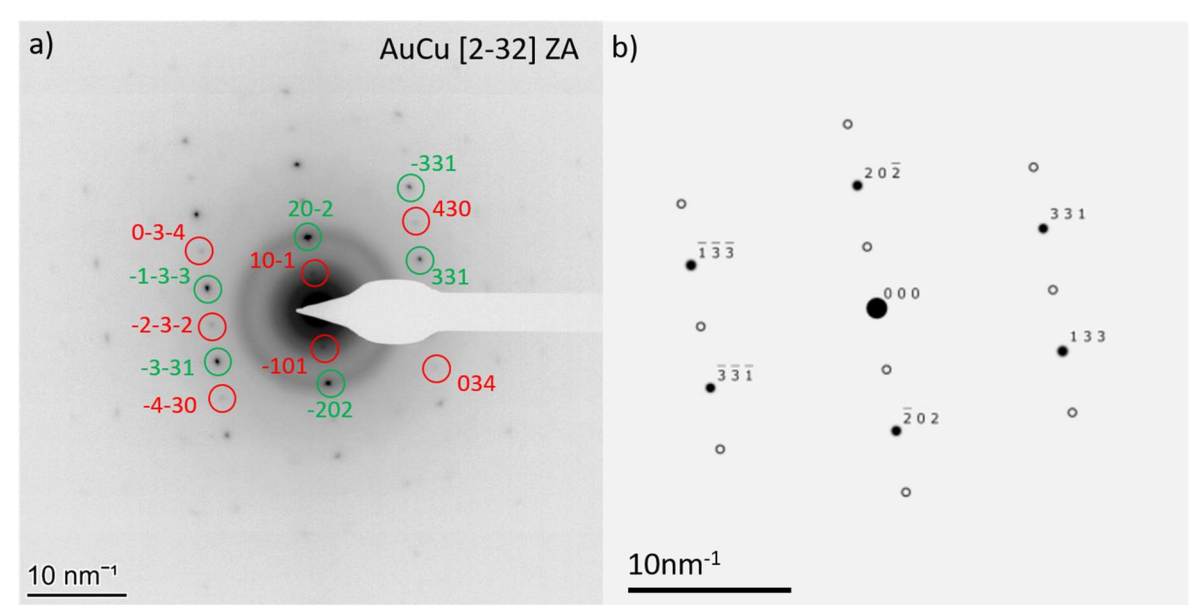


**Figure 48:** SAD diffraction pattern with an identified (2-32) zone axis and the corresponding labelled diffraction spots showing clear reflection dots (green) as well as weaker superlattice reflections (red) visualising the existent ordered phases.

The calculated lattice parameter  $a=3.84\text{\AA}$  and parameter  $c=3.79\text{\AA}$  show in comparison to the particles' parameter on a sapphire substrate in Chapter 4.5.1 a smaller a of  $\Delta a=0.12\text{\AA}$  and higher c of  $\Delta c=0.11\text{\AA}$ . Both parameters show about the same deviation from the particles on the sapphire substrate demonstrating the same relation between parameter a and c independent from the substrate. In fact, a lattice parameter close to one of the ordered phased particles on the sapphire substrate is expected. Yet, quite high differences between these two parameters are observable. Still, the calculation of the lattice parameter via measuring the distance in the linescan is not a too accurate method. Additionally, small divergences of the samples' concentration might cause a change of lattice parameter as already seen at the concentration series under Chapter 4.4.

# 5. Discussion

In this Chapter the results received and presented before are discussed. Conclusions can be made about the general process of AuCu solid-state dewetting, about the deviations observed in SSD and XRD, particles' formation and faceting as well as the specific peak appearances at XRD.

# 5.1 The solid-state dewetting process

This work deals largely with the SSD mechanism of AuCu and detecting the ideal parameters. With the results presented under the Chapter 4.1 and 4.2 statements about the SSD behaviour of the AuCu *40nm* bilayer system can be made.

The predominant growth directions of dewetting are visualised in Figure 32 where an FFT was performed on a SEM picture of a 600 °C 1200 s annealed sample finding itself in the initial state of dewetting. Clear lines appear which signalise three favoured dewetting directions being two diagonally and one vertically to the image. The visual lines are organised in a 60° angle to each other leading to the assumption that the (111) orientation relates to the predominant dewetting directions due to the existent six (110) planes bordering at the sides of the (111) facet. Subsequently the suggestion is that the predominant dewetting directions follow along the (110) directions as already noticed in other literature [40].

The overall dewetting behaviour of the AuCu thin film observed in the present work is similar to that in other systems reported in several literature including void formation, rim formation and pinch-off [1,2,6].

### 5.1.1 Deviations from the SSD trend

Some deviations are observed when analysing Figure 27 where SEM images of dewetted samples with varying annealing time and temperature are illustrated. The state of SSD can be read out and it may be compared to the calculated *%areas* in image 28. The trend of SSD we expect to notice due to several sources is that with increasing temperature and longer annealing time the %area decreases [41]. Most noticeable is the deviation between the annealing times of 900 s and 1200 s at 700 °C. This becomes clear when considering the SEM images where the 1200 s sample has much larger and connected particles than the 900 s sample which is contradictory to the trend expected. Though taking the *%area* in account the 900 s sample shows a by  $\Delta\% are a_{900/1200} = 4.88 \%$  higher area caused by the much higher particle density. Additionally, deviating from the expectations is the sample annealed at 850 °C for 1200 s where reaching the ideal temperature for SSD no significant change in the dewetted area should be noticeable. Examining the 1200s sample at 850 °C abrupt increase in the %area by  $\Delta$ % are  $a_{900/1200} = 5.14$  % is observed due to the high increase in the particle density illustrated in the SEM image. Likewise, a minimization of particle size is detected. This phenomenon is also observed in another literature where the particle size is decreasing with increasing particle density. It also occurred at higher annealing times of 10 minutes at 900 °C for an AuNi alloy wherefore no particular explanation was provided [41].

Then again, the SSD is a sensitive process and such deviations can be provoked easily by any perturbations caused in the production of those specimen. Pollution on the substrate can be hardly avoided as well as any discontinuities in the PVD and heating process. Often irregularities appeared when heating in the RTA, even resulting in shattering of the Wafer, which was fixed but cannot be excluded. At last, the fact that other samples were heated under the same conditions (850 °C 1200 s) and behaving standardized suppose the assumption that the deviating samples underwent inconsistencies in the fabrication.

#### 5.2 Particle formation

The particles fabricated by SSD form facets which can variate depending on annealing time, temperature and elemental concentration. At 800 °C rather elongated grains are formed which evolve due to insufficient annealing temperature. This means that the activation energy in not high enough to reach the spherical particle shape. At 850 °C the most ideal temperature is given for particle production forming spherical ones. This trend is also observed at several literatures where with longer annealing times and increasing temperatures the particles' shape evolve from elongated to circular [41].

When considering the faceting, different types can be seen in Figure 49. Particles with a rectangular plane pointing upwards are observed which seems to be a (100) orientation. Also, rather round particles with an assumed (111) orientation due to the hexagonal shape appearing on the particles' surface is noticed. It is uncommon for fcc particles to adopt (100) orientations on a  $\alpha$ -Al2O3 substrate leading to the suggestion that the seemingly (100) oriented particles obtain a (111) orientation where the faceting is not yet developed completely. So it is difficult to conclude the particle's orientation just by the faceting.

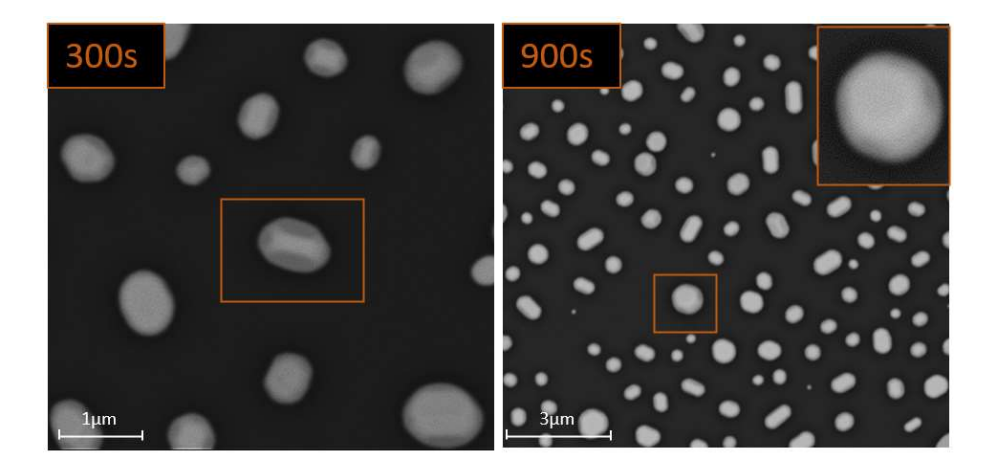


**Figure 49:** Particle shape and faceting showing at *300 s* a particle with a rectangular shape on its surface not giving a clear indication on the orientation and at *900 s* a hexagonal shape on its surface as it is characteristic for a *(111)* OOP orientation.

### 5.3 XRD discussion

The XRD measurements generate a lot of insights into the particles' properties like texturing, orientation or chemical composition. It is firstly helpful to identify the expected peak emergence at different crystal systems which is calculated by the structure factor  $F_{hkl}$  [42]:

$$F_{hkl} = \sum_{j=1}^{N} f_j(H) \cdot \exp(2\pi i H r_j)$$
 (12)

with N as the number of particles, j as the particle position,  $f_j$  as the atomic factor,  $r_j$  as the scattering factor of the j-th atom and H as the reciprocal lattice vector.

The peak appearance obviously differs from the face centred cubic to the tetragonal crystal system in the ordered phases. For these two cases the structure factors were calculated in the following. In accordance with the AuCu phase diagram an fcc is existent in the solid solution where each element does not take any specific place in this crystal as shown in Figure 9. Therefore, the atomic form factor can be estimated through building the average between both elements.

$$F_{111} = f_{AuCu} \cdot (1 + (-1)^{h+k} + (-1)^{h+l} + (-1)^{k+l}) = 4 \cdot f_{AuCu}$$

$$F_{110} = 0$$

$$F_{100} = 0$$

$$F_{200} = 4 \cdot f_{AuCu}$$

Only peaks at all even or all odd (hkl) numbers are appearing in the XRD measurements of fcc materials. Hence the orientation with a structure factor of zero does not show any intensity in the diffractogram.

The tetragonal and orthorhombic crystal systems obtain a specific alignment of each element in the unit cell as illustrated in the phase diagram. Further the calculations of the observable peaks are demonstrated:

$$F_{111} = f_{Au} \cdot (-1)^{k+l} + f_{Cu} \cdot (1 + (-1)^{h+k}) = f_{Au} + 2 \cdot f_{Cu}$$

$$F_{110} = 2 \cdot f_{Cu} - f_{Au}$$

$$F_{100} = f_{Au}$$

$$F_{200} = f_{Au} + 2 \cdot f_{Cu}$$

### 5.3.1 Deviations of peak appearances

XRD measurements of a concentration series, Vegard and Bulk concentrations with fcc structures in the solid solution and the samples with the ordered phases were performed. Some inconsistencies appeared in comparison to the expectations or regarding the other measurements.

The emergence of peak shifting is observed frequently in the measurements where in the case of the concentration series the shifting can be explained through concentration variations. There it was detected that with decreasing Au concentration the peak is shifted to higher angles which confirms the successful formation of AuCu solid solutions and is in line with literature for other bimetallic solid solutions like AuNi [43]. When the Au concentration is decreased the probability of Cu taking the place in the unit cell is higher wherefore the lattice constant decreases because its lattice constant is clearly smaller than the Au one. Due to the reduced lattice constant the rightwards shift is obtained [43]. At the ordered phases no such an incident occurs which is expected due to the consistent elemental concentration. On the contrary the Bulk and Vegard's measurements should have consistent concentrations as well however shifting occurs especially for the AuCu (111) and (200) peak. The samples were produced for each

concentration in one batch but when quantifying the concentration by point measurements in the EDX of the Tabletop SEM, to confirm the consistency of the concentration of each sample, deviations are sighted. On each sample, nine point measurements were recorded. Out of that, the mean concentration with its standard deviation can be extracted which is listed in Table 4.

**Table 4:** EDX point measurements of each Vegard  $59.5~at.\%_{Au}$  and Bulk  $53.8~at.\%_{Au}$  sample annealed for 120~s-1200~s showing slight deviations to the intended concentration.

average measured at.% Au		annealing times [s]	
	52	120	
9	55	300	
Vegard	55	600	
>	55	900	
	57	1200	
	56	120	
	50	300	
~	50	600	
Bulk	49	900	
	50	1200	

In Table 4 some concentration variations are detected where the initial concentrations are  $a_{Bulk} = 53.8 \ at. \%_{Au}$  and  $a_{Vegard} = 59.5 \ at. \%_{Au}$ . The shift mainly does not correlate according to the trend when considering the increase or decrease of Au concentration measured. Though a concentration variation is existent wherefore most likely the shifting occurs.

Furthermore, the intensity loss at the AuCu (111) peak is observed at a concentration of 52~at.  $\%_{Au}$  and 54~at.  $\%_{Au}$  which are close to the lattice matching. Those integrated intensities are  $I_{52at.\%}=339.99$  and  $I_{54at.\%}=271.46$  compared to the other intensities being in the range of  $I_{48at.\%}=27680.89$  which is a radical difference. Yet the intensity at the AuCu (200) peak of both concentration is higher in comparison to other concentrations. Accordingly, texture loss is observed when

being close to or at the lattice match between particle and substrate. The  $\frac{I_{111}}{I_{200}}$  is visualised in Figure 50 where the rapid decrease in texturing at these specific concentrations is demonstrated.

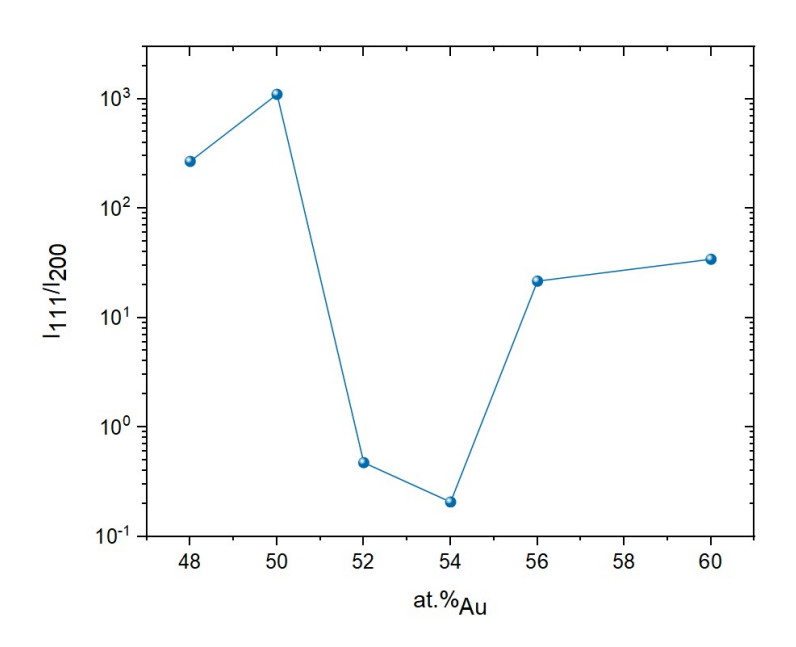


Figure 50: I111/I200 against at.% Au visualising the texture loss at 52 at.% Au and 54 at.% Au.

This phenomenon also occurred when annealing AuNi particles at  $650^{\circ}C$  at specific layer thicknesses (5nm Ni/5nm Au and 10nm Ni/10nm Au) also causing rapid decrease of  $\frac{I_{111}}{I_{200}}$ . This is explained in this literature through the higher strain in thinner films [43]. Due to the constant total film thickness of 40nm in our experiments and the emergence at just two concentrations leads to the assumption that more strain is induced when approaching the lattice match. The hypothesis is that near lattice match, a small bending of the planes directly at the interface is energetically more unvaforable than a higher mismatch. To compensate that, the particles tend to tilt away from the ideal orientation. So far this is a possible assumption for that but a detailed theoretical explanation is still outstanding.

#### 5.3.2 Peak observation

Face centred cubic is the crystal system that was existent for the concentration series as well as for the Vegard and Bulk concentration measurements. Accordingly, only specific peaks may appear for the different AuCu orientations. The (111) and (200) AuCu orientations are observed agreeable to the  $F_{hkl}$  calculated before. Furthermore, the tetragonal system of the ordered phases discussed in Chapter 4.5 allow the appearance of all peaks. This matches with the measured XRD data and observed peaks. However, the separation of the (200) and (002) peak confirm the existents of a distortion of the crystallographic cubic unit cell characteristic for the L1<sub>0</sub>-type structure according to literature [44]. These peaks are observable in the tetragonal system due to the inequality of the unit cell's parameter  $a \neq c$  and therefore showing a separation of these peaks.

The energetically most favourable orientation of fcc particles on a sapphire substrate is the (111) orientation where this orientation extensively dominates yet also AuCu (200) orientation is seen. This peak might be caused when no sufficient annealing time is provided so some particles are not able yet to reach the equilibrium orientation and therefore remain in the (200) orientation. In Figure 51 the texture evolution of a fcc is illustrated.

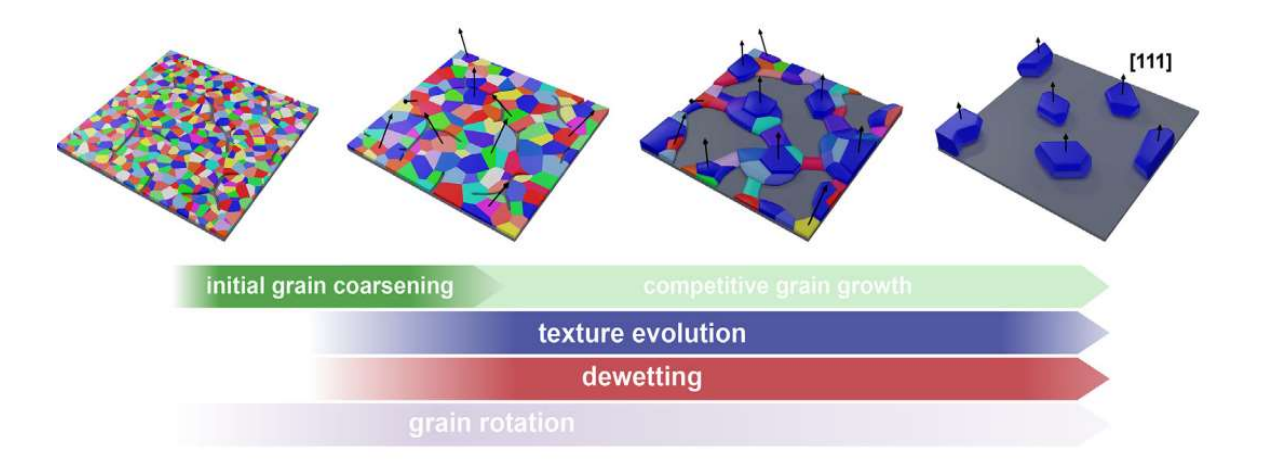


**Figure 51:** Texture evolution of a fcc on a sapphire substrate showing the preferred *(111)* orientation [45].

A reason for this conclusion is that in the Bulk concentration this AuCu (200) peak disappears when annealing the sample for 1200 s. Then again at the Vegard concentration no such extinction takes place however the 1200 s sample exhibits already some deviations in the SSD process discussed in 5.1. Additionally, all samples measured in the concentration series were just annealed for 120 s so no statement can be concluded through that. Another reason for particles adopting the (200) orientation could be to reduce strain due to obtaining the smallest strain energy density in this orientation [43].

When considering the XRD of the ordered phases another peculiarity occurs. Only the sample post annealed at 350 °C shows the AuCu (110) and (201) peaks. Then again, their low intensities let is assume that also peaks of the 400 °C post annealed sample exist yet are so low that no peak can be seen.

Furthermore, when observing the close-up of the AuCu (111) peak a double peak is visible at the 400 °C post annealed sample. When post annealing the sample at this temperature a tetragonal crystal system is expected. One peak is roughly in alignment with the (111) peak of the 350 °C illustrating a tetragonal crystal system whereas the other one is shifted towards lower 20 angles near to the fcc AuCufcc (111) peak. This leads to the assumption that one part of these particles obtains an tetragonal system. Whereas the other part finds itself in a presumably slightly distorted fcc AuCu (111) system due to the minimal shift to the higher angles in contrast to the peak of the fcc sample without post annealing. The reason for the double peak might be the considerably high temperature for post annealing close to the solid solution.

### 6. Conclusion and Outlook

In this work, AuCu nanoparticles were fabricated successfully by solid-state dewetting finding the ideal annealing parameters of 850 °C for 120 s and indicating particle sizes of about  $r_{300s} = 436,2nm \pm 135,0nm$  to  $r_{1200s} = 306,2nm \pm 65,4nm$ EDX confirmed the particles to be consistently alloyed particles. AFM measurements verified the accuracy of the film thicknesses by E-beam deposition as well as the rim formation in the dewetting process suggesting a conventional SSD mechanism of the AuCu thin film. When applying a FFT on a SEM image three predominant dewetting directions along the (110) directions were observed showing the anisotropy of the SSD process. The test series of varying annealing temperatures and times revealed the trend of increasing SSD with higher annealing temperatures and longer times. When analysing the particles under the SEM grain boundaries and facets appear. A high number of particles presumably obtain a (111) orientation considering the characteristic hexagonal shape on their surface. The expected predominant (111) orientation of AuCu particles on a α-Al<sub>2</sub>O<sub>3</sub> substrate is confirmed by XRD measurements showing no significant changes with increasing annealing times verifying the expectation of a (111) orientation of fcc on  $\alpha$ -Al<sub>2</sub>O<sub>3</sub>. By realising a concentration series lattice match was observed at 52 at.  $\%_{Au}$  for a =3.89 Å showing a significant texture loss in the XRD with an increasing (200) orientation. The texture loss is assumed to be caused due to the apparently energetical preference of higher mismatch than small bending of the planes directly at the interface to make it coherent wherefore the particles tilt away from the ideal orientation. Yet this is a possible assumption but not a detailed theoretical explanation. Furthermore, the expected trend is confirmed that with increasing Au concentration the lattice parameter increases and therefore a peak shift to lower 20 is observed. Additionally, ordered AuCu phases were created causing a tetragonal crystal system showing a predominant (111) orientation in the XRD and for a tetragonal system typical (200) and (002) separation is visual. When annealing the sample close to the limitation between solid solution and ordered phases at 400 °C a double peak is observed indicating the tetragonal (111) and the fcc (111) peak.

With the fabrication of ordered phased AuCu particles on a SiN<sub>x</sub> membrane TEM grid the formation on amorphous substrates under the same conditions were proven to operate as well. SAD measurements revealed a *(2-32)* zone axis where the lattice parameter deviates  $\Delta a = 0.12 \text{Å}$  from the one of the ordered phases on sapphire substrate.

In order to continue the research, an EBSD map can be recorded to obtain more details about on the orientation of single particles. The texture loss can be further investigated by cross-sectional and plan-view investigations of the substrate-particle interface analysing the alignment and the misfit dislocation network. In addition, AuCu particle formation on amorphous substrates, as already briefly covered for SiN<sub>x</sub>, can be analysed onward.

### References

- [1] Herz A. On the solid-state dewetting of Au-Ni and Au-W bilayer polycrystalline thin films and the formation of alloy micro- and nanoparticles. Dissertation.
- [2] Pandey P, Kunwar S, Sui M, Bastola S, Lee J. Role of Annealing Temperature, Time, and Composition on the Fabrication of Aux Pd1-x Nanostructures on c-Plane Sapphire by the Solid-State Dewetting of Bimetallic Thin Films. IEEE Trans. Nanotechnology 2018;17(2):325–31.
- [3] Mendoza-Cruz R, Bazán-Diaz L, Velázquez-Salazar JJ, Samaniego-Benitez JE, Ascencio-Aguirre FM, Herrera-Becerra R et al. Order-disorder phase transitions in Au-Cu nanocubes: from nano-thermodynamics to synthesis. Nanoscale 2017;9(27):9267–74.
- [4] Niekiel F. Solid-state Dewetting of Metallic Thin Films studied by Advanced in situ Electron Microscopy Techniques. Dissertation. Erlangen; 2017.
- [5] Hieke SW, Breitbach B, Dehm G, Scheu C. Microstructural evolution and solid state dewetting of epitaxial Al thin films on sapphire (α-Al2O3). Acta Materialia 2017;133:356–66.
- [6] Thompson CV. Solid-State Dewetting of Thin Films. Annu. Rev. Mater. Res. 2012;42(1):399–434.
- [7] Kovalenko O, Greer JR, Rabkin E. Solid-state dewetting of thin iron films on sapphire substrates controlled by grain boundary diffusion. Acta Materialia 2013;61(9):3148–56.
- [8] Choudhury S, Aguiar JA, Fluss MJ, Hsiung LL, Misra A, Uberuaga BP. Non-uniform Solute Segregation at Semi-Coherent Metal/Oxide Interfaces. Scientific reports 2015;5:13086.
- [9] Dehm G, Rühle M, Ding G, Raj R. Growth and structure of copper thin films deposited on (0001) sapphire by molecular beam epitaxy. Philosophical Magazine B 1995;71(6):1111–24.
- [10] Smallman RE, Ngan A. Surfaces, Grain Boundaries and Interfaces. In: Modern Physical Metallurgy: Elsevier; 2014, p. 415–442.
- [11] Martin Dierner. Interface design of AuxNi1-x alloy nanoparticles on (0 0 0 1) oriented α-Al2O3 investigated by X-rays and electrons. Master's Thesis. Erlangen; 2020.
- [12] Kauffmann-Weiss S, Hamann S, Reichel L, Siegel A, Alexandrakis V, Heller R et al. The Bain library: A Cu-Au buffer template for a continuous variation of lattice parameters in epitaxial films. APL Materials 2014;2(4):46107.
- [13] Yin J, Shan S, Yang L, Mott D, Malis O, Petkov V et al. Gold-Copper Nanoparticles: Nanostructural Evolution and Bifunctional Catalytic Sites. Chem. Mater. 2012;24(24):4662–74.
- [14] Ravi R, Paul A. Diffusion mechanism in the gold-copper system. J Mater Sci: Mater Electron 2012;23(12):2152–6.
- [15] Fedorov PP, Volkov SN. Au-Cu Phase Diagram. Russ. J. Inorg. Chem. 2016;61(6):772-5.
- [16] Franssila S. Introduction to Microfabrication. Chichester, UK: John Wiley & Sons, Ltd; 2010.
- [17] Reichelt K, Jiang X. The preparation of thin films by physical vapour deposition methods. Thin Solid Films 1990;191(1):91–126.

- [18] Franck Laporte. AS-One User's manual: Annealsys; 2014.
- [19] Eaton P, West P. Atomic Force Microscopy: Oxford University Press; 2010.
- [20] Buschow KHJ. Encyclopedia of materials: Science and technology. Amsterdam: Elsevier; 2001.
- [21] Chatterjee S, Gadad SS, Kundu TK. Atomic force microscopy. Reson 2010;15(7):622–42.
- [22] Voigtländer B. Atomic Force Microscopy. Cham: Springer International Publishing; 2019.
- [23] Zhou W, Wang ZL (eds.). Scanning Microscopy for Nanotechnology. New York, NY: Springer New York; 2006.
- [24] Hafner B. Scanning Electron Microscopy Primer. In:
- [25] Thermo Fisher Scientific. Phenom ProX G6 Desktop SEM Desktop SEM with EDS capability for robust, effortless, and versatile elemental analysis. Datasheet; 2021.
- [26] FEI Elstar. Extreme high resolution SEM column. Information Poster.
- [27] Bubert H (ed.). Surface and thin film analysis: Principles, instrumentation, applications. 1st ed. Weinheim: Wiley-VCH; 2003.
- [28] Leng Y. Materials Characterization. Chichester, UK: John Wiley & Sons, Ltd; 2008.
- [29] Goldstein JI, Newbury DE, Echlin P, Joy DC, Lyman CE, Lifshin E et al. Scanning Electron Microscopy and X-ray Microanalysis: Third Edition. Boston, MA: Springer; 2003.
- [30] Birkholz M, Fewster PF. Thin film analysis by X-Ray scattering. 2nd ed. Weinheim: Wiley-VCH; 2009.
- [31] Fultz B, Howe JM. Transmission electron microscopy and diffractometry of materials. 3rd ed. Berlin: Springer; 2008.
- [32] Reimer L. Transmission Electron Microscopy: Physics of Image Formation and Microanalysis. Berlin, Heidelberg, s.l.: Springer Berlin Heidelberg; 1984.
- [33] Williams DB, Carter CB. Transmission electron microscopy: A textbook for materials science. 2nd ed. New York: Springer; 2009.
- [34] Yamasaki J, Ohta K, Morishita S, Tanaka N. Quantitative phase imaging of electron waves using selected-area diffraction. Appl. Phys. Lett. 2012;101(23):234105.
- [35] Chierchia R. Strain and crystalline defects in epitaxial GaN layers studied by high-resolution X-ray diffraction. @Bremen, Univ., Diss., 2007; Available from: http://elib.suub.uni-bremen.de/diss/docs/00011449.pdf.
- [36] Reimer L, Kohl H. Transmission electron microscopy: Physics of image formation. 5th ed. New York, NY: Springer; 2008.
- [37] Johannes Will, Patrick Herre, Tobias Zech, Johanna Schubert, Mingjian Wu, Tadahiro Yokosawa, Jan Schwenger, Stefan Romeis, Dong Wang, Tobias Unruh, Wolfgang Peukert, and Erdmann Spiecker. Correlative TEM and XRD study of the role of Au on the solid state dewetting behavior of Au/Ni bilayers on [alpha]-Al2O3; 2019.
- [38] Abdullah O. Modeling the lattice parameters of solid solution alloys. Hamburg: Anchor Academic Publishing; 2017.

#### References

- [39] LIPRAS: Line-Profile Analysis Software. (2017): Giovanni Esteves, Klarissa Ramos, Chris M. Fancher, and Jacob L. Jones.
- [40] Niekiel F, Schweizer P, Kraschewski SM, Butz B, Spiecker E. The process of solid-state dewetting of Au thin films studied by in situ scanning transmission electron microscopy. Acta Materialia 2015;90:118–32.
- [41] Oliva-Ramirez M, Schade P, Zobel C, Wang D, Schaaf P. Morphological and compositional mapping of supersaturated AuNi alloy nanoparticles fabricated by solid state dewetting. Applied Surface Science Advances 2021;4:100082.
- [42] Read RJ. Structure-factor probabilities for related structures. Acta Crystallogr A Found Crystallogr 1990;46(11):900–12.
- [43] Wang D, Schaaf P. Ni–Au bi-metallic nanoparticles formed via dewetting. Materials Letters 2012;70:30–3.
- [44] Krupinski M, Perzanowski M, Zarzycki A, Zabila Y, Marszałek M. Ordered FePdCu nanoisland arrays made by templated solid-state dewetting. Nanotechnology 2015;26(42):425301.
- [45] Niekiel F, Kraschewski SM, Schweizer P, Butz B, Spiecker E. Texture evolution and microstructural changes during solid-state dewetting: A correlative study by complementary in situ TEM techniques. Acta Materialia 2016;115:230–41.

# List of Figures

Figure 1: Void formation at grain boundaries starting at a) the surface by grain
boundary grooving or b) the interface between the substrate and film [4] 3
Figure 2: Mass accumulation forming a rim due to edge retraction closely followed
by valley formation ahead of the rim [6]4
Figure 3: a) Increasing edge retraction leading to increasing depth of the valley, b)
sometimes insofar that the valley reaches the substrate and an isolated rim evolves
[6] 5
Figure 4: Top view of the fingering process evolving into islands due to Rayleigh
instabilities [1]5
Figure 5: A Wulff plot representing the surface energy determined by the length of
the vector $\gamma_{f}$ and the crystal's orientation by the angle $\omega$ resulting in a minimized
surface energy at the four cusps [6]6
Figure 6: The Winterbottom construction considers contrary to the Wulff plot the
interface energy between the film and the substrate finding the crystal's equilibrium
shape [6]7
Figure 7: Different interface pattern between film and substrate forming a a)
coherent interface, b) semi-coherent interface with misfit dislocations and an c)
incoherent interface [11]8
<b>Figure 8:</b> a) The equilibrium texturing of a fcc structure forming a (111) oriented particle on a (0001) oriented α-Al <sub>2</sub> O <sub>3</sub> substrate demonstrating the position and shape of each plane [4]. b) Simulated SAED-Pattern showing the orientation relation Au(111)<1-10>    Al <sub>2</sub> O <sub>3</sub> (0001)<10-10> well known for metal <sub>fcc</sub> – Al <sub>2</sub> O <sub>3</sub> systems [5].
9
Figure 9: Phase diagram of an AuCu alloy with displayed crystallographic structures
in each region, showing a fcc structure in the whole solid solution range at higher
temperatures. At lower temperatures three types of ordered phases CuAu (green),
AuCu <sub>3</sub> (red) and CuAu <sub>3</sub> (blue) exist [15]11

Figure 10: Procedure of PVD by E-Beam heating causing material evaporation by
inducing high energy. These atoms/molecules are deposited on the substrate
placed above12
Figure 11: Vacuum chamber of a Winter Vakuumstechnik HVB 130 showing the
target material and the sample holder positioned above 13
Figure 12: The process chamber of an AS-One 100 [18] specified in a cross section
of the inside [1] showing the lamp furnace, the cooled bedplate and the quartz pins
holding the wafer14
Figure 13: A schematic setup of an AFM illustrating the measurement by means of
the cantilever in the contact mode. Measurements of the cantilever's deflection are
detected which behave proportional to the forces achieving a three-dimensional plot
of the height data against the distance [22]16
Figure 14: Sample preparation for height-difference and film thickness
measurement in the AFM17
Figure 15: Signals generated through beam-specimen interaction illustrated in an
interaction volume showing the two electron types for imaging in the SEM, SE and
BSE [24]
Figure 16: Structure of a SEM column of the Helios Nanolab 660 visualising the
electron source, the Schottky field emitter, lenses and different detectors [26] 20
Figure 17: Generating characteristic X-rays or Auger electrons through the
interaction of the specimen's atoms with the electron beam [28]21
Figure 18: Bragg deflection of X-rays at lattice planes at a certain angle $\theta$ leading
to either constructive or to destructive interference depending on the path difference
between two waves. [28]
Figure 19: Working mechanism of a X-ray OOP measurement illustrating the
movement of the X-ray source and detector in equal measure maintaining the same
incoming and outcoming angle $ heta.$ The measured $2 heta$ angle is visualised as well as
the plane being measured [30]25
Figure 20: The most common operations in the TEM are a) the diffraction mode
and b) the imaging mode [33]26

Figure 21: Ewald sphere construction with a radius related to the wavelength
showing the incident wave vector $k_{\rm i}$ and diffracted wave vector $k_{\rm e}$ [35]
Figure 22: The total 40nm AuCu layer on top of the sapphire substrate showing the
order of each layer deposited29
Figure 23:Evolution of the lattice parameter for AuCu alloys as a function of the Au
concentration showing a deviation between the Vegard's prediction and the data for
bulk alloys [12] . The line at a=3.89Å indicates the lattice parameter needed for
lattice matching
Figure 24: Film thickness measured by the AFM compared to the intended layer
thickness marked with a horizontal line () showing a good correlation to the AFM
measured thicknesses
Figure 25: Three-dimensional AFM recording of a 40nm AuCu layer illustrated with
the software Gwyddion
Figure 26: Height map of a SSD (T=600 °C t=300 s) sample demonstrated a) in a
2D and b) in a 3D illustration visualising rim formation at the edges of the holes. 35
Figure 27: SSD map of AuCu 40nm thin films at variating annealing times and
temperatures showing a trend of increasing SSD with higher temperatures and
longer annealing times
Figure 28: Changing %area through varying annealing temperatures and annealing
times showing a trend of decreasing %area with a) increasing annealing time and
b) higher temperatures39
Figure 29: Facetted particles dewetted at 800 °C imaged with BSE in the Tabletop
SEM
Figure 30: Relative frequency [%] plotted against the particle size [nm] showing the
particle size distribution of the 800 °C series calculated by assuming the particles'
circularity by means of the software ImageJ40
Figure 31:Relative frequency [%] plotted against the particle size [nm] showing the
particle size distribution of the 850 °C series calculated by assuming the particles'
circularity by means of the software ImageJ41
Figure 32: a) A FFT image of b) a dewetted AuCu specimen at 600 °C after 1200 s
showing three predominant directions for SSD

Figure 33: EDX maps of Au (red) and Cu (green) in the Tabletop SEM on a 40nm
SSD AuCu thin film at a) 600 °C and b) 800 °C for 600 s showing in both samples a
uniform distribution of Au and Cu and therefore a consistent AuCu alloy43
Figure 34: Comparison of dewetted %area between two concentrations calculated
considering Vegard's law (59.5 at.%Au) and Bulk (53.8 at.%Au) showing an
approximate constant %area with changing annealing times except the deviation at
59.5 at.% <sub>Au</sub> 1200s
Figure 35: SEM image with a) a TLD illustrating the spherical shape of particles and
with b) a CBS detector showing the faceting of particles of a 850 °C 300 s 59.5
at.% Au sample
Figure 36: Qualitative EDX maps of a a) 59.5 at.% Au sample at annealing times of
$300~ ext{s}$ and $1200~ ext{s}$ and a b) $53.8~ ext{at.}\%_{ ext{Au}}$ sample annealed at $120~ ext{s},$ illustrating the <code>Au</code>
and Cu concentrations of several and one single particle revealing a homogeneous
distribution and therefore the existence of an alloy
Figure 37: SEM picture in the FIB with a CBS detector of faceted particles on a
850 °C 1200 s 59.5 $at.\% Au$ sample showing the existence of three types of particles
the most important (111) oriented particles (red), the tilted particles (blue) and the
particles with grain boundaries (green)
<b>Figure 38</b> : (111) oriented particles of a) 59.5 $at$ . % $Au$ 1200 s, b) 59.5 $at$ . % $Au$ 120 s
and c) 53.8 $at.\%Au$ 900 s samples revealed by a) six impressions on their
sides or b) and c) a triangular shape on top of them
Figure 39: SEM images of deviating particles detected with a CBS of a a) 1200 s
annealed and b) 600 s annealed 53.8 $at.\% Au$ sample showing more facets than
particles at 59.5 $at.\% Au$ throughout maintaining the (111) orientation
Figure 40: XRD measurements of the a) Vegard and b) Bulk concentrations with
labelled peaks showing a predominant (111) orientation 51
<b>Figure 41:</b> SEM pictures of the SSD state of AuCu 40nm thin films at variating at. $\%_{Au}$
concentration annealed at constant 850 °C for 120 s showing decreasing SSD with
high at.% <sub>Au</sub> where concentrations of 0-60 at.% <sub>Au</sub> show a similar SSD state 54
Figure 42: Behaviour of the SSD with increasing Au concentration demonstrated by
the %area. At a range between 0 at.% $_{ extsf{Au}}$ and 60 at.% $_{ extsf{Au}}$ the dewetted area stays

# List of Figures

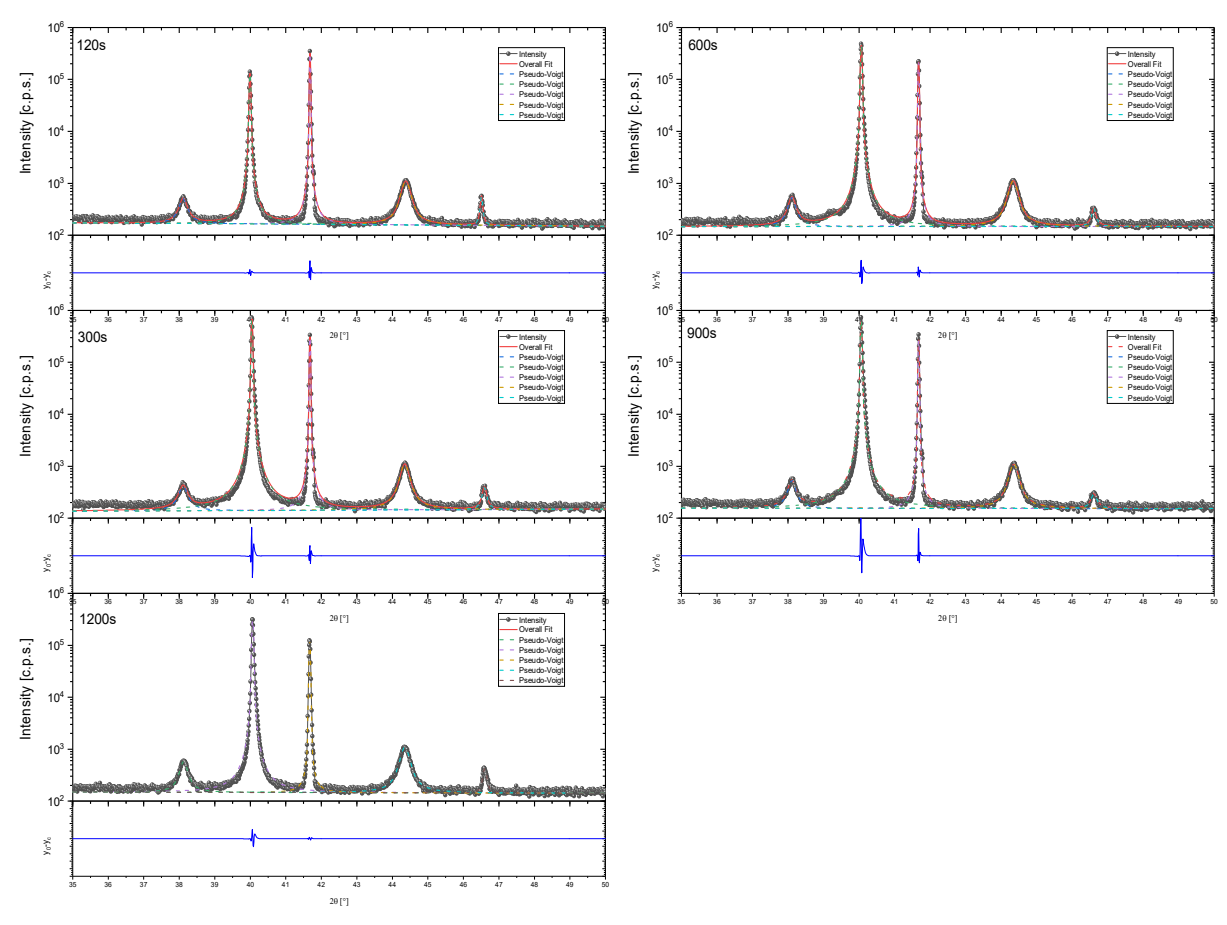
approximately the same whereupon with high Au concentration from 80 at. $\%_{\text{Au}}$ the
%area increases rapidly55
Figure 43: XRD data of the concentration series from 0 -100 at. %Au showing a shift
of the (111) and (200) peak to higher angles with decreasing at. %Au and texture
loss at 52 at. %Au and 54 at. %Au sample 56
Figure 44: Experimental data illustrating the behaviour of the lattice parameter with
increasing at. $\%_{\text{Au}}$ compared to Bulk and Vegard. The experimental data matches
the Bulk plot closely especially in the region of the lattice match highlighted with a
horizontal line at a=3.89 Å approximating the data with EDX point measurements.
58
Figure 45: XRD measurement of 50 $at.\%Au$ particles with ordered phases
compared to a sample with a fcc structure and a close-up of the AuCu (111) peak
showing a double peak of the 400 °C annealed sample. The separation between
(200) and (002) peaks reveal the existence of a tetragonal crystal system 60
Figure 46: TEM image of ordered particles on a SiN <sub>x</sub> TEM grid. Most particles being
too thick for SAD measurements therefore the thinner marked particle is measured.
62
Figure 47: SAD measurement of ordered phase AuCu particles showing two line
profiles of the reflections observed indicating superlattice reflections of the weaker
ones
Figure 48: SAD diffraction pattern with an identified (2-32) zone axis and the
corresponding labelled diffraction spots showing clear reflection dots (green) as well
as weaker superlattice reflections (red) visualising the existent ordered phases. 64
Figure 49: Particle shape and faceting showing at 300 s a particle with a rectangular
shape on its surface not giving a clear indication on the orientation and at 900 s a
hexagonal shape on its surface as it is characteristic for a (111) OOP orientation.
67
Figure 50: I111/I200 against at.% Au visualising the texture loss at 52 at.% Au and 54
at.% <sub>Au</sub>
Figure 51: Texture evolution of a fcc on a sapphire substrate showing the preferred
(111) orientation [45]

## List of Tables

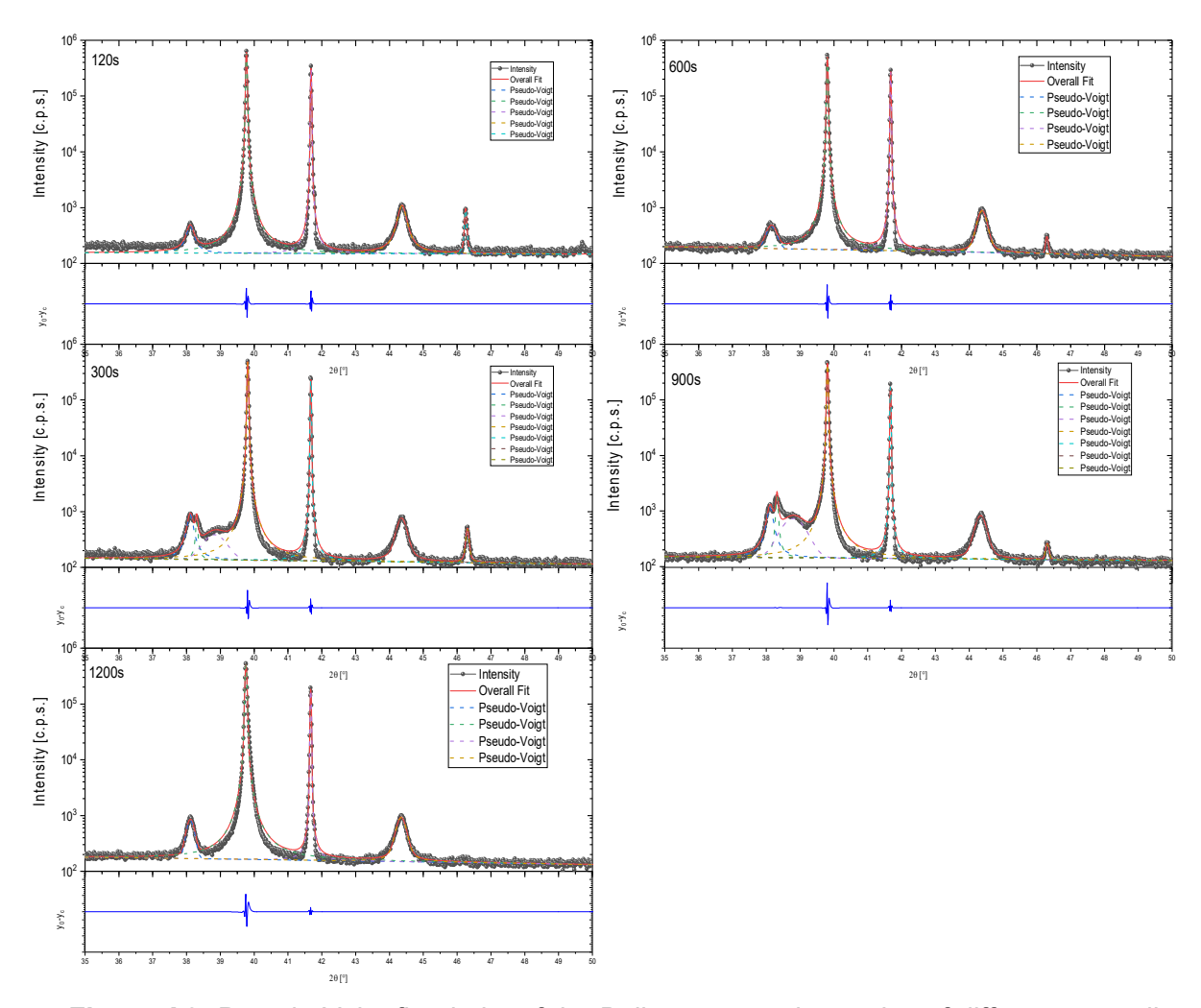
## List of Tables

Table 1: Atomic percent and film thickness of Au and Cu is calculated for different
concentrations adjusting the lattice parameter32
<b>Table 2:</b> The intended at. $\%_{Au}$ concentration compared to the EDX point
measurements showing slight deviations whereby the EDX measurements shows
rather a lower at.% <sub>Au</sub> than intended53
Table 3: The lattice parameters corresponding to each atomic concentration
measured in the XRD test series57
<b>Table 4:</b> EDX point measurements of each Vegard 59.5 $at.\%Au$ and Bulk 53.8
at.%Au sample annealed for 120 s-1200 s showing slight deviations to the intended
concentration70

# **Appendix**



**Figure A1:** Pseudo-Voigt fitted plot of the Vegard concentration series of different annealing times.



**Figure A2:** Pseudo-Voigt fitted plot of the Bulk concentration series of different annealing times.

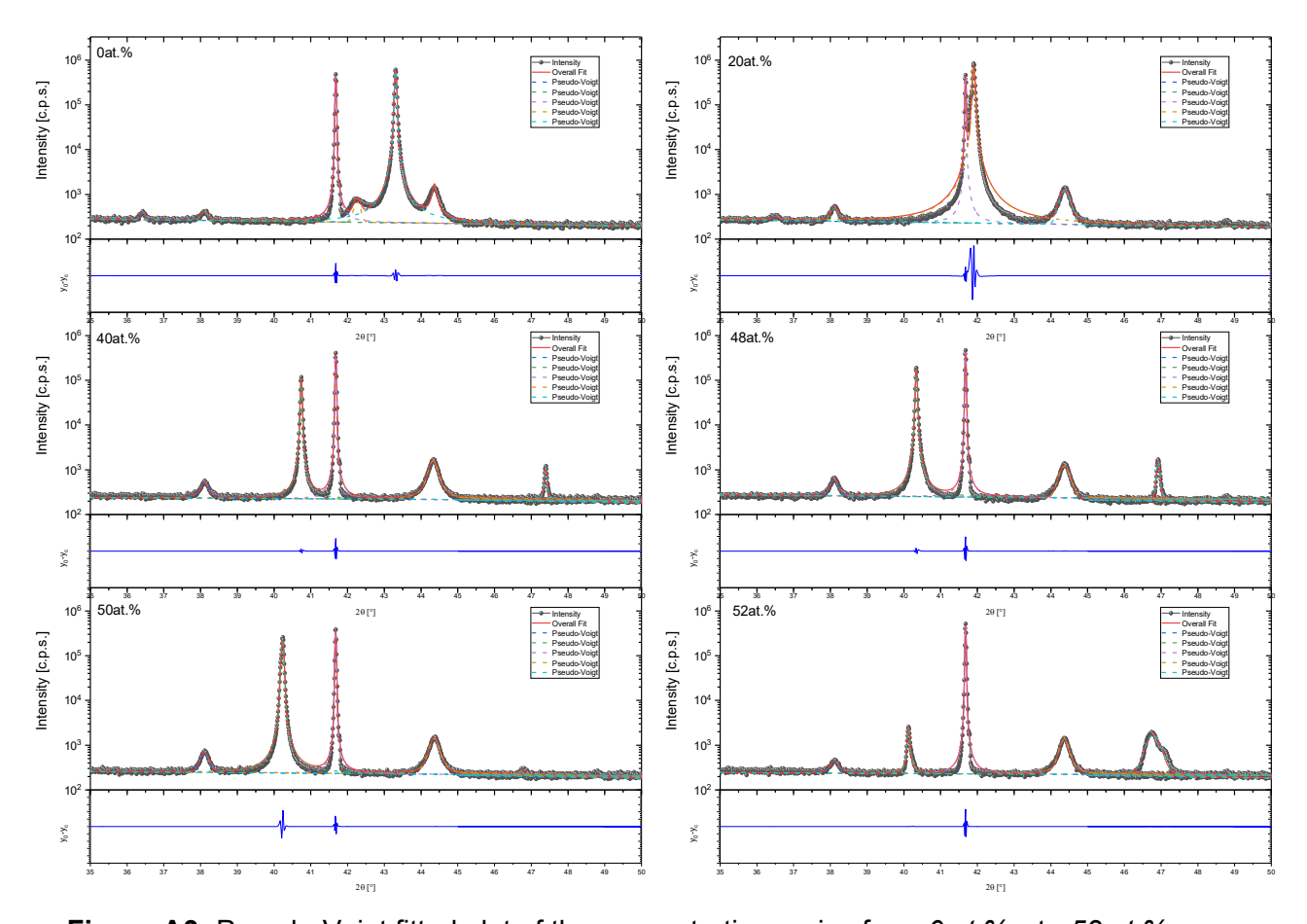


Figure A3: Pseudo-Voigt fitted plot of the concentration series from 0 at.% Au to 52 at.% Au.

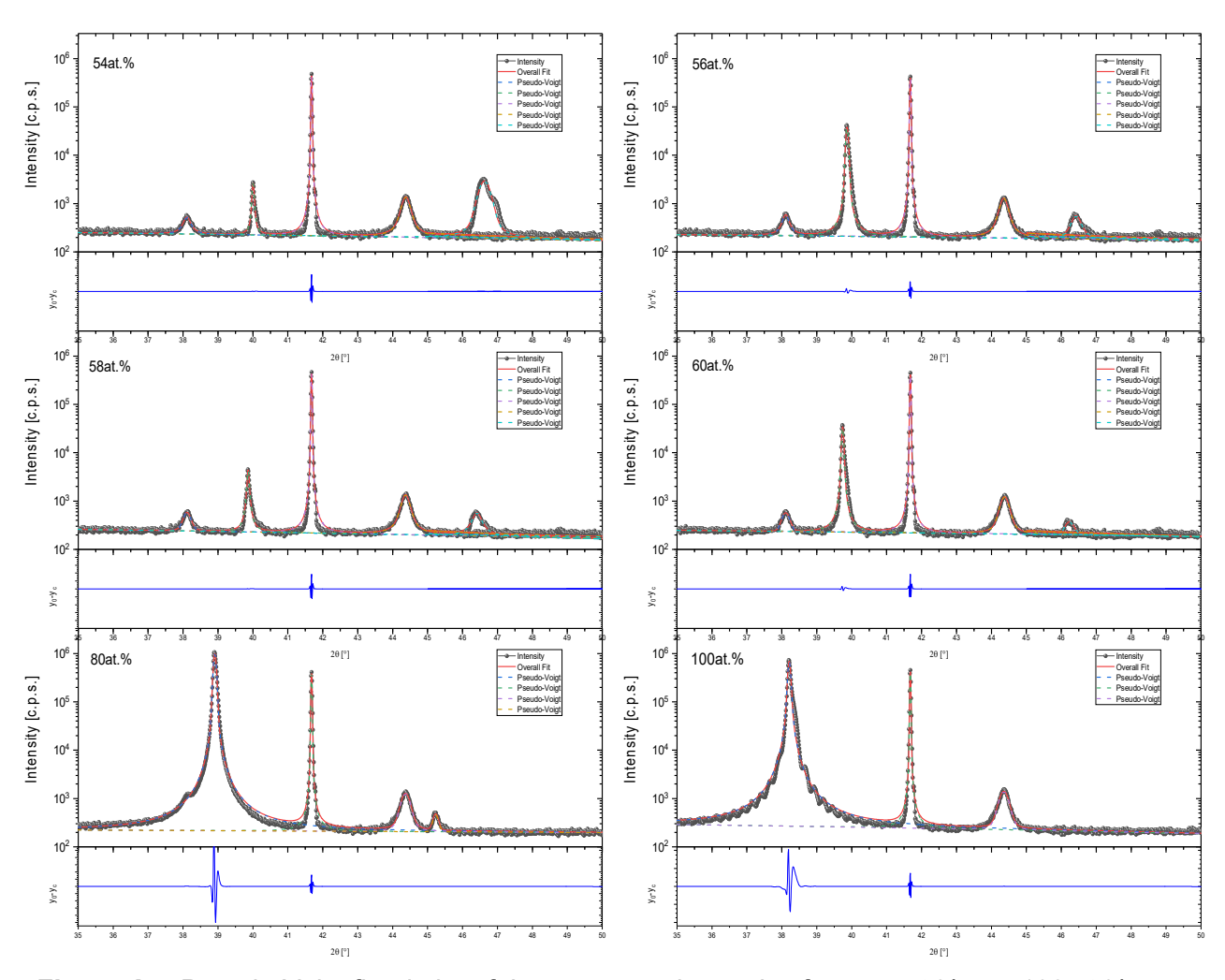
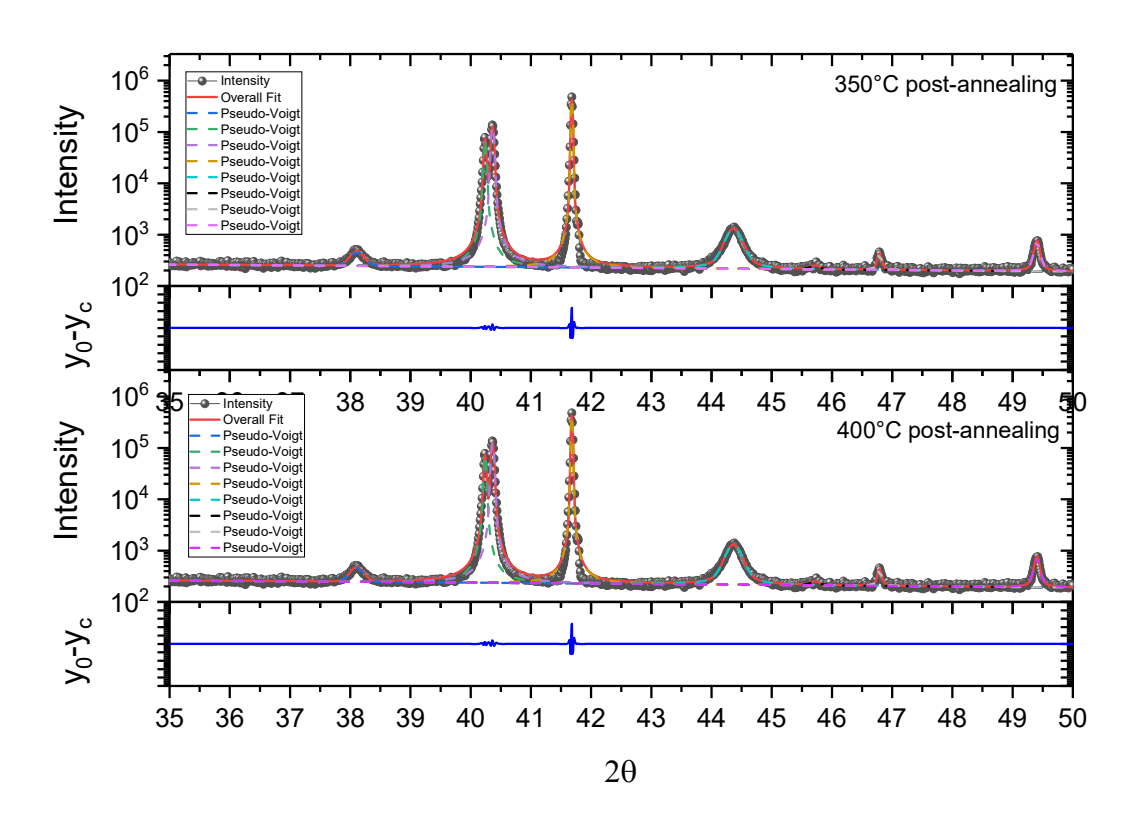


Figure A4: Pseudo-Voigt fitted plot of the concentration series from 54 at.% au to 100 at.% au.



**Figure A5:** Pseudo-Voigt fitted plot of the ordered AuCu phases post-annealed for 350°C or 400°C.

## Acknowledgement

First, I would like to thank **Prof. Erdmann Spiecker** for providing the opportunity to write my thesis in this interesting topic at his Institute of Micro- and Nanostructure Research at the Friedrich-Alexander University. Many thanks for the great support and help on any questions regarding this thesis in the meetings.

My special thanks go to **Johanna Schubert** and **Martin Dierner** for introducing me into several methods and your tireless support. Thank you for taking your time to help me in any situation.

Furthermore, I would like to thank:

- ...**Dr. Johannes Will** for the great help at the discussion of the XRD data and generally for the support.
- ...Dorota Kubacka and Robert Branscheid for the help and fixing with the RTA furnace and fixing other technical problems.
- ...Dr. Thomas Przybilla for the support in the particle imaging in the FIB.
- ... Carmen Rubach for keeping the labratory running and giving good advises.
- ...Nicolas Karpstein and Dr. Johannes Will for the balance due to the sporty activities.

A huge thanks to the whole WW9 group for the great atmosphere and support that created an enjoyable working environment during my Bachelor thesis.

### Prüfungsrechtliche Erklärung

## Prüfungsrechtliche Erklärung

Ich versichere, dass ich die Arbeit ohne fremde Hilfe und ohne Benutzung anderer als der angegebenen Quellen angefertigt habe und dass die Arbeit in gleicher oder ähnlicher Form noch keiner anderen Prüfungsbehörde vorgelegen hat und von dieser als Teil einer Prüfungsleistung angenommen wurde. Alle Ausführungen, die wörtlich oder sinngemäß übernommen wurden, sind als solche gekennzeichnet.

	_ Erlangen,	den 09.	September	2021
Evelvn Nachbauer				